

UNIVERSITY
of
GLASGOW

Dynamics of Ions and Neutral Particles in the Sheath Region of Processing Plasmas

by

Neal S. Wade, BEng.

Thesis
submitted to the
University of Glasgow
for the degree of
Ph.D.

Astronomy and Astrophysics Group
Department of Physics and Astronomy
University of Glasgow
Glasgow, G12 8QQ.

Submitted
March 2002

ProQuest Number: 13818842

All rights reserved

INFORMATION TO ALL USERS

The quality of this reproduction is dependent upon the quality of the copy submitted.

In the unlikely event that the author did not send a complete manuscript and there are missing pages, these will be noted. Also, if material had to be removed, a note will indicate the deletion.



ProQuest 13818842

Published by ProQuest LLC (2018). Copyright of the Dissertation is held by the Author.

All rights reserved.

This work is protected against unauthorized copying under Title 17, United States Code
Microform Edition © ProQuest LLC.

ProQuest LLC.
789 East Eisenhower Parkway
P.O. Box 1346
Ann Arbor, MI 48106 – 1346

GLASGOW
UNIVERSITY
LIBRARY:

12491

COPY 1

Abstract



The path of ions traversing the sheath region of a radio frequency plasma is modelled using the Child-Langmuir approximation to the full sheath equation. The collective characteristics of many ions is obtained by Monte Carlo simulation, revealing structure in the relationship between many parameters. By performing a systematic calculation of ion impact energy versus initial energy and phase, a distinctive spiral shape has been observed. This provides additional insight into the mechanism that underlies the bimodal ion energy distributions that are widely reported in plasma processing systems.

A further step has been taken from this observation, to see if it can be used to provide an analytic method for constructing ion energy distributions. A spiral shape that varies continuously across phase and initial ion energy space has been created, replicating that seen in Monte Carlo simulation. By sampling the result across the appropriate initial conditions, an ion energy distribution can be generated.

A numerical solution to the full sheath equation has been implemented. This allows the inclusion of electrons into the area where the sheath region meets the plasma. It has been shown that this causes ions to follow a significantly different path through the sheath region. When an ion first enters the sheath region, it experiences a smaller force due to the reduction in electric field because of the presence of electrons. The effect of this propagates through to the ion energy distribution.

Effects due to the high electric fields that are present in etched substrate features have been considered. Particles with an electric dipole moment are attracted along lines of increasing electric field strength under a mechanism called dielectrophoresis. An assessment of the significance of this force on neutral transport in substrate features has been made. It is found that particles with a typical dielectric moment are accelerated towards the central region of a trench and accelerated out of the trench in a fraction of time that it would take without a force due to dielectrophoresis.

Acknowledgements

Those who helped me get here:

My parents, Mike and Margot, sisters Helen and Liz and all the rest of my family who must have had something to do with me ending up doing this.

Past teachers for their enthusiasm and guidance.

Stuart for asking me to share a graduation meal.

John Brown and Declan Diver, who respectively awakened me to the idea in the first place and thought I was suitable to have a go.

Those who helped me get out:

Members of the Astronomy Group: Darren McDonald, Richard Barrett, Paul Millar, Hugh Potts, Guillian McArthur, Norman Gray, Daphne Davidson, Gail Penny, Noelle Daly, Eve McCollum, Graeme Stewart, Martin Hendry, Brendan Dowds, Sinclair Bremner, Steve Owens, Dave Clarke, Scott McIntosh, Lyndsay Fletcher, Deborah Telfer, Graham Woan, Stephane Rauzy, Esther Haydock, Helen Bryce, Lida Oskinova, Kenton D'Mellow, Etienne Vogt, Callum Alexander, Paul Allan, Dug MacDonald, Martin Hewitson and Rejean Dupuis for their friendship, assistance and interest in my work.

Trampolinists: Frances, Gavin, John, Grant, Elly, James, Jenni, Keith, Nicky and all the rest for not letting me fall off.

Those living in a criminally inept state: Brendan, Joey, Andrew, Judy, Kyra, Emily, Bobby, Colin and Susanne for pop music.

Special thanks to Jenny for understanding.

Declaration of Authorship

The contents of this thesis represent original work carried out by the author at the University of Glasgow. A portion of section 4.1 – 4.7 has been published in N.S. Wade, D.A. Diver, D.C. McDonald and A.P. Millar *Modelling the dielectrophoresis effect on the transport of neutral molecules in processing plasmas*, Physics Letters A, **275**, pp447-451 (2000).

Contents

Abstract	i
Acknowledgements	iii
Declaration of Authorship	v
Symbols and Acronyms	xiv
1 Introduction	1
1.1 Development of Electronic Devices	2
1.2 Defining a Plasma	3
1.2.1 Collective Behaviour	3
1.2.2 Quasineutrality	4
1.2.3 Plasma Frequency	5
1.3 Plasma Processing	6
1.3.1 Plasma Processing as a Tool	6
1.3.2 Plasma Characteristics	7
1.3.3 Sheath Characteristics	8
1.3.4 Reactor Operational Summary	9
1.3.5 Types of Reactor	10
1.3.6 Plasma Chemistry	11
1.4 Planar Sheath Representation	12

1.4.1	Describing the Sheath Region	12
1.4.2	General Sheath Representation	13
1.4.3	Bohm Sheath Criterion	13
1.5	Ion Dynamics	14
1.5.1	Child-Langmuir Sheath Representation	14
1.5.2	Time-Dependent Child-Langmuir Representation	15
1.5.3	Monte Carlo Simulations and Random Numbers	16
1.6	Non-Ionised Components in Reactor Gases	18
2	Ion Dynamics I	20
2.1	Oscillating Child-Langmuir Expression	21
2.2	Trajectories	22
2.3	Monte Carlo Method	25
2.3.1	Further Results	25
2.3.2	Polar Contours of Impact Energy	30
2.4	Phase Dependence	32
2.5	Spiral Description	35
2.5.1	Implementation	36
2.5.2	Variation with Sheath Parameters	36
2.5.3	Spiral Function Shape	39
2.5.4	Selection of Initial Phase	39
3	Ion Dynamics II	42
3.1	Motivation	43
3.2	Full Non-Linear Solution	43
3.3	Sheath Extent	44
3.4	Numerical Model	46

Contents	ix
3.4.1 Program Description	46
3.5 Results	47
3.5.1 Ion Trajectories	47
3.5.2 Ion Energy Distributions	48
3.5.3 Polar Plots of Parameter Space	50
3.6 Discussion	50
3.7 Outstanding Issues	56
4 Neutral Dynamics: Dielectrophoresis (DEP)	57
4.1 Background	58
4.2 Dielectrophoresis	58
4.3 Application to Plasma Processing	59
4.4 Model trench calculation	59
4.5 Numerical Simulation	62
4.5.1 Equation of Motion	62
4.5.2 Non-dimensional Representation	63
4.6 Results	63
4.6.1 At Aspect Ratio of 4	63
4.6.2 Variation in Aspect Ratio	70
4.7 Discussion	77
4.8 More Complete Potential Calculation	78
4.8.1 Discussion of Graphical Results	80
4.8.2 Simulation Results	85
4.9 Change in Electric Field with Aspect Ratio	85
4.10 Comparison of DEP models	90

5	Conclusions, Future Work and Speculation	96
5.1	Summary	97
5.2	Future Work	98
5.2.1	Ion Dynamics	98
5.2.2	Dielectrophoresis	98
5.3	Speculation	99
5.3.1	General Application of Spiral Observation	99
5.3.2	Non-Sinusoidal Driving Voltages	99

List of Figures

1.1	Anisotropic and isotropic etching	3
1.2	Influence of long range forces in a plasma	4
1.3	Simple representation of plasma processing system	7
1.4	Electrical state of substrate	8
1.5	Generalised particle motion and charge distribution	9
1.6	Coordinate system for sheath description	12
1.7	Generating non-uniform deviates	18
2.1	Contrasting ion trajectories	23
2.2	Ions entering sheath at different regions of cycle phase	24
2.3	Ion energy distribution (IED) of argon in reactor at 13.56MHz	26
2.4	Ion energy characteristics seen with Child-Langmuir sheath, $\eta \ll 1$	27
2.5	Ion energy characteristics seen with Child-Langmuir sheath, $\eta = 1$	28
2.6	Ion energy characteristics seen with Child-Langmuir sheath, $\eta \gg 1$	29
2.7	IED's and energy plots	31
2.8	Distribution of data points in figure 2.7	32
2.9	Polar plot of ion energy, $\eta \ll 1$	33
2.10	Polar plot of ion energy, $\eta = 1$	34
2.11	Polar plot of ion energy, $\eta \gg 1$	34
2.12	Example spiral plot	35

2.13 Development of the analytic spiral 37

2.14 Extracted IED 37

2.15 Analytic spiral when $n = 2$ 38

2.16 Analytic spiral when $n = 5$ 38

2.17 Analytic spiral when $n = 15$ 39

2.18 IED's at different n 40

3.1 Sheath extent 45

3.2 Ion trajectory, full sheath equation, $\eta \ll 1$ 48

3.3 Ion trajectory, full sheath equation, $\eta = 1$ 49

3.4 Ion trajectory, full sheath equation, $\eta \gg 1$ 49

3.5 Ion energy characteristics seen with full sheath equation, $\eta \ll 1$ 51

3.6 Ion energy characteristics seen with full sheath equation, $\eta = 1$ 52

3.7 Ion energy characteristics seen with full sheath equation, $\eta \gg 1$ 53

3.8 Polar plot of ion energy, full sheath equation, $\eta \ll 1$ 54

3.9 Polar plot of ion energy, full sheath equation, $\eta = 1$ 54

3.10 Polar plot of ion energy, full sheath equation, $\eta \gg 1$ 55

4.1 Geometry of large aspect ratio trench 60

4.2 Particles ejected perpendicular to the bottom of the trench, $\beta = 1$ 64

4.3 Particles ejected perpendicular to the bottom of the trench, $\beta = 10$ 65

4.4 Particles ejected perpendicular to the bottom of the trench, $\beta = 100$ 66

4.5 Particles ejected at 45° to the bottom of the trench, $\beta = 1$ 67

4.6 Particles ejected at 45° to the bottom of the trench, $\beta = 10$ 68

4.7 Particles ejected at 45° to the bottom of the trench, $\beta = 100$ 69

4.8 Particles ejected perpendicular to the bottom of a trench with aspect ratio = 2 71

4.9	Particles ejected perpendicular to the bottom of a trench with aspect ratio = 8	72
4.10	Particles ejected perpendicular to the bottom of a trench with aspect ratio = 16	73
4.11	Particles ejected at 45° to the bottom of a trench with aspect ratio = 2	74
4.12	Particles ejected at 45° to the bottom of a trench with aspect ratio = 8	75
4.13	Particles ejected at 45° to the bottom of a trench with aspect ratio = 16	76
4.14	Cross-section of potential	79
4.15	Electric field strength in trench, $n = 1$	81
4.16	Electric field strength in trench, $n = 27$	82
4.17	DEP force when $n = 1$	83
4.18	DEP force when $n = 27$	84
4.19	Numerical model, particles ejected perpendicular to trench bottom, $\beta = 1$	86
4.20	Numerical model, particles ejected perpendicular to trench bottom, $\beta = 100$	87
4.21	Numerical model, particles ejected at 45° to trench bottom, $\beta = 1$. . .	88
4.22	Numerical model, particles ejected at 45° to trench bottom, $\beta = 100$. .	89
4.23	Electric field in whole trench with aspect ratio = 2	91
4.24	Electric field in selected regions of trench with aspect ratio = 2	92
4.25	Electric field in whole trench with aspect ratio = 8	93
4.26	Electric field in selected regions of trench with aspect ratio = 8	94

Symbols and Acronyms

Symbols

m_e Electron mass (9.109×10^{-31} kg)

m_p Proton mass (1.673×10^{-27} kg)

m_i Ion mass

n_i Ion number density

n_e Electron number density

λ_d Debye length

ω_p Electron plasma frequency

k_B Boltzmann constant (1.381×10^{-23} JK⁻¹)

e Electron charge (1.602×10^{-19} C)

ϵ_0 Permittivity of a vacuum (8.854×10^{-12} Fm⁻¹)

T_e Electron temperature

T_i Ion temperature

eV Electron-volt (1.602×10^{-19} J)

ϕ Electric potential

\mathbf{E} Electric field

J_0 Ion current

ρ Charge density

θ Phase

χ Characteristic potential energy

\mathcal{L} Characteristic length

\mathcal{M} Characteristic kinetic energy

η Characteristic ion transit parameter

\mathbf{p} Electric dipole moment

a Trench width

d Trench depth

α Aspect ratio

ξ Characteristic trench width

ζ Characteristic trench depth

β Characteristic parameter of dielectrophoresis force

τ Characteristic time

Acronyms

DEP Dielectrophoresis.

IED Ion energy distribution.

IEDF Ion energy distribution function.

Chapter 1

Introduction

1.1 Development of Electronic Devices

The basic building blocks of electronic circuits have changed beyond recognition over the course of the last century. In order to create the electronic circuits which are ubiquitous in all aspects of modern life, it is necessary to utilize an element which can amplify electrical signals. Thomas Edison made the first step toward achieving this when he inserted a metal plate into one of his incandescent bulbs, finding that a current would only flow if the plate was positive with respect to the filament. John Ambrose Fleming was given some of these bulbs by Edison in 1889, yet it wasn't until 1904 that he appreciated the usefulness of this rectifying property. He was able to measure the strength of radio signals by using Edison's valve as what is now known as a diode, to rectify the signal, thus allowing it to be measured on a galvanometer. Lee De Forest added a metal grid to the valve in 1906 which could be used to control the flow of current between the main electrodes in the tube. This device is the triode valve and is an amplifying device which was used by AT&T in their coast to coast phone system of 1914. The development of these devices has had a huge influence on many aspects of the twentieth century [1; 2].

A new amplifying device began to replace the thermionic valve during the 1950's. Although the valve had obviated most problems relating to the crystals used for radio sets, a number of people continued research into understanding and improving the quality of these crystals. In 1948 while working for Bell Labs, William Shockley understood enough to be able to devise the junction transistor. Having established his ideas, the first functional device was produced in 1950. The advent of 'solid state', transistor-based circuits provided many benefits over the valve equivalents by ultimately reducing cost, power consumption, complexity and size, while also increasing reliability.

Taking a step back from the transistor for a moment, the simplest useful semiconducting component is the diode. If crystalline silicon or germanium has small amounts of impurities added to them they form the basic p-type and n-type materials which constitute all semiconducting devices. A simple interface between p- and n-type material forms a diode; this will allow current to pass in one direction, but not the other. A junction between n- p- and n-type or p- n- and p-type material forms the transistor, which is the amplifying device crucial to all microelectronic products today. Initial production of components relied purely upon chemical techniques to dope silicon or germanium to form these junctions.

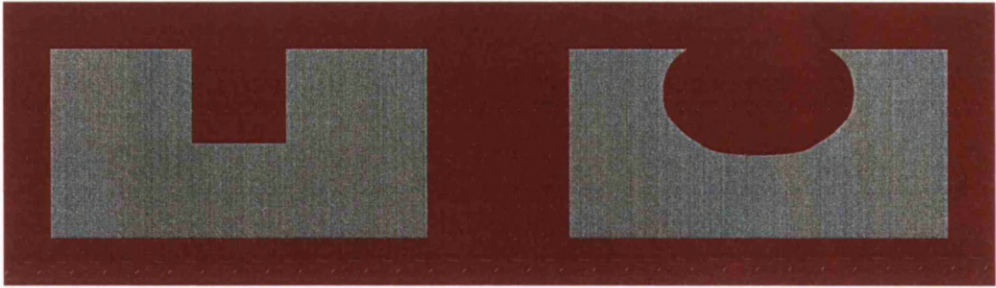


Figure 1.1: Comparing anisotropic (left) and isotropic (right) etching.

Integrated circuits consist of a great number of transistors and other devices, all constructed and interconnected on one substrate. The first working examples were produced independently by Jack Kilby at Texas Instruments and Robert Noyce at Fairchild Semiconductor in 1958 and 1959 respectively. When integrated circuits were first produced and for many years subsequently, the requisite etch and growth stages were achieved chemically. Chemical processes are characterised by a uniform rate on all exposed surfaces. This isotropic manner of progress impedes the ability to form steep-sided high aspect-ratio features, instead rounded substrate features are formed (figure 1.1). In order to fabricate silicon chips with higher densities of transistors it is necessary to produce substrate features that are as sharply defined as possible.

Although not a primary motive for developing plasma processing methods, it is noted that chemical treatments also consume and result in undesirable toxic materials.

1.2 Defining a Plasma

Before examining plasmas used for the processing of materials, it is useful to look at what characterises a plasma. There are two concepts which provide a definition of a plasma, these are quasineutrality and collective behaviour.

1.2.1 Collective Behaviour

In a gas with insignificant ionisation, molecular motion is governed by interactions which take place during collisions. As the level of ionisation increases, forces due to the presence of charged particles become significant and then dominate.

The Coulomb force between two regions of charge separated by r decreases as $1/r^2$,

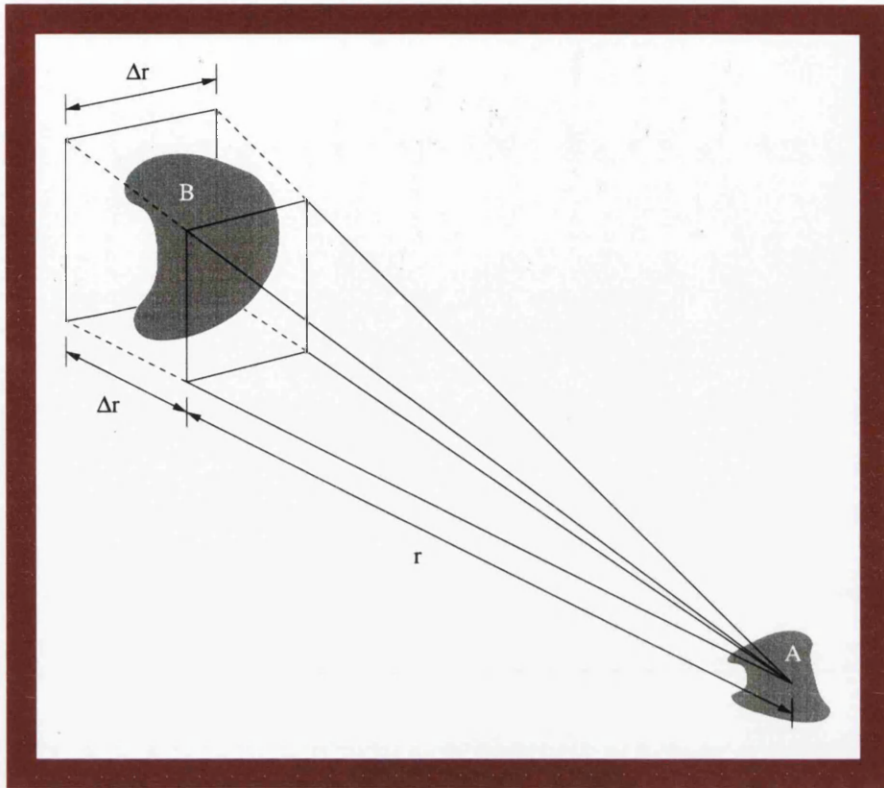


Figure 1.2: Influence of long range forces in a plasma.

this alone would mean that forces are not experienced at great distances. However, the volume of a region of charge in a solid angle at distance r increases as r^3 , which allows elements of a plasma to affect each other at great distances (figure 1.2). This leads to the collective behaviour which is responsible for some of the interesting properties of plasmas.

1.2.2 Quasineutrality

While long range forces exist in a plasma, it is not possible to set up any static electric fields beyond a certain distance from an electric charge perturbation. This distance is the length in which electrons can shield the charge from the plasma bulk and is known as the Debye radius. Note that electrons carry out the shielding as ions are too massive to move in the necessary timescales.

In order to approximate a value for the Debye length λ_D , we use Poisson's equation in one dimension,

$$\frac{d^2\phi}{dx^2} = -\frac{e}{\epsilon_0}(n_i - n_e). \quad (1.1)$$

Since the ions are stationary with respect to the timescale here, $n_i = n_\infty$, where n_∞ is the density of the plasma bulk.

From the Boltzmann collision integral, the electron distribution function can be determined,

$$f(u) = A \exp[-(\frac{1}{2}mu^2 + q\phi)/k_B T_e], \quad (1.2)$$

where the $q\phi$ term arises from the potential energy of the charge. For a finite plasma bounded by a vessel, there is not complete charge neutrality in the plasma bulk. However, consider that when $\phi \rightarrow 0$, $n_e = n_\infty$ and that $q = -e$, then integrate $f(u)$ over u ,

$$n_e = n_\infty \exp(e\phi/k_B T_e). \quad (1.3)$$

Putting this into (1.1),

$$\frac{d^2\phi}{dx^2} = \frac{en_\infty}{\epsilon_0} \left\{ \left[\exp\left(\frac{e\phi}{k_B T_e}\right) \right] - 1 \right\}. \quad (1.4)$$

The potential falls very rapidly adjacent to the charge and so this region contributes a negligible thickness to the shielding. Elsewhere it is the case that $|e\phi/k_B T_e| \ll 1$, allowing the exponential to be expanded in a Taylor series

$$\frac{d^2\phi}{dx^2} = \frac{en_\infty}{\epsilon_0} \left[\frac{e\phi}{k_B T_e} + \frac{1}{2} \left(\frac{e\phi}{k_B T_e} \right)^2 + \dots \right]. \quad (1.5)$$

Taking the linear term from (1.5)

$$\frac{d^2\phi}{dx^2} = \frac{en_\infty}{\epsilon_0} \frac{e\phi}{k_B T_e} \quad (1.6)$$

From this we define the Debye length as the e-folding distance

$$\lambda_D \equiv \left(\frac{\epsilon_0 k_B T_e}{ne^2} \right)^{1/2}, \quad (1.7)$$

where $n = n_\infty$, the bulk plasma density.

In order to be considered a plasma, an ionised gas must satisfy the requirement of quasineutrality. To be quasineutral, the volume that the gas occupies must have dimensions (L) much greater than the Debye length, ie. $\lambda_D \ll L$.

1.2.3 Plasma Frequency

Another important plasma parameter is the *electron plasma frequency*, often simply called the *plasma frequency*, ω_p . If electrons in a plasma are displaced, the resulting

charge imbalance sets up an electric field that acts to restore the electrons to their original position. Because of their inertia the electrons overshoot this position, again setting up an electric field and so on. The characteristic frequency at which this occurs can be written:

$$\omega_p = \left(\frac{e^2 n_0}{\epsilon_0 m_e} \right)^{1/2}. \quad (1.8)$$

This parameter is solely dependent on plasma density, n_0 .

It is important in the context of the work that follows that the frequency that the plasma is driven at is less than the plasma frequency. If this condition is obeyed, then the electrons in the plasma can respond to an imposed potential and shield the plasma bulk. This allows the formation of sheaths, which are crucial to the following work and will be discussed in due course.

1.3 Plasma Processing

1.3.1 Plasma Processing as a Tool

Plasma processing methods have provided the means to address the need to fabricate substrate features on an increasingly small scale by acting on a substrate in a fundamentally different way to preexisting material processing techniques. Steep sided (often referred to as anisotropic) features can readily be formed.

In order to explain the advantages of plasma processing let us consider the system as having two main features. Firstly, a supply of ionised molecules or atoms and secondly, an electric field across which the ions can be accelerated. Ions are available within a vessel and the substrate to be worked is at the vessel wall. The electric field is perpendicular to the substrate, with the polarity of the field such that ions are accelerated from the edge of the plasma toward the substrate (figure 1.3). This situation will result in a flux of ions striking the substrate, with individual energies that depend on a number of parameters in the system.

The stream of ions impinging upon the substrate can have a range of effects when they strike the surface. This will depend upon both the energy of the ion and the chemical properties of the system. The substrate may be unaffected, layers of incoming ions could build up onto the substrate, ions can be implanted into the crystal lattice or material may be removed from the substrate. Extreme ion energies may actually cause

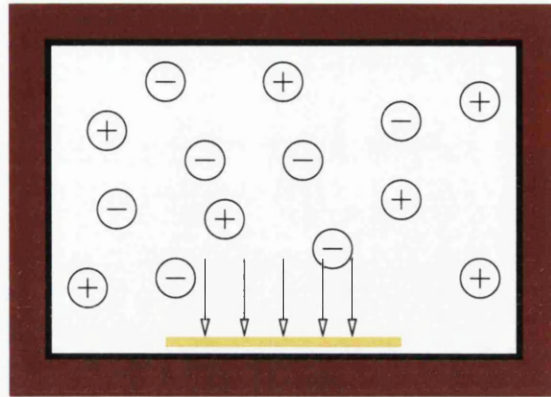


Figure 1.3: Simple representation of plasma processing system: a vessel containing ions and electrons and a substrate with an electric field directed perpendicularly to it.

undesirable damage to the substrate [3]. Control of the ion energy is crucial to a plasma processing system, so that consistent and desirable results may be achieved. A great deal of experimental [4; 5; 6; 7; 8; 9] and theoretical [10; 11; 12; 13; 14; 15; 16] work has been carried out to this end. When a silicon wafer is produced with many integrated circuits upon it, the vast majority are unusable. Improvement of ion control is one way to improve this situation.

The crucial difference between this operating regime and a chemical process is that the ions are striking the substrate perpendicularly rather than a process taking place on all exposed surfaces. This means that as (for example) a trench develops, it is the bottom that continues to be etched and not the walls.

1.3.2 Plasma Characteristics

To sustain a plasma, energy must be put into the reactor vessel. In many cases the radio frequency electric field is coupled to the plasma by either inductive or capacitive means. Some additional heating can be supplied by exploiting electron cyclotron resonance (ECR) and magnets can provide additional confinement. The proportion of ions created is around 1 in 10^{-4} , other particles remaining uncharged. This partial ionisation means that the plasma is not in thermal equilibrium, but three distinct groups of particles exist.

Most of the energy put into the vessel causes the heating of electrons, while the ions gain a little energy and the neutrals stay close to ambient temperature. If we consider

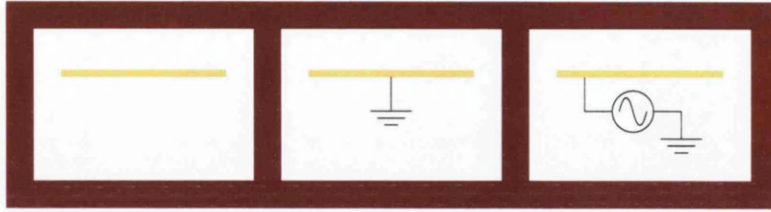


Figure 1.4: Substrate can be (left to right) floating, grounded or externally driven.

a stationary singly-charged particle with mass m in an electric field E , it can be shown that in time t the particle gains energy [17]

$$\text{Energy} = \frac{(Eet)^2}{2m}. \quad (1.9)$$

Given that $m_i \gg m_e$, most of the energy will be given to the electrons. Three separate energy distributions then exist in the plasma, one for electrons at around 2eV, one for ions a little above ambient ($\approx 1/20\text{eV}$) and neutrals remain around 1/40eV (290K).

When the energetic electrons have inelastic collisions with atoms, *electron impact ionisation* takes place which makes a major contribution to sustaining the plasma.

1.3.3 Sheath Characteristics

Surfaces around the vessel can be in three different electrical conditions, one of floating, grounded or externally driven (figure 1.4). In either case a region will form between the plasma bulk and the surface, where the flux of ions and electrons and any current through the surface must balance. This is referred to as a Sheath Region.

Each condition can be examined if we consider that the electrons have a much greater energy than ions and consequently a correspondingly higher flux to any surface bounding the plasma.

- An initially uncharged floating surface will collect electron charge and begin to repel the incoming electron flux. This creates a space charge between the plasma bulk and the surface.
- There will initially be a higher flux of electrons to a grounded surface. The electrons will flow to ground until the plasma cannot sustain any further outward electron current. The reduction of electron density in the plasma results in a space charge between the plasma and the surface.

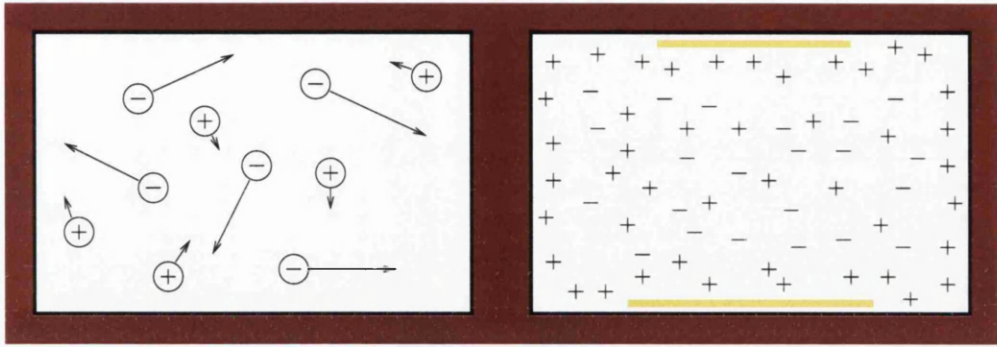


Figure 1.5: Generalised particle motion and charge distribution. In the left panel it is shown that ions move more slowly than electrons. In the right panel, the reduction in the number density of electrons at the vessel walls is shown.

- Applying a voltage to a surface will modify the balance between the electron current from the plasma and the current resulting from the applied voltage. A schematic description of these conditions is given in figure 1.5.

In any case the plasma will adjust to keep the system in equilibrium and a space charge will form between the plasma and the surface. Poisson's equation relates the variation of potential, ϕ with distance x across a space charge density ρ . In one dimension this is:

$$\frac{d^2\phi}{dx^2} = -\frac{\rho}{\epsilon_0}. \quad (1.10)$$

further,

$$E = -\frac{d\phi}{dx} \quad (1.11)$$

so

$$\frac{dE}{dx} = \frac{\rho}{\epsilon_0}. \quad (1.12)$$

In the absence of any perturbations such as that produced by a surface in the plasma, there are no variations in the electric field within the plasma. Relative to a surface in any electrical configuration, the plasma bulk can be assigned a potential which is more positive than the surface. This is called the *plasma potential* and can only be measured relative to parts of the vessel under different electrical conditions.

1.3.4 Reactor Operational Summary

The substrate which is to be worked is placed on a plinth in the reactor chamber. A plasma is induced in the chamber and sustained by some input of power, depending

upon the reactor type. The process is allowed to continue until some pre-determined end point is reached.

Reactor vessels are arranged so that feedstock gases can flow into the chamber as exhaust gases are pumped out. Controlled pumping allows the pressure in the chamber to be reduced to the appropriate operating conditions. This flow of gases constitutes a macroscopic flow which can be of importance to the uniformity of the process. This is particularly the case when working on substrates with a large surface area. There can be implications on the macroscopic flow due to the geometry of the reactor vessel.

1.3.5 Types of Reactor

There are many types of reactor for generating a plasma [18], but two basic types of plasma are generated for plasma processing. Presently the most widely used is a high pressure ($1\text{-}10^3$ Pa) low density ($10^{15}\text{-}10^{16}$ m^{-3}) plasma produced by a capacitively coupled (rf diode) type reactor. A pair of parallel electrodes are driven at a radio frequency of typically 13.56MHz to sustain the plasma. There is no technical reason for the use of this particular frequency, but it is allocated for this purpose by international electromagnetic interference regulatory authorities. The other type is a low pressure (0.1 Pa), high density ($10^{18}\text{-}10^{19}$ m^{-3}) plasma which is becoming increasingly popular due to the higher degree of control that can be exercised over the plasma. A number of different reactor configurations can produce this type of plasma, electron-cyclotron resonance (ECR); helicon; helical resonance and inductively coupled.

Capacitively Coupled Reactors

Capacitively coupled reactors have the advantage of being simpler to understand and implement than other types, making them a good starting point for study. It is also for this reason that they gained a strong foothold as practical machines for industrial use.

These reactors are characterised by a relatively low plasma density and high pressure. Low density means that there may be a shortage of the ionised particles necessary for the progression of the process in question. A high pressure will result in an increased probability of collisions, which will lead to a less anisotropic process.

The area of the electrodes in the reactor has an important effect upon the characteristics of the discharge. If symmetrical, there will be roughly half of the driving voltage

dropped across the sheath at each electrode. If the electrodes are made to be different sizes, then the relative voltage across each sheath will change in relation to this. The interrelated nature of geometry and electrical properties highlights some of the difficulties which are experienced with this type of reactor.

Since the ion impact energy is so important to the effect an ion has on the substrate, independent control of this parameter from other parameters is highly desirable. One method of achieving this is to apply a biasing voltage to the substrate, in order to manipulate the potential difference across the sheath region.

Other Reactor Types

Further developments have led to reactors which give considerably more independent control over the plasma parameters. The plasma density can be improved by using measures that provide more effective confinement or providing additional heating to the electrons via ECR [19].

1.3.6 Plasma Chemistry

The importance of the actual gases that are used in plasma processing systems can be vitally important to developing a useful system. In reactive ion etching (RIE) systems, a feedstock gas (for example CF_4) chemically activates the substrate surface so that the atoms are loosened and etching can progress at a lower ion impact energies. Other gases are added to moderate the process or to assist in the conversion of removed material into molecules that can easily pass through the reactor. The gas composition is adjusted to yield the best results; this knowledge will be a closely guarded industrial secret.

The precise nature of the removed particles is difficult to determine and various studies have tried to address issues around this topic. A review by Hancock [20] discusses the diagnostics of active species in plasmas. Laser induced fluorescence is used in [21; 22; 23; 24] to examine fluorine and chlorine product lifetimes and density. Etching yields and product formation measurements are reported by Kubota(1998) and Kroesen(1998) [25; 26]. Theoretical models of reaction products and rates have been made by Laganà(1997) and Martišovitš(1997) [27; 28]. These articles show that the environment in which plasma processing takes place is not sympathetic to developing a clear understanding of the chemical processes that happen.

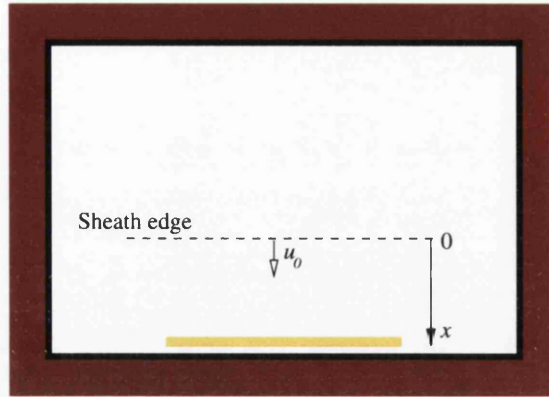


Figure 1.6: Coordinate system for sheath description. $x = 0$ is defined as the sheath edge and u_0 is the speed of an ion when it enters the sheath region.

1.4 Planar Sheath Representation

So some basic knowledge about plasmas and plasma processing has been introduced. A large part of this thesis is concerned with how particles behave when they interact with the sheath region between the plasma bulk and the vessel walls. The sheath region will be the focus of interest from this point forward.

1.4.1 Describing the Sheath Region

To start an investigation of the plasma sheath we must make some assumptions which allow us to express the problem more simply. A schematic representation of the coordinate system in use is shown in figure 1.6. Firstly we assume that there are no collisions in the sheath, so we can give ion energy conservation as [29]:

$$\frac{1}{2}mu^2(x) = \frac{1}{2}mu_0^2 - e\phi(x), \quad (1.13)$$

where u_0 is the velocity at the sheath edge. Secondly, if there is no ionisation in the sheath, the continuity of ion flux is:

$$n_i(x)u(x) = n_0u_0, \quad (1.14)$$

where n_0 is the ion density at the sheath edge.

From these basic equations we see in the next section how we can begin to express properties of the sheath.

1.4.2 General Sheath Representation

To describe the sheath a similar process is followed as for deriving the the Debye length, λ_D . The Debye radius defines the sheath for a point charge, expressing a planar sheath is not entirely dissimilar.

Rearranging (1.13)

$$u = \left(u_0^2 - \frac{2e\phi}{m} \right)^{1/2}, \quad (1.15)$$

and inserting this into (1.14)

$$n_i(x) = n_0 \left(1 - \frac{2e\phi}{mu_0^2} \right)^{-1/2}, \quad (1.16)$$

gives the ion density through the sheath region $n_i(x)$ in terms of the density in the main plasma n_0 .

The electron density $n_e(x)$ can be expressed as in (1.3)

$$n_e(x) = n_0 \exp(e\phi/k_B T_e). \quad (1.17)$$

Substituting (1.16) and (1.17) into the Poisson equation (1.10)

$$\frac{d^2\phi}{dx^2} = \frac{e}{\epsilon_0} (n_e - n_i) = \frac{en_0}{\epsilon_0} \left[\exp\left(\frac{e\phi}{k_B T_e}\right) - \left(1 - \frac{2e\phi}{mu_0^2}\right)^{-1/2} \right]. \quad (1.18)$$

Changing the notation more clearly reveals the structure of this equation

$$\chi \equiv -\frac{e\phi}{k_B T_e} \quad \mathcal{L} \equiv \frac{x}{\lambda_D} = x \left(\frac{n_0 e^2}{\epsilon_0 k_B T_e} \right)^{1/2} \quad \mathcal{M} \equiv \frac{u_0}{(k_B T_e / m_i)^{1/2}} \quad (1.19)$$

This allows (1.18) to be written

$$\chi'' = \left(1 - \frac{2\chi}{\mathcal{M}^2} \right)^{-1/2} - e^{-\chi} \quad (1.20)$$

where the prime denotes $d/d\mathcal{L}$.

1.4.3 Bohm Sheath Criterion

In order to satisfy the equations that follow, ions must be travelling at a velocity above their thermal velocity as they enter the sheath region. This criterion was recognised by Bohm [30] and in view of more recent ideas is given thorough treatment in [31]. In a simple sheath model the wall disturbance is said to have been shielded by the sheath, so the electric field in the plasma at the edge of the sheath is zero. With no electric field

there is no mechanism to accelerate ions to the necessary velocity to allow a sheath to form consistently. It can be shown how this problem arises by integrating (1.20)

$$\int_0^{\mathcal{L}} \chi' \chi'' d\mathcal{L} = \int_0^{\mathcal{L}} \left(1 - \frac{2\chi}{\mathcal{M}^2}\right)^{-1/2} \chi' d\mathcal{L} - \int_0^{\mathcal{L}} e^{-\chi} \chi' d\mathcal{L} \quad (1.21)$$

Since $\chi = 0$ at $\mathcal{L} = 0$

$$\frac{1}{2}(\chi'^2 - \chi_0'^2) = \mathcal{M}^2 \left[\left(1 + \frac{2\chi}{\mathcal{M}^2}\right)^{1/2} - 1 \right] + e^{-\chi} - 1 \quad (1.22)$$

and since $\mathbf{E} = 0$ in the plasma, $\chi'_0 = 0$ at $\mathcal{L} = 0$.

In order to make sense physically, the right hand side of (1.22) must be positive for all \mathcal{L} . Looking at the plasma-sheath interface, where $\chi \ll 1$, the right hand side of (1.22) can be Taylor expanded

$$\mathcal{M}^2 \left[1 + \frac{\chi}{\mathcal{M}^2} - \frac{1}{2} \frac{\chi^2}{\mathcal{M}^4} + \dots - 1 \right] + 1 - \chi + \frac{1}{2} \chi^2 + \dots - 1 > 0 \quad (1.23)$$

$$\frac{1}{2} \chi^2 \left(-\frac{1}{\mathcal{M}^2} + 1 \right) > 0 \quad (1.24)$$

For this inequality to hold, it must be the case that

$$\mathcal{M}^2 > 1 \quad \text{or} \quad u_0 > \left(\frac{k_B T_e}{m_i} \right)^{1/2} \quad (1.25)$$

This result proves to be a difficulty because the requirement that ions are accelerated before reaching the sheath region contradicts the assumption that $\chi' = 0$ at $\mathcal{L} = 0$. Although this needs to be borne in mind when justifying assumptions and results, the work in this thesis does not tackle this problem.

1.5 Ion Dynamics

Here the necessary components of what has been discussed will be put into the specific context of ion dynamics in the sheath of a processing plasma. The Monte Carlo approach to modelling will also be introduced.

1.5.1 Child-Langmuir Sheath Representation

When the electrodes are driven by an external voltage, the sheath potential is often considerably higher than the electron energy T_e . In these conditions there are no electrons

in the sheath and the ion energy at the sheath edge is small compared to the sheath potential. The latter allows simplification of equations (1.13) and (1.14):

$$\frac{1}{2}m_i u^2(x) = -e\phi(x) \quad (1.26)$$

$$en(x)u(x) = J_0. \quad (1.27)$$

where J_0 is the ion current. Rearranging (1.26) and substituting for $u(x)$ in (1.27):

$$n(x) = \frac{J_0}{e} \left(-\frac{2e\phi}{m_i} \right)^{-1/2} \quad (1.28)$$

Using this in Poisson's equation (1.10):

$$\frac{d^2\phi}{dx^2} = -\frac{J_0}{\epsilon_0} \left(-\frac{2e\phi}{m_i} \right)^{-1/2}. \quad (1.29)$$

Multiplying both sides by ϕ' and integrating

$$\int_0^x \frac{d^2\phi}{dx^2} \frac{d\phi}{dx} dx = \int_0^x \frac{d\phi}{dx} \frac{J_0}{\epsilon_0} \left(\frac{2e\phi}{m_i} \right)^{1/2} dx \quad (1.30)$$

$$\frac{d\phi}{dx} = -2 \left(\frac{J_0}{\epsilon_0} \right)^{1/2} \left(\frac{2e}{m_i} \right)^{-1/4} \phi^{1/4} \quad (1.31)$$

Integrating once more and rearranging

$$\int_0^x \frac{d\phi}{dx} dx = -2 \left(\frac{J_0}{\epsilon_0} \right)^{1/2} \left(\frac{2e}{m_i} \right)^{-1/4} \int_0^x \phi^{1/4} dx \quad (1.32)$$

$$\phi(x) = \left(\frac{9J_0}{4\epsilon_0} \right)^{2/3} \left(\frac{m_i}{2e} \right)^{1/3} x^{4/3} \quad (1.33)$$

1.5.2 Time-Dependent Child-Langmuir Representation

The Child-Langmuir Law is derived for a DC sheath, so is a steady state solution. Since processing plasmas are largely AC, operating at 13.56MHz, is this sheath equation of any relevance to the plasmas which are being discussed here? The Child-Langmuir Law *has* been widely applied to AC sheaths, which requires some justification. If the sheath were to be looked at in a snapshot of time, the question is, are the particles in this snapshot behaving as they would if this were the steady state DC sheath? It is argued that the electrons are so mobile as to follow the potential variations instantaneously and the ions are so slow to respond that their paths continue as normal.

1.5.3 Monte Carlo Simulations and Random Numbers

Since the advent of the first electronic computer in the 1940's it became possible to carry out large numbers of calculations with comparative ease. Stanislaw Ulam had been considering how to evaluate the chances of different outcomes occurring in a system, for example will a game of solitaire be successful or not? It was apparent that it would be more efficient to play the game a sufficient number of times to have a confident prediction of the chance of success, rather than to try to devise and solve a series of equations describing the game. This example highlights the origins of the name which is due to the connection with games of chance that can be found in the casinos of which Monte Carlo is renowned. While working on The Manhattan Project at Los Alamos, Stanislaw Ulam and John von Neumann were aware of the ENIAC electronic computer and understood its potential to perform the necessary calculations for a Monte-Carlo-based experiment [32].

It is recognised that Enrico Fermi was using the Monte Carlo technique to predict experimental results with uncanny accuracy up to fifteen years before it was given a name and published by Ulam and von Neumann.

To carry out a Monte Carlo simulation in an experiment, such as understanding neutron diffusion in fissionable material, von Neumann's originally proposed application, a single entity is followed during the time of interest. Equations are applied during the lifetime and a history of the entity's behaviour is established. This is repeated with as many entities as required to provide a reliable representation of the real system.

For at least one point in the experiment a number will need to be drawn from a distribution, for example an energy from a Maxwellian temperature distribution. This leads to a crucial aspect of the Monte Carlo Method, which is the need to produce random numbers. More accurately, it is necessary to produce a sequence of numbers which appear random in the context of the experiment which is being performed. The random number sequence must introduce no bias to the results. The production of truly random numbers is invariably very difficult and time consuming. Typical starting points for this task are radioactive sources or electrical noise. Two techniques are much more readily applied to computer-based problems, the generation of *pseudo-random* and *quasi-random* number sequences.

Pseudo-random sequences are commonly generated using the recursive linear-

congruential or Lehmer generator [33]. A simple formula is used to calculate the next integer in the sequence,

$$x_{n+1} = Ax_n + C \pmod{M}, \quad (1.34)$$

where x_n is the n th number in the sequence and A , C and M are integers which are chosen to suit the particular application. Usually this means maximising the number of calls before the sequence repeats itself, which in the best case will be M calls. To obtain real numbers in the range 0 to 1, x_{n+1}/M is returned. This method is quick, but the sequence will repeat itself and in any case this method is frequently poorly implemented. With a numerical recipes [34] library available, this is a preferable option.

In reality quasi-random sequences are anything but random, they are carefully structured to obey certain rules. When wanting to ‘randomly’ sample points on a grid, a truly random generator will tend to provide numbers that bunch together until a sufficiently high quantity of numbers has been generated. In order to reduce the quantity, a pre-determined sequence of numbers that appear random to the problem in hand yet also realistically cover the whole parameter space is used. Quasi-random sequences are applied when using the Monte Carlo Methods to numerically evaluate integrals.

A random number generator returns *uniform deviates*, that is to say numbers evenly distributed, usually between 0 and 1. Often a different distribution, such as binomial, Poisson or Gaussian will be required. A rejection method can be used to provide these alternative deviates. The procedure for this is as follows (refer to figure 1.7):

- A uniform deviate x , is generated by the selected method. For this example the range would be 0 to 3.
- A distribution function $f(x)$ is evaluated.
- A second uniform deviate j , is generated, this time in the range 0 to 1, and is compared with $f(x)$.
- If $j > f(x)$ then it is rejected and the process is repeated, otherwise x is returned.

As this process is repeated the desired distribution will be produced.

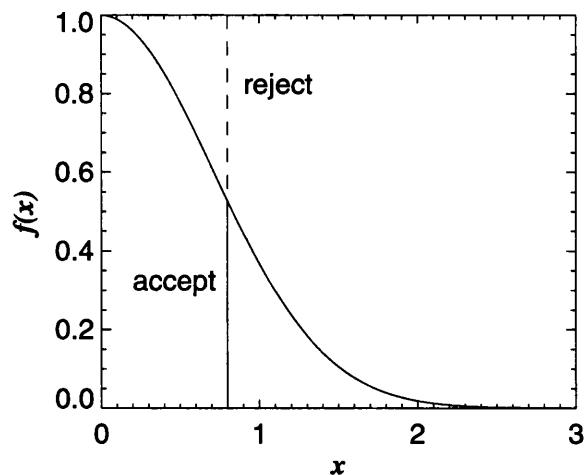


Figure 1.7: Generating non-uniform deviates by drawing two random numbers, x and j . The distribution function is evaluated at x and the result is compared with j . If j is less than $f(x)$, then x is accepted.

1.6 Non-Ionised Components in Reactor Gases

It has been pointed out that there is only a small degree of ionisation in a processing plasma. This means that there is a large proportion of neutral particles contributing to the total volume. Although the ionised component of the gas is clearly crucial to the progress of material processing, what influence do the neutral particles have in the system?

In reactive ion etching (RIE) systems, the composition of the gas is selected to optimise the chemical activity in the system.

The macroscopic flow of the neutral gas through the system is determined by the geometry and pumping arrangement in the vessel. The macroscopic flow is important as this carries with it the ionised portion of the gas. The delivery of ions to the edge of the sheath region is reliant on a steady and uniform circulation of the reactor gas.

A further mechanism for the transport of neutral particles is explored in depth in this thesis. Due to the sharply angled shapes on a substrate surface, large electric field gradients are found around these features. Molecules which are asymmetric in structure exhibit an electric dipole due to the distribution of charge across the molecule. If a dipole is placed in an electric field it will become aligned with the field lines. Further, if there is a gradient in the field, one end of the dipole will have a greater force exerted

upon it than the other, causing a molecule to move toward regions of increasing electric field. This phenomenon and the implications are discussed in §4.

Chapter 2

Ion Dynamics I

2.1 Oscillating Child-Langmuir Expression

The Child-Langmuir expression for space-charge-limited current in a plane diode provides useful insight for DC sheaths. It would be useful if we were able to apply this to a time-evolving AC sheath. Techniques have been applied which include the time-dependency in the driving voltage of the system [35; 36]. This results in a Child-Langmuir equation of the form

$$\phi(r, t) = \phi_p(t) - 3/4(en_i/\epsilon_0)^{2/3}(3k_B T_i/\pi e)^{1/3}[l(t) - r]^{4/3}. \quad (2.1)$$

In this expression $r = 0$ is at the electrode, $\phi_p(t)$ is the time-varying plasma potential, n_i the ion density, T_i the ion temperature and $l(t)$ the time-varying sheath thickness.

A few steps are required to describe $l(t)$. Firstly the potential difference between the plasma and the electrode, ϕ_{pe} is given in terms of the plasma potential, ϕ_p and the electrode potential, ϕ_e

$$\phi_{pe}(t) = \phi_p(t), \quad (\text{grounded electrode}) \quad (2.2)$$

$$\phi_{pe}(t) = \phi_p(t) - \phi_e(t). \quad (\text{driven electrode}) \quad (2.3)$$

In the case of the driven electrode, ϕ_e is a simple combination of the driving potential and a self-bias DC voltage ϕ_{dc} , arising due to unevenly-sized electrodes. Note that a small natural self-bias also occurs due to the the current-voltage characteristic of the plasma, see Sugawara [37] for an explanation of this.

$$\phi_e(t) = \phi_0 \sin(\omega t + \theta) - \phi_{dc}, \quad (2.4)$$

$$\phi_{dc} = \phi_0 \sin \left[\frac{\pi}{2} (A_a - A_c) / (A_a + A_c) \right], \quad (2.5)$$

where A_a and A_c are the anode and cathode surface areas respectively.

The plasma potential, ϕ_p is given by [35]

$$\begin{aligned} \phi_p(t) &= (k_B T_e / e) \ln \{ [1 + (A_c / A_a)] \\ &\quad \times \exp(e\phi_e(t) / k_B T_e) / [1 + (A_c / A_a)] \} + \phi_p^0, \end{aligned} \quad (2.6)$$

$$\phi_p^0 = (k_B T_e / 2e) \ln(\langle v_e \rangle / \langle v_i \rangle) \quad (2.7)$$

With the quantities above it is then possible to express the sheath extent, $l(t)$,

$$l(t) = l_0[\phi_{pe}(t)]^{3/4}, \quad (2.8)$$

$$\text{where, } l_0 = l_{max}/[\phi_{pe,max}]^{3/4}. \quad (2.9)$$

This covers all the quantities that are used in equation [2.1] which can then be used to calculate the motion of ions when they come into the influence of the sheath region by using the equation of motion:

$$\frac{d^2r}{dt^2} = \left(\frac{-e}{m_i}\right) \frac{\partial\phi(r,t)}{\partial r}. \quad (2.10)$$

2.2 Trajectories

Once this series of equations has been established, it is possible to follow the path of an ion through the sheath region. Following the trajectories of ions provides insight into their interaction with the acceleration mechanism they encounter in the sheath region. By changing initial parameters an understanding of the conditions that result in particular final energy levels can be achieved.

Two ion trajectories can be seen in figure 2.1. Two quantities are recorded as time progresses. The oscillating solid curve marks the extent to which the sheath penetrates into the plasma. The dot dash curve gives the distance of the ion from the substrate. Distance is expressed relative to the substrate.

During the periods of time that an ion is not under the sheath extent curve, there is no force on the ion so it continues to move with uniform speed. During the periods that the ion is under the sheath extent curve, acceleration is experienced. It is noted that the acceleration while under the curve is not constant, but depends upon both the extent of the sheath and the position of the ion within it.

The two distinct cases of trajectory in figure 2.1 show the extreme variations in energy acquisition for an ion. To understand how this comes about, observe where the ion strikes the substrate relative to the final sheath oscillation. In the case where a high impact energy is achieved, the ion strikes the substrate immediately prior to the collapse of the sheath. For a low impact energy the ion strikes immediately prior to the growth of the sheath.

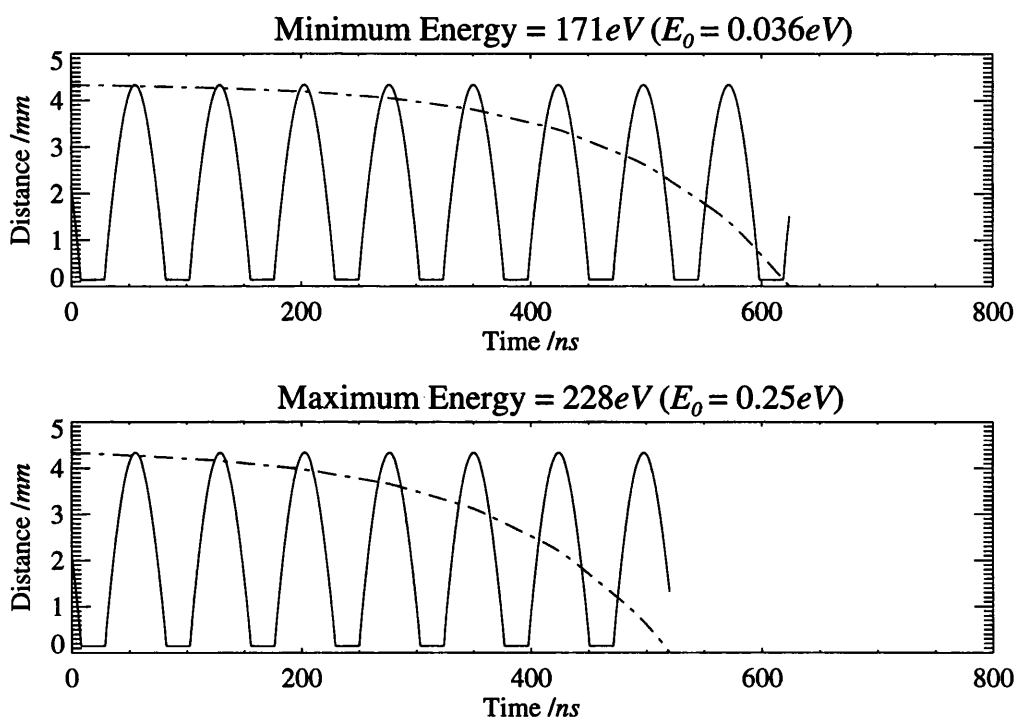


Figure 2.1: Contrasting ion trajectories. Minimum ion impact energy is achieved when the ion strikes the substrate just before the sheath begins to extend. This contrasts with maximum ion impact energy, which occurs when the ion strikes the substrate just as the sheath reduces to its minimum value. On the time scale of the driving voltage period the plasma does not become extinguished, so the plasma potential sustains a small sheath region during the sheath extent minimum.

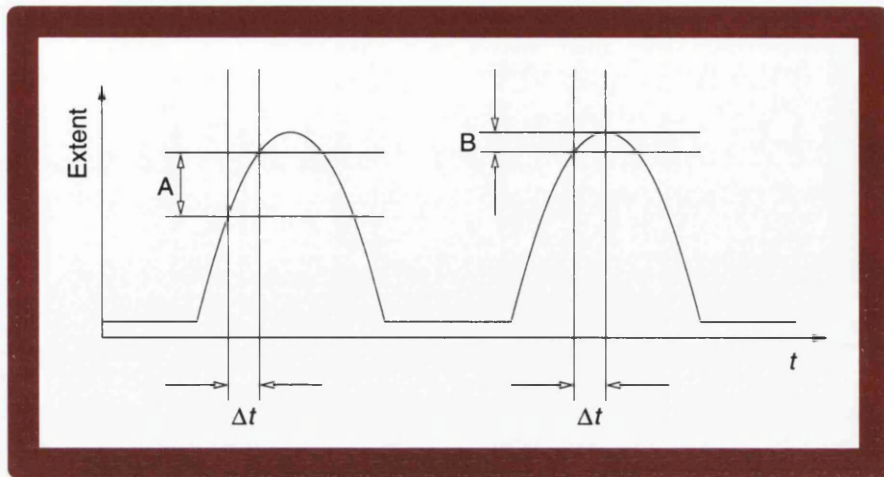


Figure 2.2: Effect of sheath shape on the number of ions entering at different sheath extents. If the same number of ions enter the sheath in each period Δt , the ions will be distributed across a greater range of sheath extent in case A than in case B.

As an ion approaches the substrate, the width of the sheath which the ion interacts with increases. Therefore the contribution from an individual sheath interaction to the total energy increase is higher when the ion is closer to the substrate surface. By spending the maximum amount of time being accelerated in the final part of the trajectory, the maximum overall energy acquisition is attained. Conversely, if an ion is drifting for the final stage of the trajectory, then the minimum impact energy is achieved. Intermediate values for ion impact energy are seen for cases between these two extremes.

So this accounts for the extremes of energy which can be attained. An appreciation of how these energies shift can also be acquired by considering a single trajectory. The number of sheath oscillation cycles before impact can be different for any combination of a number of reasons; driving frequency, initial ion velocity, ion mass, potential across sheath and sheath width. If an ion encounters a large number of sheath cycles before impact, the last sheath interaction will play a small part in the total energy gain across the whole sheath. All ions will therefore arrive with similar final energies. Where a small number of sheath cycles are encountered, the last encounter will account for practically the whole energy gain and this will be reflected in a broad range of possible energies. Ions whose characteristics fall between these two extremes will achieve an intermediate energy gain.

Some information about the number of ions terminating at each energy can also be seen, giving a qualitative prediction of the ion energy distribution. Since the sheath

potential (approximately) follows the shape of a half wave rectified sinusoid, there are steep rising and falling sides with a more slowly turning crest. Assuming that ions are delivered to the sheath edge at a constant rate in time, more ions will enter the sheath where the potential is changing more slowly, so tending to group the ions at one or two energies. Looking at figure 2.2 it can be seen that for two equally sized time periods (Δt) there is a greater range of sheath extent that can be entered on the steep slope of rising curve, labeled A. Conversely the segment labelled B has the same number of ions entering at a relatively small range of sheath extent.

2.3 Monte Carlo Method

A large number of particle trajectories are followed in a Monte Carlo simulation. This provides a statistically robust representation of how the process would progress in reality.

Starting conditions for an ion are randomly selected. The ion speed is selected from a one-dimensional Gaussian distribution and the sheath phase from a linear distribution. Using the equation of motion (2.10) and the Child law equation (2.1) the motion of an ion to the next time point can be calculated. As the simulation progresses information on the position and speed of an ion is updated.

Several pieces of information are collected from each trajectory, initial energy E_0 , initial phase θ_0 , impact energy E_i and time of impact t_i .

The simplest way to analyse a simulation is to plot a histogram of E_i (figure 2.3). This is the most important result and yields the ion energy distribution function (IEDF or simply IED).

2.3.1 Further Results

It has been stated that the number of sheath interactions during the transit of an ion across the sheath region controls the range of final energies that is obtained. Also, there are a number of factors that affect the number of sheath interactions, driving frequency ω_0 , sheath width l_0 , initial ion velocity v_0 . These are related as follows

$$\eta = \frac{l_0 \omega_0}{v_0}. \quad (2.11)$$

In order to investigate parameter space it is only necessary to vary the overall value of η .

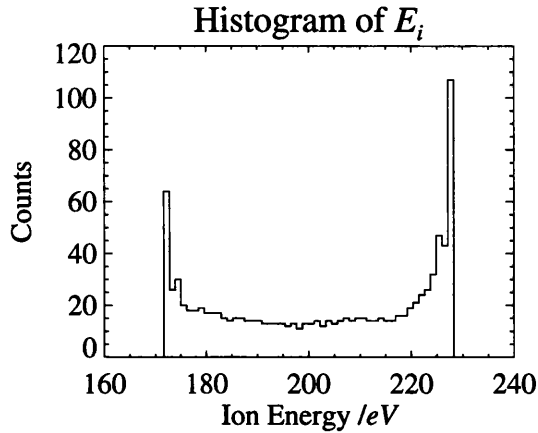


Figure 2.3: IED of Argon in reactor at 13.56MHz.

Results are presented for three regions of η . The relationships between initial energy E_0 , final (impact) energy E_i , initial phase θ_0 and the number of sheath cycles encountered are described. The first series of plots contain six plots for each of the conditions $\eta \ll 1$ (figure 2.4), $\eta = 1$ (figure 2.5) and $\eta \gg 1$ (figure 2.6). The plots show the following information:

1. Initial energy distribution of the ions.
2. IED (histogram of final ion energies).
3. Number of cycles of the oscillating sheath encountered before impact with the substrate.
4. Energy gain, E_i/E_0 versus initial ion energy.
5. Final ion energy versus initial ion energy.
6. Number of cycles encountered versus initial ion energy.

Looking at these plots enables the identification of several trends as η is varied. Looking at each plot in turn the findings are described:

1. The most important of these is the variation in the shape and energy range of the IED's. The IED's can be characterised as follows:

$\eta \ll 1$ broad IED with single peak at even higher energy.

$\eta = 1$ wider IED, one dominant peak at higher energy.

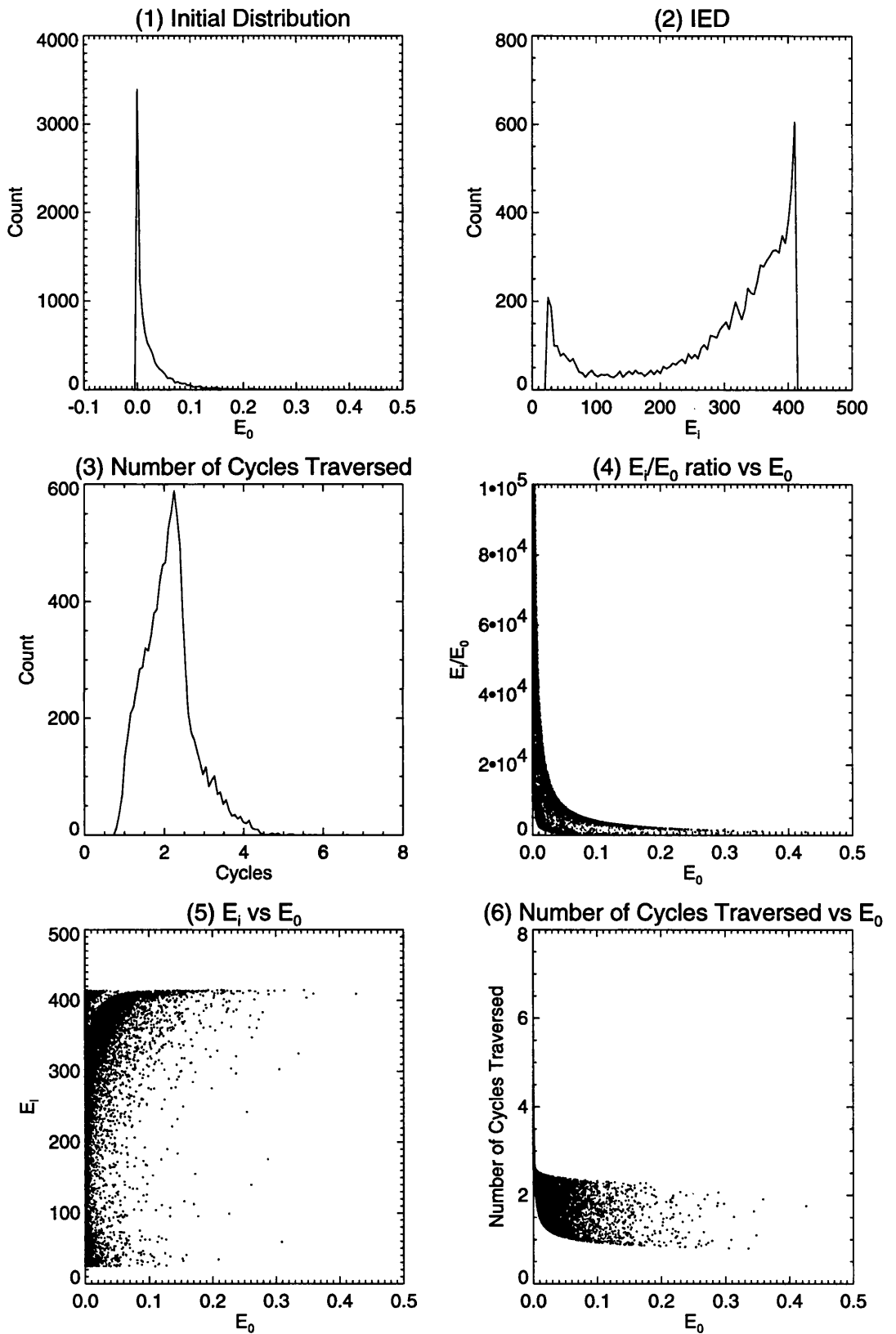


Figure 2.4: Ion energy characteristics when $\eta \ll 1$. Sheath modelled by using Child-Langmuir representation. IED is bimodal with a large high energy peak and a small low energy peak.

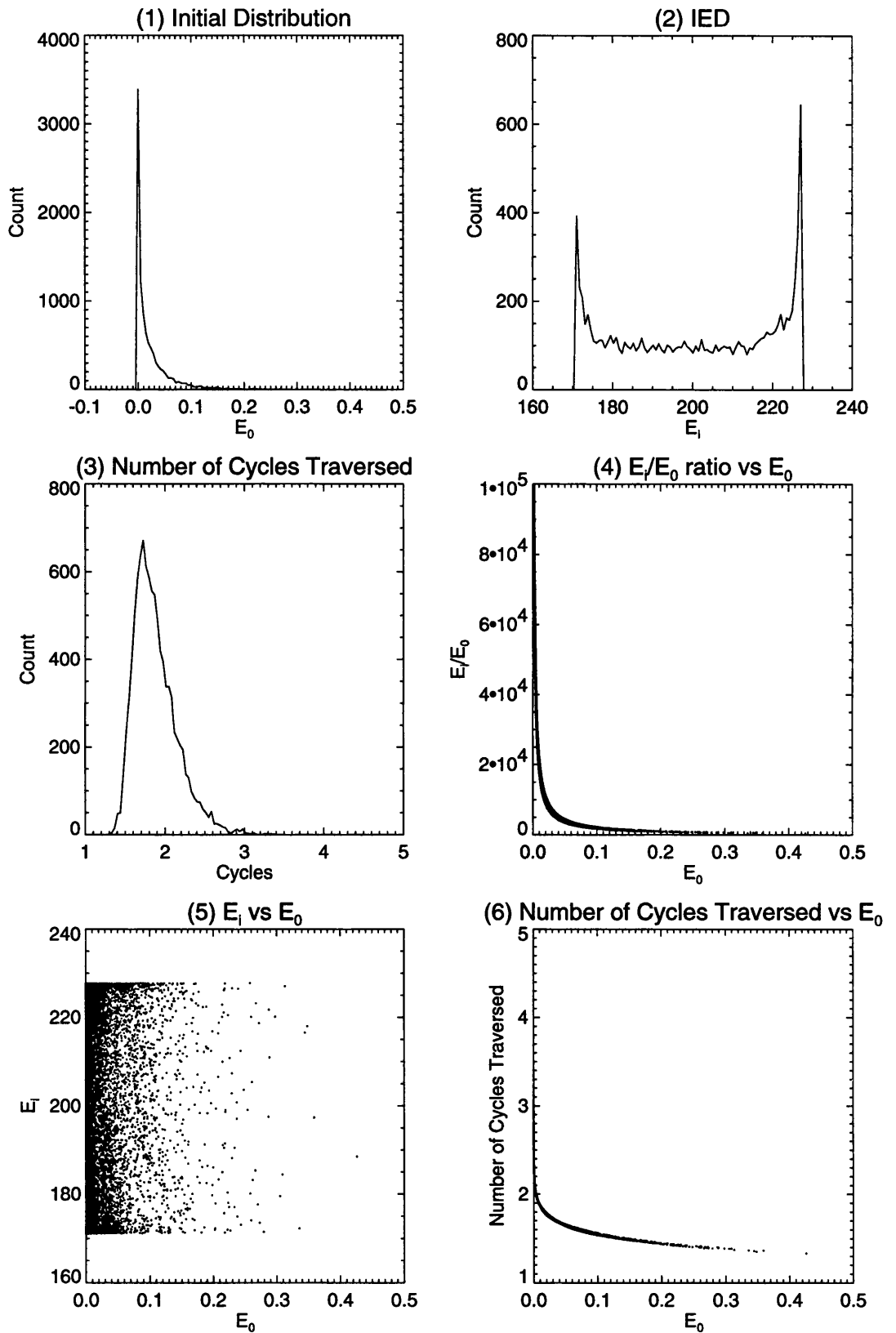


Figure 2.5: Ion energy characteristics when $\eta = 1$. Sheath modelled by using Child-Langmuir representation. IED is bimodal with a large high energy peak and a medium low energy peak, the energy range is smaller than in the previous case.

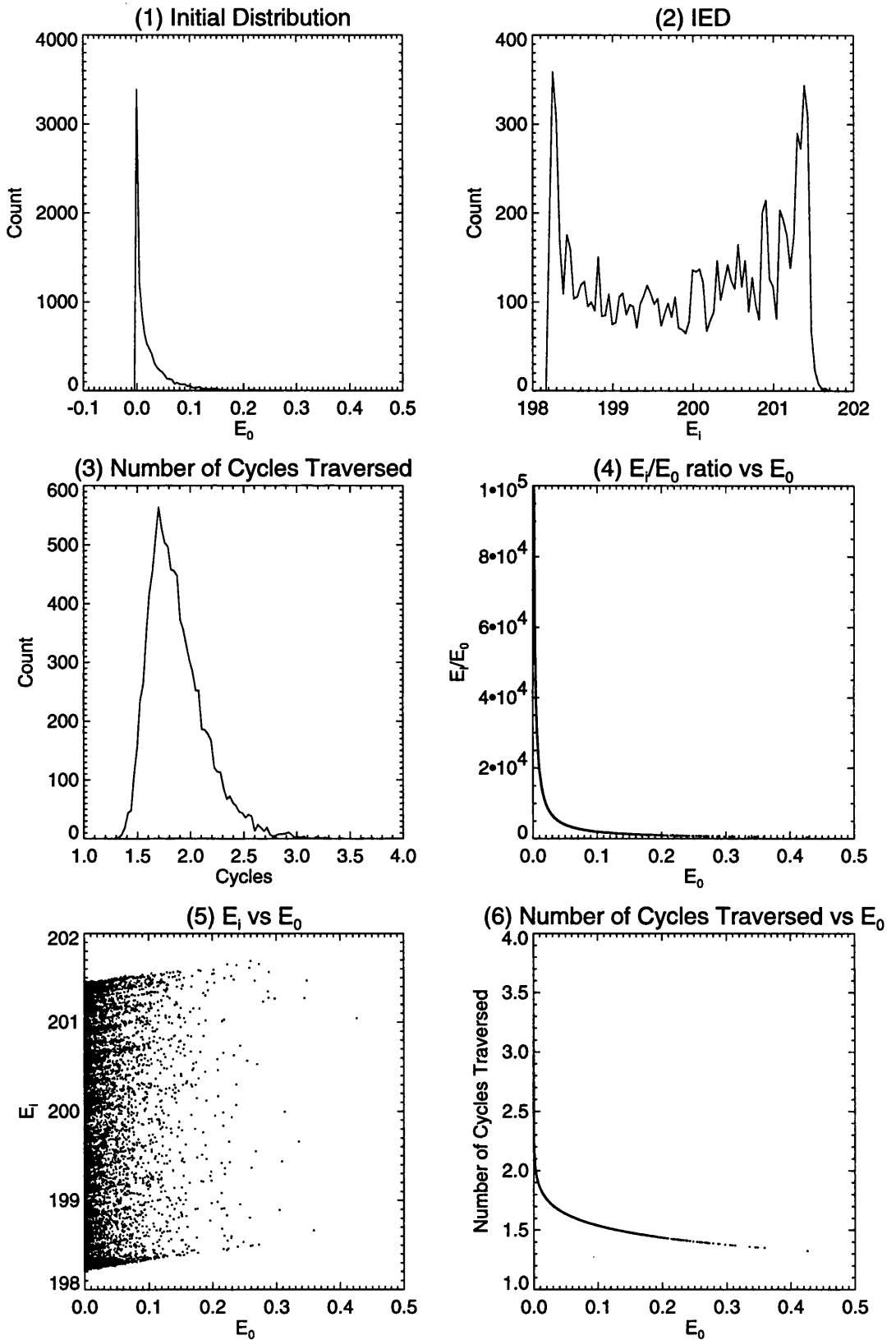


Figure 2.6: Ion energy characteristics when $\eta \gg 1$. Sheath modelled by using Child-Langmuir representation. IED is bimodal with equal high and low energy peaks, the energy range is very small.

$\eta \gg 1$ narrow IED with symmetric peaks.

2. The number of cycles traversed approximately increases by an order of magnitude in each case:

$\eta \ll 1$ centred about 2 cycles, varies from twice this to less than 1.

$\eta = 1$ centered about 18, varies from 13 to 30.

$\eta \gg 1$ centered about 175, varies from 130 to 330 cycles.

3. E_0 distribution same in each case, 1-D Gaussian.
4. Energy gain versus E_0 follows a similar shape in each case, ions starting with low energy have the highest gain, emphasising the point that an ion starting out with low energy can still attain a high energy state. It can be seen in the $\eta \ll 1$ case that for a particular initial energy a wider range of gain is available than in the other two cases.
5. E_i versus E_0 displays how the final energy is largely independent of initial energy. In the case that $\eta \gg 1$ an upward trend in E_i with increasing E_0 is visible, reflecting a dependence on E_0 not previously seen.
6. Number of cycles traversed versus E_0 shows how as η increases the number of cycles traversed becomes very closely related to E_0 . Bearing in mind that it was shown in the previous plot that the full range of possible E_i is available, it can be seen that however many cycles are traversed, the full range of E_i remains available.

2.3.2 Polar Contours of Impact Energy

A further series of plots relate phase information about the interaction of the ion with the oscillating sheath region. Figure 2.7 shows the IED in each previously identified η regime and also a corresponding plot giving information about the phase of the ion. The phase at the point that an ion first encounters the accelerating influence of the oscillating sheath is used as the angular ordinate and initial energy (E_0) as the radial ordinate in a polar contour plot of ion impact energy (E_i).

The information in the polar contour plots of figure 2.7 needs to be carefully interpreted. No indication is given of the number density of points across the plot, the plotting routine merely interpolates between the available data. The plots are most

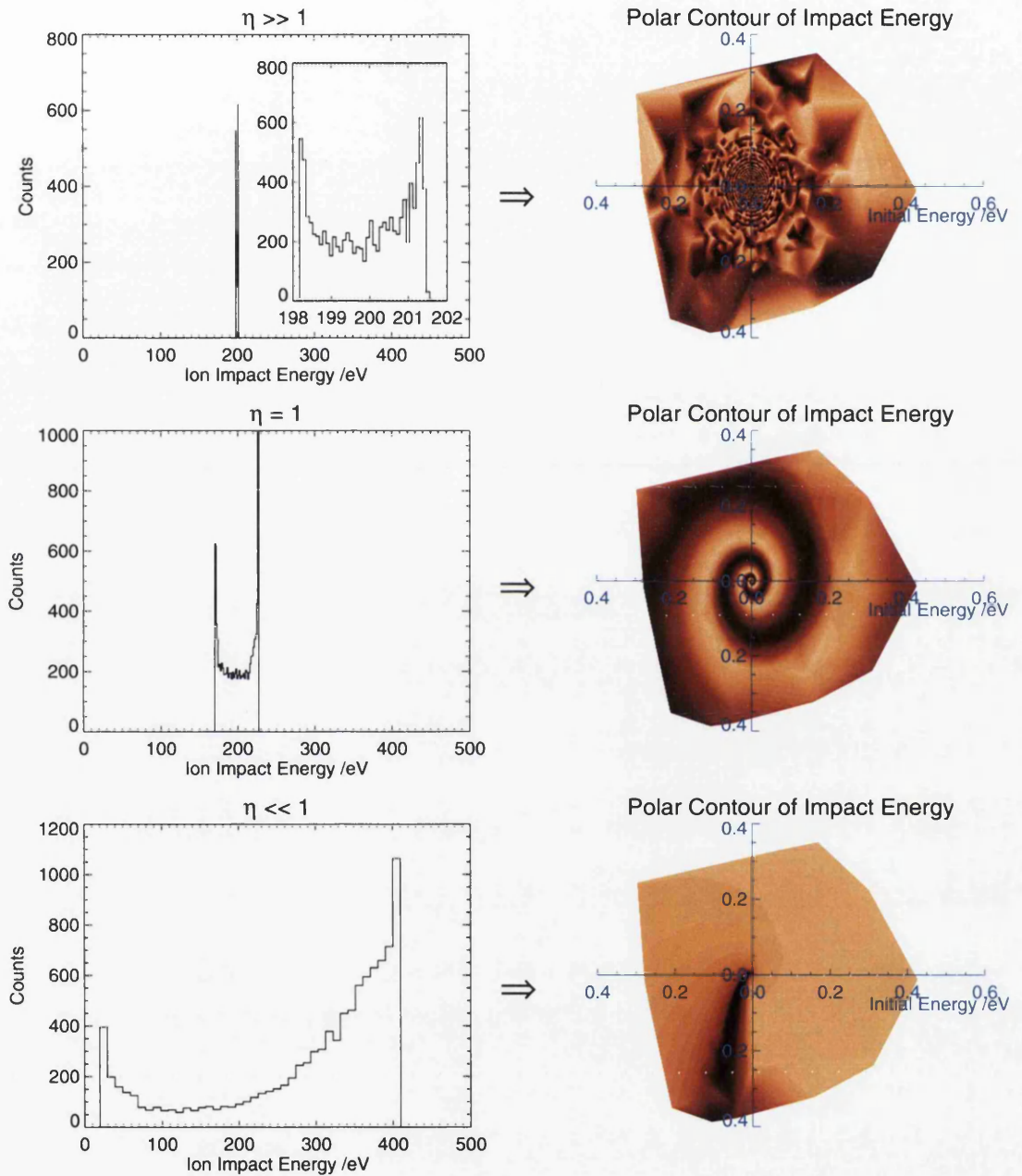


Figure 2.7: IEDs and final energy versus initial energy and phase for three values of η . For colour maps please refer to figures 2.9-2.11. When $\eta \ll 1$ no phase relation is apparent. For $\eta = 1$ phase has a strong relationship with the other parameters. In the case $\eta \gg 1$ phase dominates the resulting final energy.

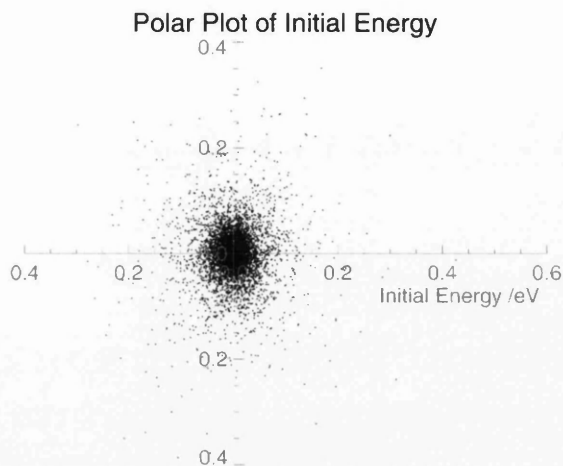


Figure 2.8: Distribution of data points in figure 2.7, showing high coverage in the central region. This yields a well defined centre, with resolution decreasing outwards.

defined in the central region because the one-dimensional Gaussian distribution from which the particles are drawn yields the majority of particles at lower energies. For the same reason, there is a smaller contribution to the energy distribution from ions at greater radial positions. The positions of the points used to create these plots are shown in figure 2.8.

For the case of Medium η a spiral shape can clearly be distinguished. Reducing η yields a looser spiral and increasing η produces a tighter spiral. It is shown in the next section how a clearer plot of this phase relationship can be obtained. Suffice to say, from these results it is clear that any initial energy can result in any final energy, if the appropriate phase is chosen.

2.4 Phase Dependence

All of the above work looks at single trajectories or many trajectories with random starting conditions. In order to gain a deeper understanding of ion impact energies, a systematic record of initial conditions has been undertaken. By setting ions of the same energy off at small and equal steps across all phase and then repeating this for many initial energies a picture of impact energy versus initial phase and energy can be constructed. This has been carried out using the same parameters as have been used in the Monte Carlo simulation, to allow a direct comparison. Low, medium and high η

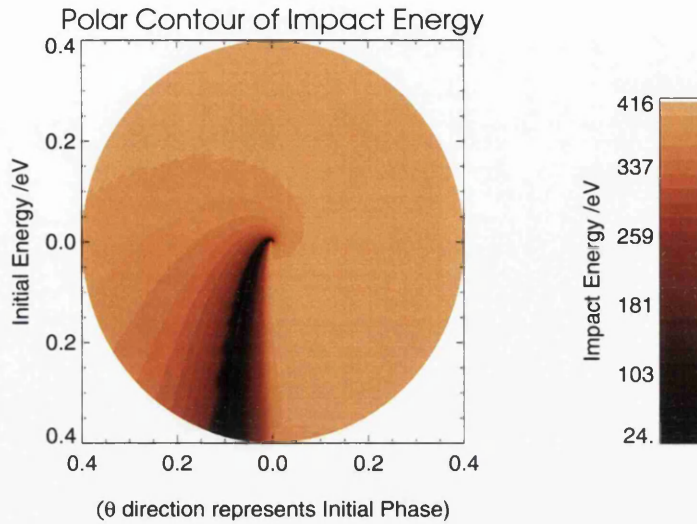


Figure 2.9: Systematically obtained ion energy with same parameters as figure 2.7, $\eta \ll 1$.

are shown in figures 2.9, 2.10 and 2.11 respectively. Note that this provides an evenly spaced grid, unlike the Monte Carlo results in figure 2.7, which accounts for the clearer picture.

There are a few main points to notice about this result:

1. Contours of constant final ion energy follow a spiral shape.
2. The full range of final ion energies is available to ions with any initial phase or energy.
3. A final energy is recorded for a range of starting conditions, which may or may not be appropriate to any specific processing system.

Point (1) is significant because a spiral shape is very easy to describe mathematically and as shown later can lead to an analytic description of ion energy characteristics.

The second point highlights the non-obvious behaviour of the acceleration mechanism that acts upon an ion in an oscillating sheath. There is no indication of the change in final ion energy given by a known change in the initial energy of an incoming ion. The dependence on phase has to be taken into account at the same time.

The appropriateness mentioned in point (3) addresses the need to select data which reflects the actual initial conditions at the sheath edge. For instance one might consider

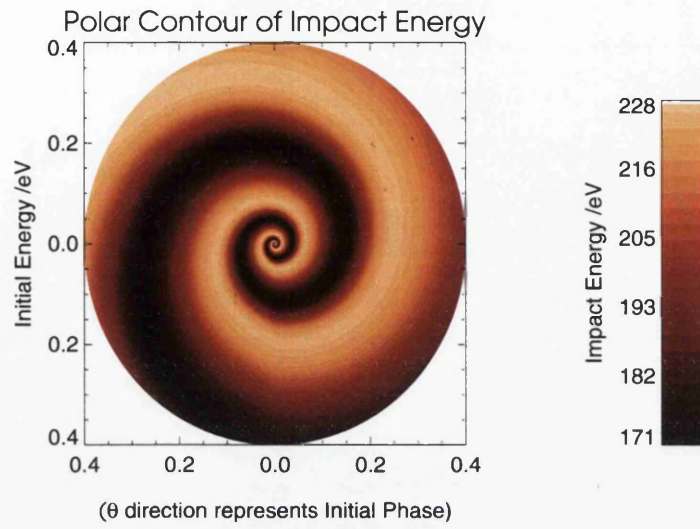


Figure 2.10: Systematically obtained ion energy with same parameters as 2.7, $\eta = 1$.

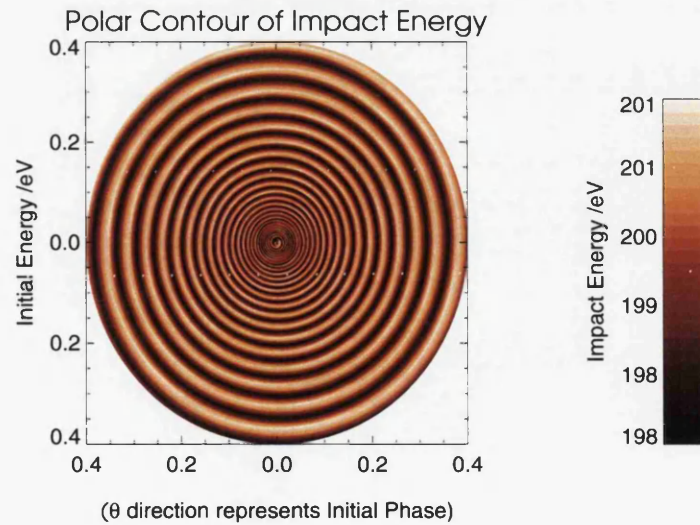


Figure 2.11: Systematically obtained ion energy with same parameters as 2.7, $\eta \gg 1$.

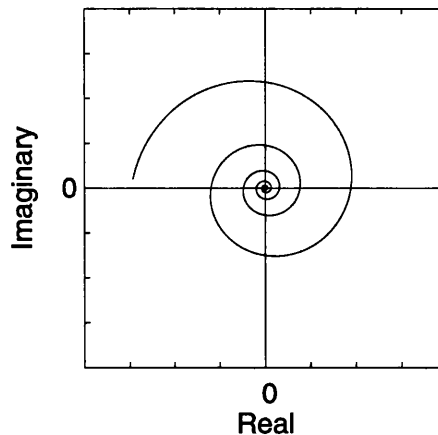


Figure 2.12: Example spiral plot.

a Bohm speed appropriate, so only consider a concentric circle of data to reflect the final ion energies.

Consider this scenario: Due to some mechanism, ions are biased toward entering the sheath region only at a certain range of phase. Now the ions will impact with an altered distribution of final energies.

If energy and phase *distributions* are involved then the interpretation of figures 2.9–2.11 becomes difficult to comprehend.

2.5 Spiral Description

Given that numerical simulation of ions accelerating in an oscillating sheath has produced the result in the previous section, an analytic approach to generating IED's has been undertaken. This works backwards from the premise that ion impact energies form a spiral shape when plotted versus initial energy and phase.

A spiral is essentially a sinusoidal shape with an amplitude that increases with time, plotted in polar coordinates. This is most clearly written in exponential terms:

$$z = Ae^{(\lambda+i\omega)t}, \quad (2.12)$$

where A and λ are scaling factors. In equation (2.12), the spiral is growing exponentially since the λt term is in the exponential. This is plotted in figure (2.12):

If we take $|z|$ as the argument of a periodic function

$$Q = \cos(\pi \log |z|) \quad (2.13)$$

this gives the intensity Q , which when plotted can replicate the numerical result shown in figures 2.9–2.11.

2.5.1 Implementation

In order to produce this computationally the following method has been used.

1. Generate an $n \times n$ array with values increasing on concentric circles from the centre in the range $[0..1]$ (figure 2.13a). Call this array A
2. Similarly, let array B have values that increase radially, in the range $[0..2\pi]$ (figure 2.13b).
3. The sum of these arrays is an array which has values increasing by 2π around concentric circles and the absolute value increases radially outwards. The radial dimension increases exponentially, so the required operation actually is $C = \log(A) + B$.
4. To create the polar plot of initial energy and phase versus final energy, take the cosine of C (figure 2.13c).

$$D = \cos(\log A + B) \quad (2.14)$$

In order to generate an IED, it is necessary to add some information about the initial conditions. The energy distribution needs to be addressed, since there are not an equal number of particles at all energies. To represent this graphically, it is necessary to add the extra dimension of number density to the plot. This is achieved by changing the final energy representation to a colour depth and introducing the number density as an intensity. As a starting point, a linear distribution can be defined (figure 2.13d).

Generation of a IED is now a case of producing a histogram of the number of particles at each intensity, biased by the number density (figure 2.14).

2.5.2 Variation with Sheath Parameters

Looking back to figure (2.7) it can be seen how the results of a Monte Carlo numerical simulation vary with the η parameter. Bearing in mind that only the central part of the

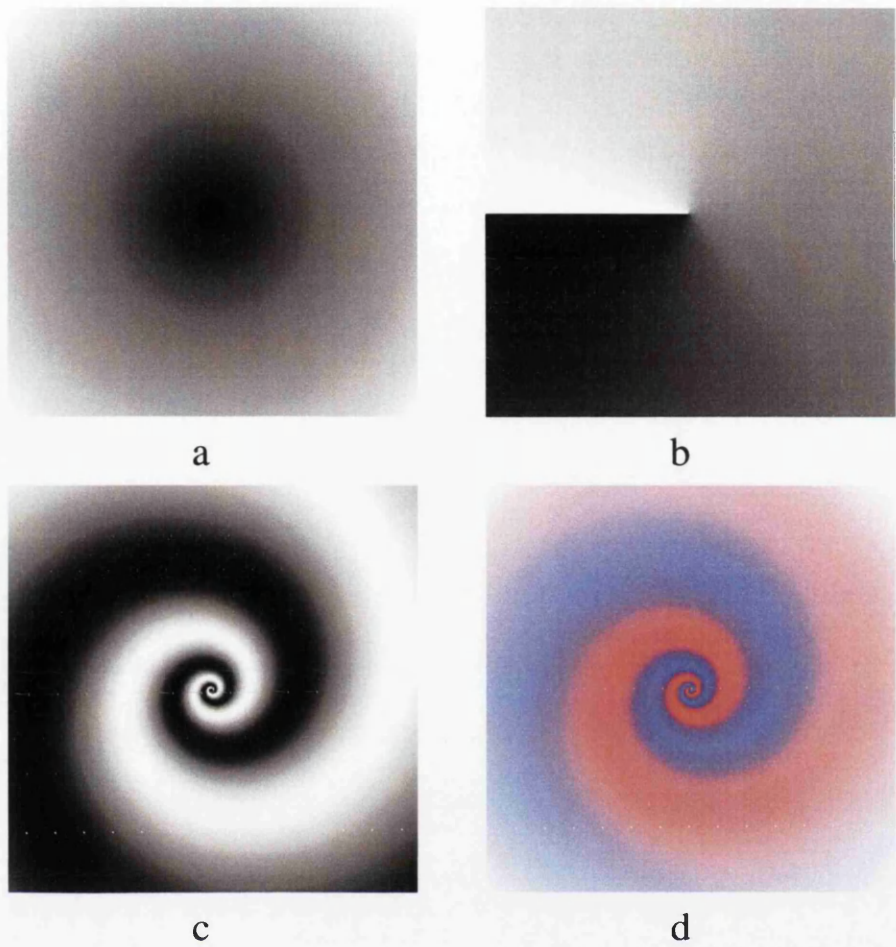


Figure 2.13: Development of the analytic spiral.

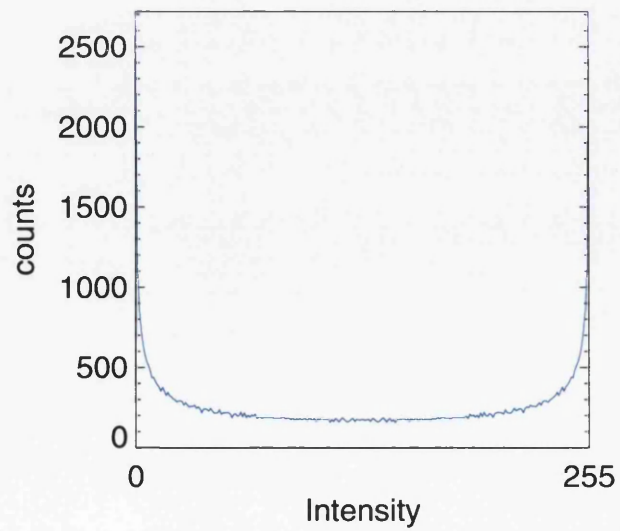


Figure 2.14: Extracted IED, the symmetry is discussed in section 2.5.3.

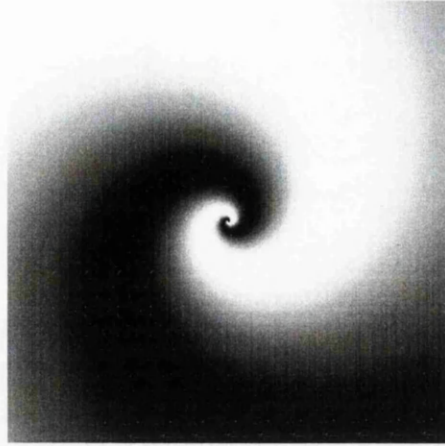


Figure 2.15: Analytic spiral when $n = 2$. Characterised by open shape.



Figure 2.16: Analytic spiral when $n = 5$. Several turns of the spiral are made.

contour is well defined, medium η completes two or three spirals in the energy range examined. Moving to high η results in a tighter spiral, such that there are effectively a series of concentric circles. At low η , not even one spiral is completed and the final energy mainly sits near one higher energy.

So in order to incorporate variations of η into this representation, the tightness of the spiral must be adjusted accordingly. This is accomplished by a slight modification to (2.14)

$$D = \cos(n \log A + B) \quad (2.15)$$

where n controls the tightness of the spiral. Figures 2.15, 2.16 and 2.17 show this.

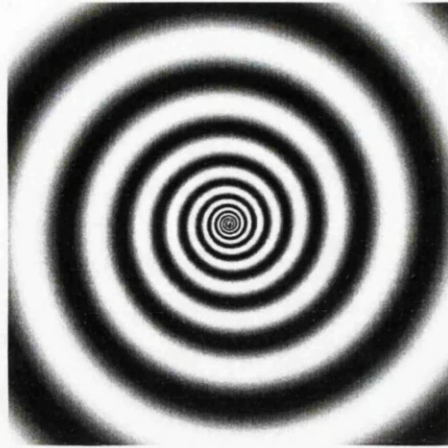


Figure 2.17: Analytic spiral when $n = 5$. Spiral approaches a series of concentric circles.

2.5.3 Spiral Function Shape

The cosine used in the formulation of the spiral is a symmetrical function. This means that the spiral is rotationally symmetrical and the histogram that results from using all the data in figure 2.14 is also symmetrical.

Particularly looking at the low value of η in figure 2.7, the need to define an appropriate function around the spiral is apparent. Most of the spiral occupies a high energy level so a sinusoidal function does not satisfactorily describe the shape of the contour. This can be implemented by a generalisation in (2.15) by using an alternative function to the cosine.

A function that moves slowly from maximum to minimum and spends more time at the maximum than the minimum will produce an asymmetric bimodal distribution similar to that seen in figure 2.5.

2.5.4 Selection of Initial Phase

In section 2.4 it was stated that if ions were only entering the sheath region at a particular range of phase, then this would have an effect on the ion energy distribution. This can be investigated by making a histogram from a selected region of phase in the spiral function. This can be thought of as taking a wedge from the spiral.

The result of this is shown in figure 2.18 for different values of n . Firstly only consider the solid blue line and compare with that in figure 2.14 (all the data).

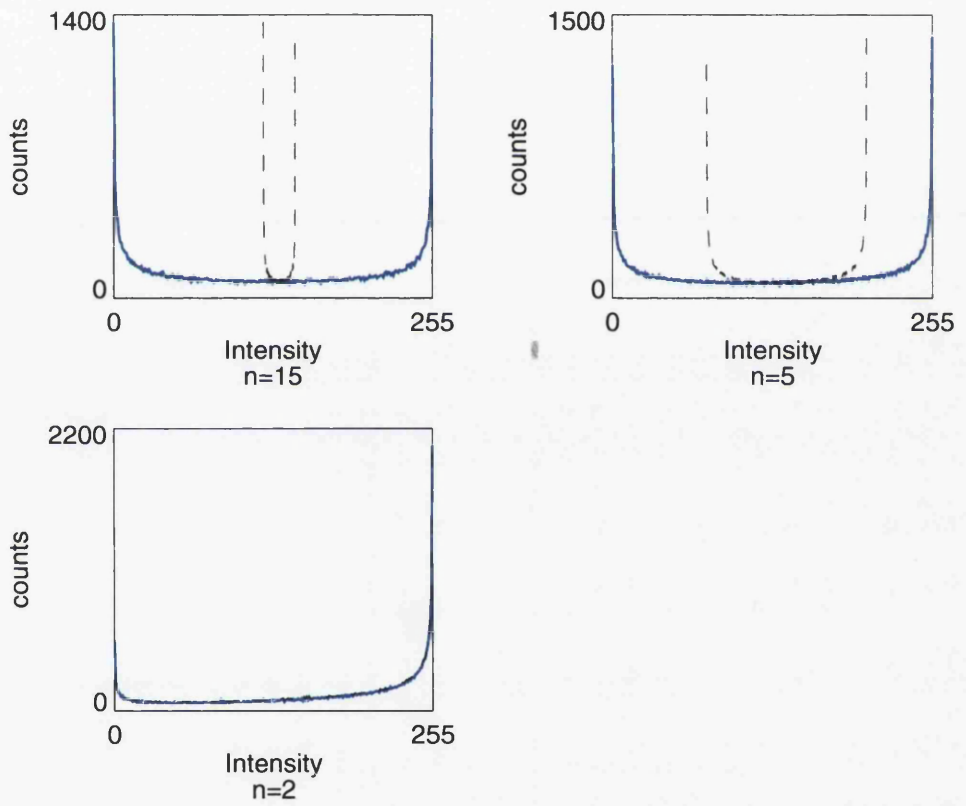


Figure 2.18: IED's at different values of n , with a reduced phase acceptance angle. The dashed line is an indication of the narrowing of ion energies with increasing η .

n=15 A selected region of phase from figure 2.17. Many cycles of the spiral are made and the result is similar to the full data set.

n=5 A selected region of phase from figure 2.16. Now it is possible to select a region of phase that results in a bimodal distribution, with a larger high energy peak.

n=2 A selected region of phase from figure 2.15. A more extreme high energy peak is produced.

In these spiral plots intensity represents ion energy, but does not give a direct measure of the ion energy. The dashed line is the same as the solid blue line, but has been scaled to indicate the effect of increasing η . That is, a narrowing of the energy range. To obtain absolute rather than relative values for ion energy, an attempt to characterise a particular processing system must be made.

Chapter 3

Ion Dynamics II

3.1 Motivation

Work in the previous chapter was based on the Child-Langmuir equation for space charge limited current. The formulation of this equation requires that only one charge carrier is considered, so that the energy conservation equation can be used. This means that electrons are not considered when evaluating the electric field across the sheath region. It can be argued that this is a reasonable approximation since any electron influence is only at the very edge of the sheath-plasma interface.

Reflecting on the last chapter, it has been shown that the initial conditions as an ion enters the sheath region have a coherent relationship with the final impact energy. If the conditions at the sheath interface are modified, then this may propagate an appreciable effect to the ion energy distribution at the substrate surface.

Given the effect of adjusting the initial conditions it is also interesting to consider variations in initial conditions along a spatial dimension parallel to the substrate. Do spatial variations lead to nonuniform energy distributions?

3.2 Full Non-Linear Solution

Recall that the full non-linear sheath equation is

$$\chi'' = \left(1 - \frac{2\chi}{\mathcal{M}^2}\right)^{-1/2} - e^{-\chi}, \quad (3.1)$$

where

$$\chi = -\frac{e\phi}{k_B T_e} \quad \mathcal{L} = \frac{x}{\lambda_D} = x \left(\frac{n_0 e^2}{\epsilon_0 k_B T_e}\right)^{1/2} \quad \mathcal{M} = \frac{u_0}{(k_B T_e / m_i)^{1/2}} \quad (3.2)$$

and the prime denotes $d/d\mathcal{L}$.

Instead of approximating the sheath description a numerical routine has been employed to solve the full non-linear sheath equation (3.1).

The first integration of (3.1) is possible by multiplying by $d\chi/d\mathcal{L}$ and integrating over \mathcal{L}

$$\int^{\mathcal{L}} \frac{d\chi}{d\mathcal{L}} \frac{d}{d\mathcal{L}} \left(\frac{d\chi}{d\mathcal{L}}\right) d\mathcal{L} = \int^{\mathcal{L}} \frac{d\chi}{d\mathcal{L}} \left[\left(1 - \frac{2\chi}{\mathcal{M}^2}\right)^{-1/2} - e^{-\chi} \right] d\mathcal{L} \quad (3.3)$$

Obtaining

$$\left(\frac{d\chi}{d\mathcal{L}}\right)^2 = f(\chi). \quad (3.4)$$

where

$$f(\chi) = 4\mathcal{M}^2 \left[\left(1 + \frac{2\chi}{\mathcal{M}^2} \right)^{1/2} - 1 \right] + 2(e^{-\chi} - 1) \quad (3.5)$$

This can be integrated numerically using a standard Romberg integration routine supplied from the Numerical Recipes library[34]. Some rearrangement is required first:

$$\frac{d\chi}{d\mathcal{L}} = \sqrt{f(\chi)} \quad (3.6)$$

$$\frac{d\mathcal{L}}{d\chi} = \frac{1}{\sqrt{f(\chi)}} \quad (3.7)$$

$$\int \frac{d\mathcal{L}}{d\chi} d\chi = \int \frac{d\chi}{\sqrt{f(\chi)}} \quad (3.8)$$

$$\mathcal{L} = \int_{\chi}^{\chi_w} \frac{1}{\sqrt{f(\chi)}} d\chi \quad (3.9)$$

where χ_w is the potential at the electrode. This allows the calculation of the distance ordinate \mathcal{L} , by the numerical integration of the potential ordinate χ .

In order to provide a non-oscillatory solution to this equation, the Bohm criterion must be satisfied.

$$\mathcal{M}^2 > 1 \quad (3.10)$$

$$u_0^2 > \frac{k_B T_e}{m_i} \quad (3.11)$$

Some thought has to be given to the topology of this representation, to be clear on firstly the position of the wall and sheath edge and secondly the direction of ion motion and potential gradient. These matters are quite trivial, except for the location of the sheath edge.

3.3 Sheath Extent

In a plasma with no externally applied potential, sheath formation is determined by the thermal motion of the ions and electrons. The Debye length describes the sheath region under these conditions. When an external potential is applied this causes an extension of the sheath region. This situation is described by (3.1) and simplified in the Child-Langmuir approximation.

Under the Child-Langmuir Law, the sheath edge was clearly prescribed by artificial means. Observations and measurements provide reasonable estimates of the sheath

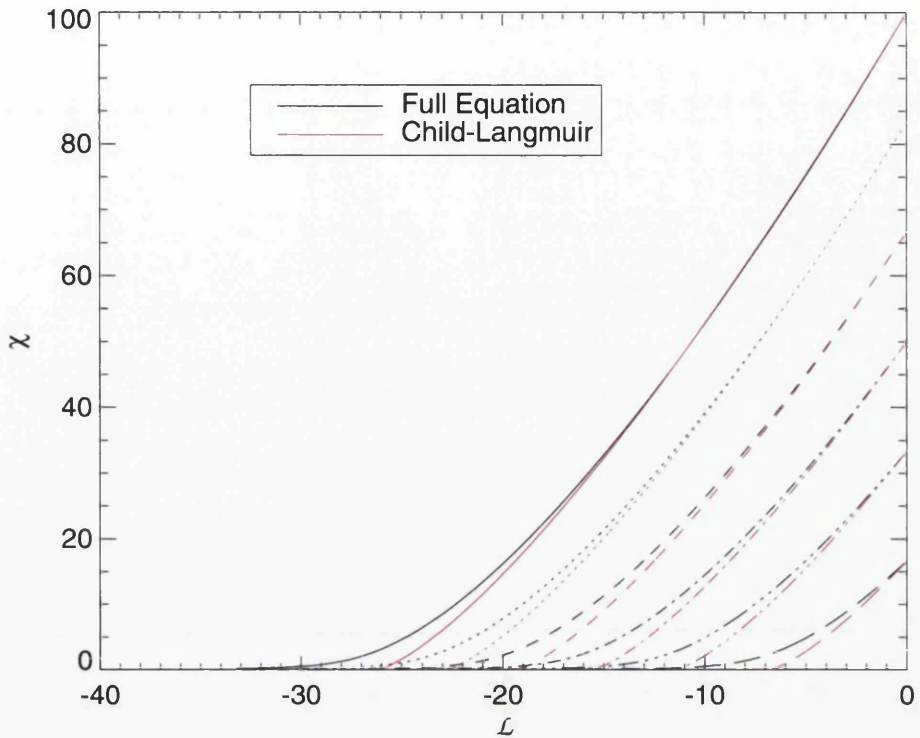


Figure 3.1: Sheath extent at a range of wall potentials for two sheath representations (χ ordinate is potential, \mathcal{L} ordinate is distance). The Child-Langmuir sheath edge ($\chi = 0$) occurs at a defined point, whereas the full equation produces a solution asymptotic with $\chi = 0$.

thickness that can be fed into the Child-Langmuir Law as a parameter. When solving the full equation the sheath edge is not well defined as the sheath potential asymptotically approaches the plasma potential. Consequently the sheath extends on a length scale one or two orders of magnitude greater than the Child-Langmuir thickness.

Consider that the full sheath equation is valid for all space (in a collisionless plasma), but the Child-Langmuir Law is only valid where no electrons are present, ie. away from the sheath edge. It follows then that the two descriptions will match at the vessel wall where the electrons are completely expelled. The gradient of both representations can be matched at the wall to show how the Child-Langmuir Law deviates from the full equation. This comparison is made in figure 3.1. The Child-Langmuir sheath terminates at a distinct distance in the \mathcal{L} dimension. This contrasts with the full equation which asymptotically approaches $\chi = 0$ as \mathcal{L} becomes progressively more negative.

3.4 Numerical Model

A different approach is taken to model the system made using the full equation. Because there is no longer a simple analytic solution to the sheath equation, a relatively intensive computation is required to perform the integration. To obtain IED's many particle simulations are required and if an integration were performed at each step, the time to complete the simulation would become large. To alleviate this problem, the sheath equation can be evaluated for all necessary values of potential and then stored in an array to be used in the simulations. This array only needs to be updated if a change in the resolution or a fundamental parameter is required.

In order to search the array quickly a bisection approach has been adopted, providing an exponential speed increase when compared to a linear search method. This means that doubling the resolution of the array only requires one more iteration of the search loop. A bisection algorithm can only be applied to an array where the values are monotonic. The target value is compared with the central value of the array, if this is higher than the target then the higher half of the array is discarded, or vice versa. The remaining array is processed in the same way and again until a single value is arrived at.

Once the above issues have been addressed, individual ion trajectories can be followed from when an ion enters the sheath region until it impacts upon the electrode. Many trajectories are followed in a Monte Carlo simulation to build up an Ion Energy Distribution.

3.4.1 Program Description

- Array of potential on wall as a function of phase created. Equation 2.3 and associated equations are implemented for this purpose.
- The Romberg integration routine mentioned previously is used to solve equation 3.9. The wall potential χ_w is set at the maximum value found in the above calculation of wall potential, the choice of χ decides to what distance from the substrate is being considered. For the purposes of this simulation, this point is where the field is judged to be reduced to such a small level that the effect it has is negligible.

- These two results are used to produce an array which gives the maximum sheath extent at each point in phase. This can be used in the main program to determine if a calculation has to be made involving the sheath, or if the ion should continue at the same speed.
- There are three possible ways the program can now progress depending upon whether a trajectory, IED or systematic study is to be obtained. These options determine how initial conditions are chosen and what information is recorded.

Trajectory Initial conditions chosen once. Record of sheath extent, ion position and sheath phase at each point in phase. One ion followed.

IED Initial conditions chosen randomly, from appropriate distribution. Record of initial energy, final energy and number of sheath cycles encountered, phase information may also be recorded. Many ions followed.

Systematic Study Initial conditions selected to cover all phase and initial energy parameters uniformly. Initial phase, initial energy and final energy recorded. Many ions followed.

- Whatever conditions are being used, the main program follows the progress of the ion, updating position and speed at each time step.

3.5 Results

To try to provide a close comparison with the Child-Langmuir sheath results, the same initial conditions as in those experiments were retained for these simulations.

3.5.1 Ion Trajectories

Looking at the trajectory that an ion follows through the sheath region shows up the fundamental effect of considering electrons in the sheath.

Two lines are shown on the trajectory plots. The periodic line shows the furthest extent of the influence of the sheath. Note that the sheath is not 'on' or 'off', but the force acting on the ion is a function of sheath extent and the position of the ion within it. The other line shows the position of the ion as the simulation progresses.

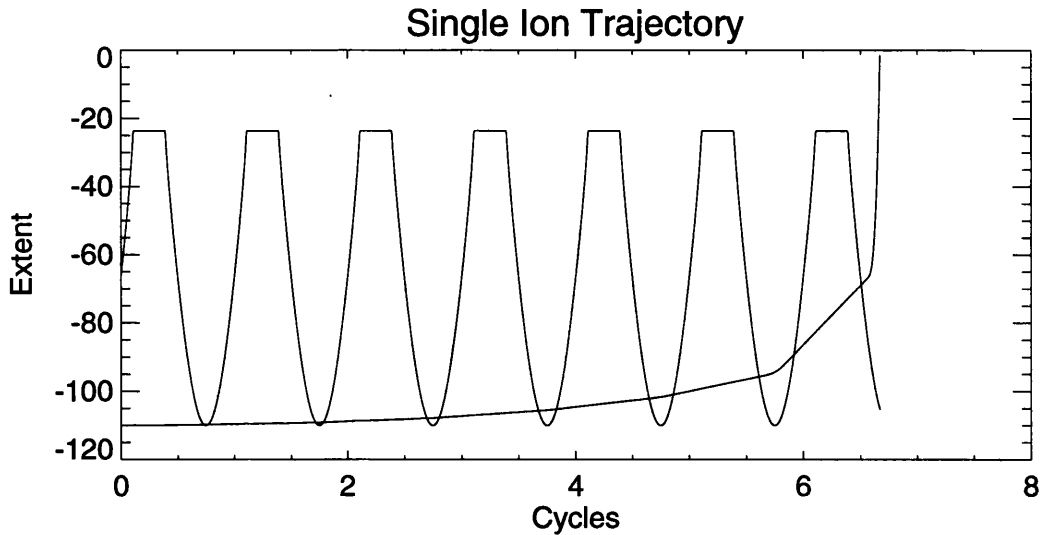


Figure 3.2: Ion trajectory, $\eta \ll 1$. Sheath modelled using numerical solution of the full non-linear sheath equation. Extent = x/λ_D .

Figures 3.2, 3.3 and 3.4 show trajectories when $\eta \ll 1$, $= 1$ and $\gg 1$ respectively. For the first two cases the whole of the simulation is plotted, the last condition causes the ion to traverse so many sheath cycles that only the last portion of the trajectory is shown.

It is apparent in each case that the ion encounters more sheath cycles than in the Child-Langmuir sheath. The electric field strength has been reduced by the addition of electrons at the outer edge of the sheath region. Because of this the force on the ion as it first encounters the oscillating sheath is much smaller than previously. Gradually the ion travels further into the sheath region and the force experienced returns to that of the Child-Langmuir sheath.

3.5.2 Ion Energy Distributions

Although ion trajectories help understand what is happening to an individual ion, the collective behaviour of the ions can be seen by generating ion energy distributions.

Three results are presented. One for each of $\eta \ll 1$ (figure 3.5), $\eta = 1$ (figure 3.6) and $\eta \gg 1$ (figure 3.7).

Six plots are presented for each value of η . Left to right, top to bottom these are as follows.

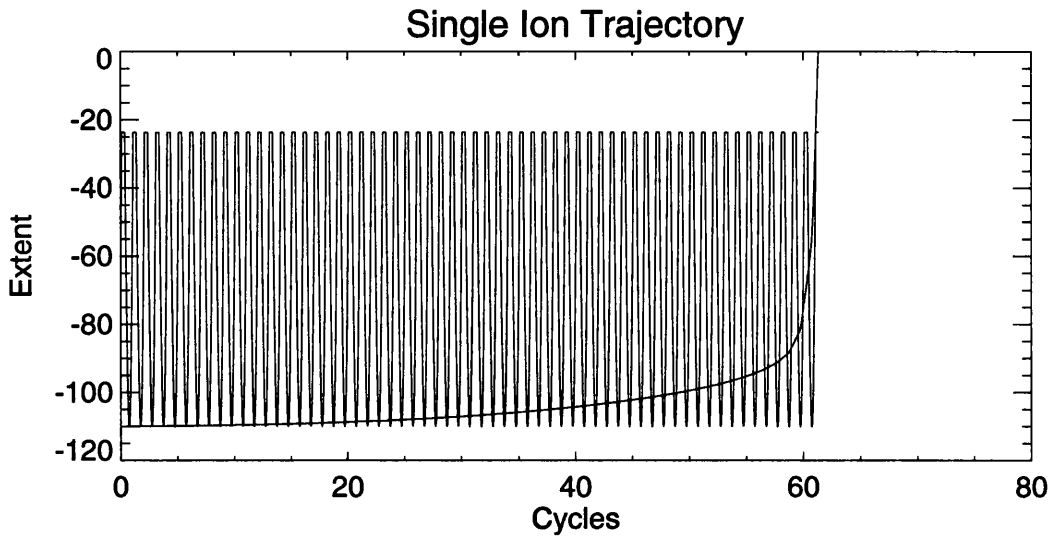


Figure 3.3: Ion trajectory, $\eta = 1$. Sheath modelled using numerical solution of the full non-linear sheath equation. Extent = x/λ_D .

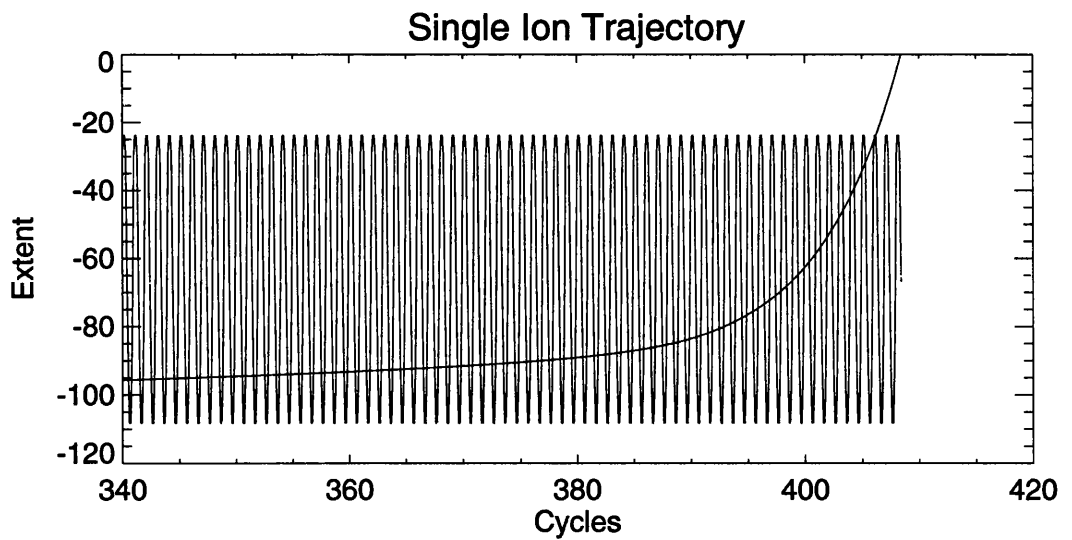


Figure 3.4: Ion trajectory $\eta \gg 1$. Sheath modelled using numerical solution of the full non-linear sheath equation. Extent = x/λ_D .

1. Initial energy distribution of the ions.
2. IED, histogram of final ion energies.
3. Number of cycles of the oscillating sheath encountered before impact with the substrate.
4. Energy gain (E_i/E_0) versus the initial ion energy.
5. Final ion energy versus initial ion energy.
6. Number of cycles encountered versus initial ion energy.

It is interesting to note the similarities and differences in these plots when compared with the results obtained in the case with no electron influence at the sheath edge.

3.5.3 Polar Plots of Parameter Space

To complete the results, phase, initial energy and final energy are recorded in a systematic study. Again results are presented for each of the three cases that has been looked at (figure 3.8, 3.9 and 3.10).

3.6 Discussion

Recall the motivation for improving on the Child-Langmuir sheath approximation. The full non-linear sheath equation has been numerically solved in order to include the influence of electrons. The effect of this is seen near the plasma-sheath boundary, where the electric field is insufficient to completely deplete the region of electrons. Although the overall potential drop is still the same, the sheath influence is considered further into the plasma. A more gentle acceleration is experienced by the ions until the full non-linear and Child-Langmuir sheaths converge.

The modification of the initial acceleration properties of the sheath has a profound effect on the trajectory of an ion. Since the acceleration of the ion when it first enters the region is small, it is not rapidly accelerated into the region of higher electric field. As a consequence, more time is spent in the sheath region and so more sheath cycles are traversed. As was seen in the previous chapter, the number of cycles encountered has a strong impact upon the influence of the initial phase on the resulting IED. In this

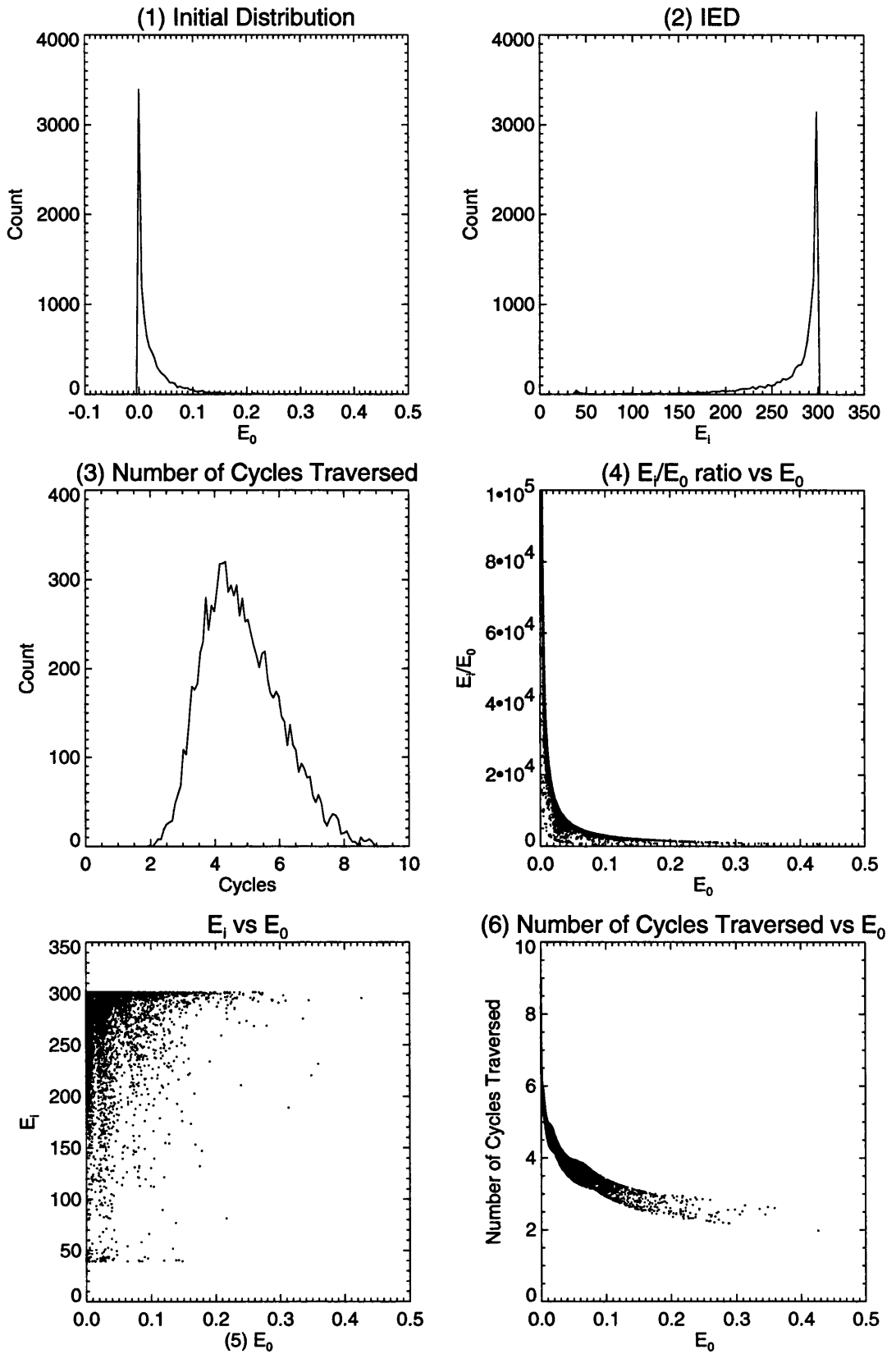


Figure 3.5: Ion energy characteristics when $\eta \ll 1$. Sheath modelled by numerical solution of full non-linear sheath equation. IED has a broad energy distribution and a large high energy peak.

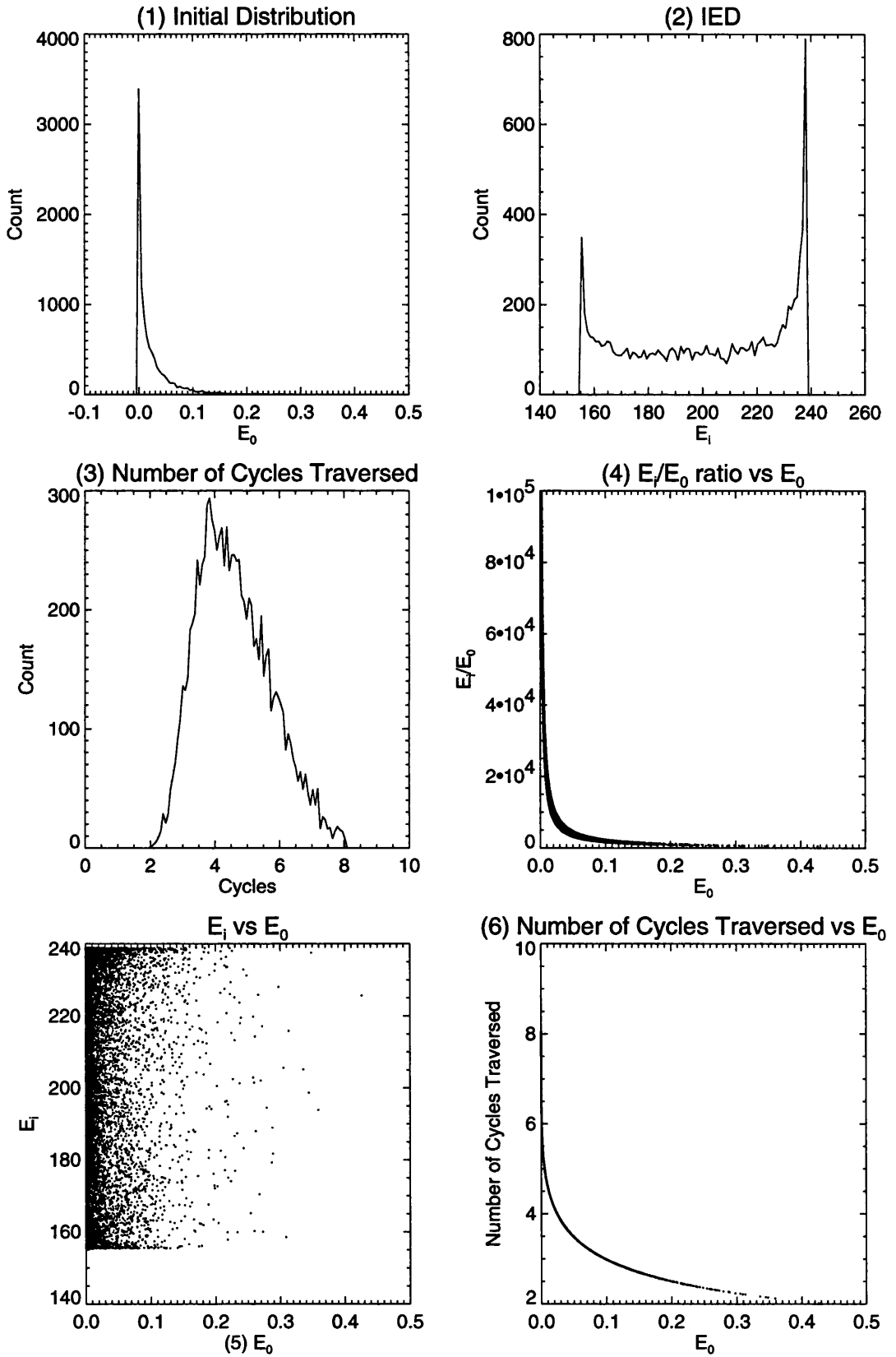


Figure 3.6: Ion energy characteristics when $\eta = 1$. Sheath modelled by numerical solution of full non-linear sheath equation. IED is bimodal, with a larger high energy peak.

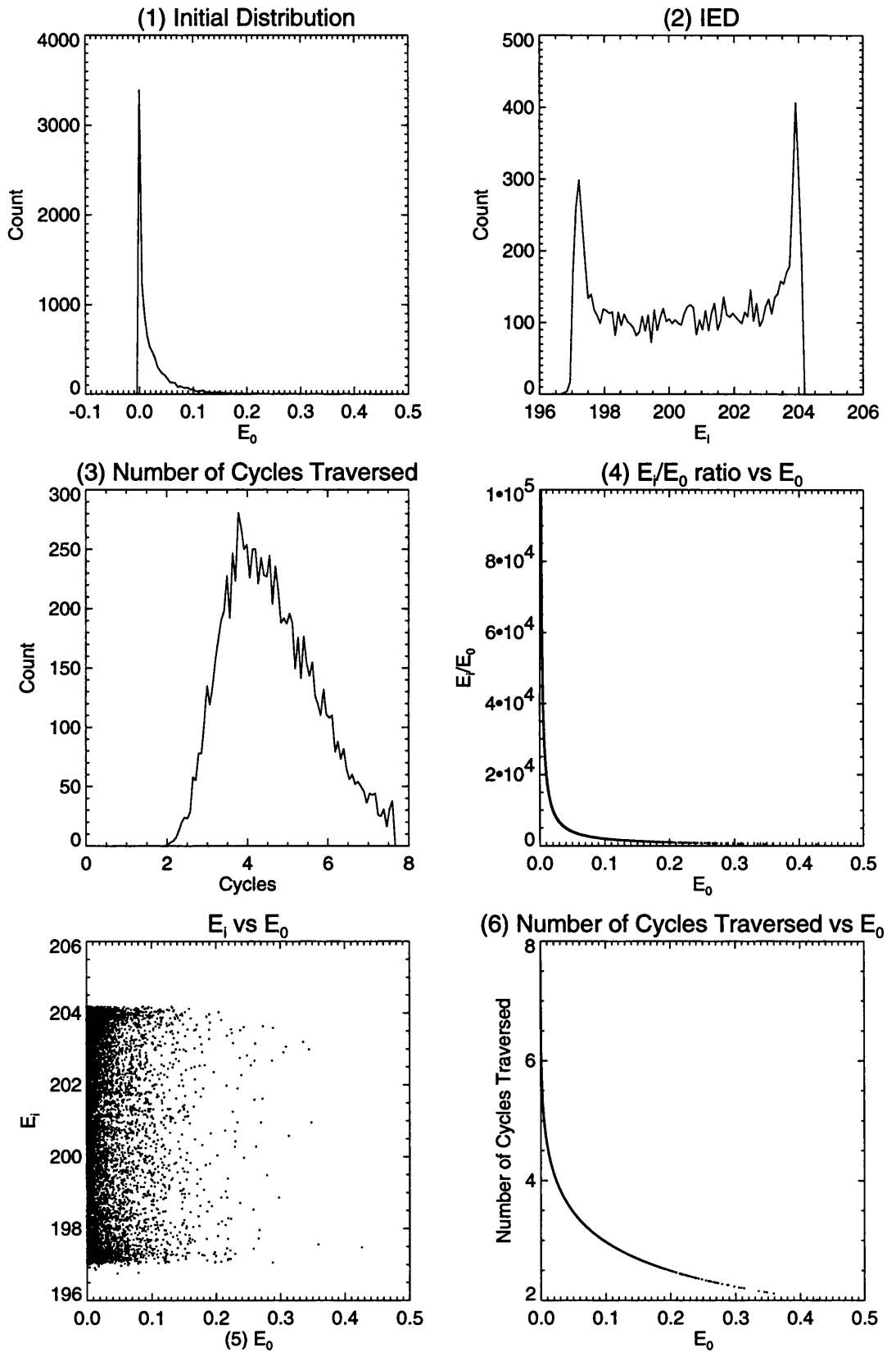


Figure 3.7: Ion energy characteristics when $\eta \gg 1$. Sheath modelled by numerical solution of full non-linear sheath equation. IED has a narrow, bimodal energy distribution with a slightly larger high energy peak.

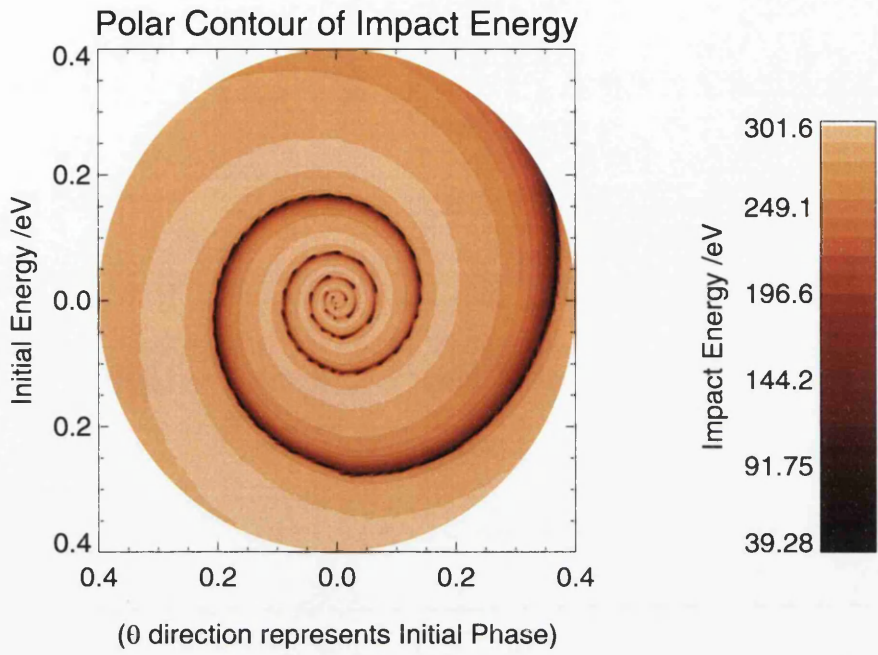


Figure 3.8: Polar plot of ion energy, full sheath equation, $\eta \ll 1$.

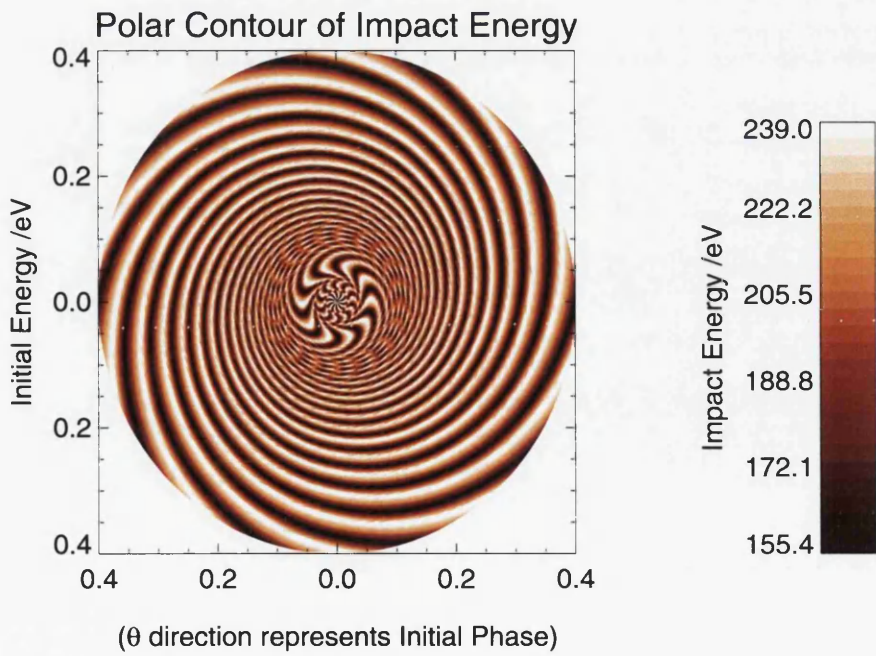


Figure 3.9: Polar plot of ion energy, full sheath equation, $\eta = 1$.

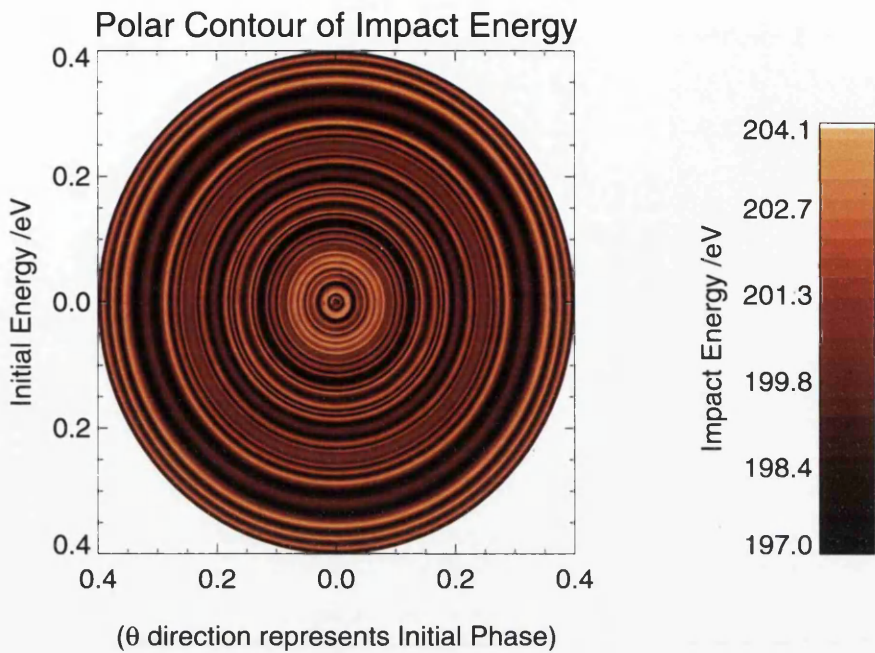


Figure 3.10: Polar plot of ion energy, full sheath equation, $\eta \gg 1$.

simulation the phase distribution of the ions as they enter the electron-free region of the sheath will already have been altered by the sheath cycles that have been encountered in the reduced field that was not previously included.

This leads to a number of differences in the ion energy distribution. Each case is looked at in turn.

In the case that $\eta \ll 1$, the low energy spike previously seen under these conditions has been all but removed. As discussed above, the increased number of sheath encounters has caused the ions to follow a more uniform path to the substrate. This is also reflected in the polar plot, where, while still showing the characteristic spiral shape, the plot is dominated by the high energy ions with only a small region available to a low energy route. The maximum energy that can be attained is reduced. This is related to the distance from the substrate that an ion enters the last sheath cycle prior to impact. For an ion to gain the most energy possible it spends all of its time under the extent of the sheath. During any time not under the sheath extent, the ion is in free fall and does not gain any energy from the sheath. When more sheath cycles are traversed the time an ion spends between sheath cycles (when it is not being accelerated) is more significant. During this period the ion is getting closer to the substrate, but not gaining energy.

The ion will enter the last sheath cycle before impact closer to the substrate, so the final energy gain is lower.

Phase effects are more dominant in the case $\eta = 1$. As in the previous case, a route to low energies is more difficult to come by. The range of available energy has increased, because the modification of initial phase has made a greater variety of trajectories available to each ion.

Lastly for the case $\eta \gg 1$, the large number of sheath encounters produces a narrow band of final energies. A wider range is available than in the Child-Langmuir case, again reflecting the phase modification. The polar plot shows concentric circles which reflects the breakdown in relationship between phase and final energy at any particular initial energy.

3.7 Outstanding Issues

It is difficult to produce a clear comparison between the two sheath definitions, since some fundamental conditions are addressed differently in each case. To provide a non-oscillatory solution to the full equation, the initial ion speed has to satisfy the Bohm Criterion, which is to say that $u_0 > (k_B T_e / m_i)^{1/2}$. Although this has been adhered to in order to obtain the sheath potential, when using the potential in the model, ions can have initial conditions freely imposed.

The inclusion of the electron influence introduces an extended sheath region, with a reduced electric field at the plasma side of the region. It could be argued that this is a step closer to including a pre-sheath that accelerates ions before entering the main (electron free) sheath region. Unfortunately this still doesn't strictly address the Bohm speed criterion, it would be of value to investigate this issue further.

Chapter 4

**Neutral Dynamics:
Dielectrophoresis (DEP)**

4.1 Background

As etching progresses in a plasma processing system, particles are removed from the substrate and must therefore be present immediately above it. This poses the question - how are the particles then removed from the vicinity of the substrate? A macroscopic flow exists within the processing chamber due to the pumping of feedstock gases through the vessel. It is not necessarily the case that this flow will greatly affect particles everywhere and in particular close to the surface or within surface features. Please note that for the sake of brevity, the term 'particle' refers to a neutral molecule or atom.

As a trench is etched, the aspect ratio (depth : width) will gradually increase. If a deep trench is required, at some point the depth will be significantly greater than the width and the aspect ratio will be regarded as high. This chapter looks at this extreme case where a high aspect ratio feature has formed on a substrate.

4.2 Dielectrophoresis

Dielectrophoresis (DEP) refers to the motion produced by the action of a nonuniform electric field upon neutral matter [38]. This is important in the characterisation of varieties of biological cells, and in the manipulation of sub-micrometer latex spheres [39; 40]. A similar effect for magnetic dipoles and strong magnetic fields is exploited in ferrofluids [41]. It is required that an electric dipole moment must exist in the neutral matter, this may be either permanent, or induced by the electric field in question. To be clear, in this work DEP is taken to mean the force exerted upon neutral, non-interacting particles with a permanent dipole moment by an externally imposed non-uniform electric field. This is consistent with Jones' phenomenological definition [42]. In simple terms, DEP causes affected particles to drift to the region of strongest electric field, irrespective of the polarity of the field.

Let a particle have electric dipole moment \mathbf{p} , and suppose that there is a non-uniform electric field \mathbf{E} present. Then the force \mathbf{F} acting on the particle is given by [43]

$$\mathbf{F} = (\mathbf{p} \cdot \nabla)\mathbf{E}. \quad (4.1)$$

4.3 Application to Plasma Processing

Suppose a particle with an electric dipole moment is ejected into the sheath region directly above the substrate surface. This molecule will be exposed to a strong sheath electric field that is spatially non-uniform (and usually varying in time). Setting aside the temporal variation, the sheath electric field will be directed from the plasma to the substrate, with intensity decreasing towards the sheath edge nearest the plasma. The DEP effect will tend to force the particle back on to the surface, where the field intensity is greatest. This may be an important consideration in analysing redeposition mechanisms and the associated sticking factor (see [44] for a discussion of these effects). However these systems are pumped, and eventually waste material is exhausted. Where the etched surface is not a level plane, the efficiency of the system pumping may be less effective at extracting etching by-products, particularly where etching takes place in very narrow ($0.2 \mu\text{m}$) and deep ($4 \mu\text{m}$) channels. It is in this specific situation that the DEP effect may be most significant. In such a deep channel, the electric field at the opening must have a large spatial rate of change because of the boundary shape and the associated dimensions.

It is proposed that the strong, spatially non-uniform plasma sheath electric field allows neutral dielectric atoms or molecules to be extracted from etched trenches via the DEP effect.

4.4 Model trench calculation

As a trial calculation, consider the potential of a rectangular well, representing a trench feature on a substrate (see Figure 4.1). Assume that the potential in the main sheath is ϕ_1 at the opening of the trench, and that the potential on the whole substrate, including the interior boundary of the well, is ϕ_2 . We can solve Laplace's equation to find the potential in the interior of the model trench, and thereby calculate the electric field intensity as a function of position. This is an idealised calculation (for example, there is no time dependence), but it does give some useful insight.

Since the absolute value of the potential is not crucial in this calculation (only the electric field is important for the dielectrophoresis effect) we can arbitrarily set the potential of the trench boundary to 0, and the potential at the mouth (supplied by the

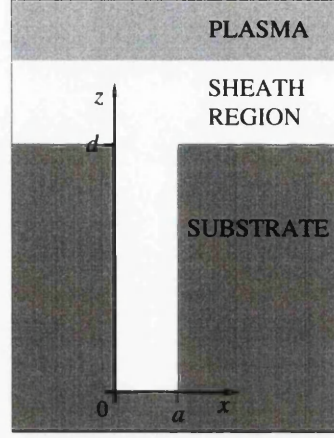


Figure 4.1: Diagram showing the geometry of a large aspect ratio trench. The axis indicate the coordinate orientation and model dimensions.

main plasma sheath) as $\phi_0 = \phi_1 - \phi_2$. This makes the handling of boundary conditions simpler by eliminating constants.

Given that the geometry is rectangular, we can find a general solution for $\phi(x, z)$, from Laplace's equation

$$\nabla^2 \phi = 0. \quad (4.2)$$

This equation is separable and in two dimensions becomes

$$\phi_z \frac{d^2 \phi_x}{dx^2} + \phi_x \frac{d^2 \phi_z}{dz^2} = 0 \quad (4.3)$$

and dividing through by $\phi_x \phi_z$

$$\frac{1}{\phi_x} \frac{d^2 \phi_x}{dx^2} + \frac{1}{\phi_z} \frac{d^2 \phi_z}{dz^2} = 0 \quad (4.4)$$

These two terms must sum to zero at all points. Since the second term is independent of x , the first must also be independent of x and so constant. By similar reasoning, the second term is also constant.

$$\frac{1}{\phi_x} \frac{d^2 \phi_x}{dx^2} = C_1, \quad (4.5)$$

$$\frac{1}{\phi_z} \frac{d^2 \phi_z}{dz^2} = C_2, \quad (4.6)$$

$$\text{also, } C_1 + C_2 = 0 \quad (4.7)$$

The above differential equations can be solved to give a general solution to $\phi(x, z)$ of the form:

$$\phi(x, z) = [C_1 \cosh(kz) + C_2 \sinh(kz)][C_3 \cos(kx) + C_4 \sin(kx)]. \quad (4.8)$$

The boundary conditions for the problem are as follows. The trench width is a and its depth is d . The bottom of the trench ($z = 0, 0 \leq x \leq a$) is at zero potential, as is each of the top corners ($(x, z) = (0, d)$ and $(x, z) = (a, d)$); the open mouth of the trench is at potential ϕ_0 ($z = d, 0 < x < a$). This gives a rectangular box with three sides at one potential and the remaining side at a different potential. Applying these boundary conditions yields

$$\phi(x, z) = \sum_{n \text{ odd}} \frac{A \sinh(k_n z)}{n \sinh(k_n d)} \sin(k_n x), \quad (4.9)$$

where $k_n = n\pi/a$ and A is a constant. For large aspect ratio $\alpha = d/a \gg 1$, the first term in the sum dominates and a good approximation to ϕ is

$$\phi(x, z) \approx A \frac{\sinh(\pi z/a)}{\sinh(\pi d/a)} \sin(\pi x/a). \quad (4.10)$$

Taking the gradient of (4.10) to get the x and z components of the electric field \mathbf{E} in the trench yields

$$E_x = -\frac{\partial \phi}{\partial x} \simeq -\frac{\pi}{a} \phi_0 \sinh\left(\frac{\pi z}{a}\right) \cos\left(\frac{\pi x}{a}\right), \quad (4.11)$$

$$E_z = -\frac{\partial \phi}{\partial z} \simeq -\frac{\pi}{a} \phi_0 \cosh\left(\frac{\pi z}{a}\right) \sin\left(\frac{\pi x}{a}\right), \quad (4.12)$$

where $\phi_0 = A/\sinh(\pi d/a)$. Using (4.1) we can find the force acting upon the particle. The field magnitude as a function of position in the large aspect ratio trench interior is readily determined:

$$|E|^2 \simeq \frac{\sinh^2(\pi z/a)}{\sinh^2(\pi d/a)}, \quad (4.13)$$

showing that the electric field is predominantly aligned with the long axis of the trench, and is concentrated at the trench opening. The longitudinal electric field has an exponential fall-off with e-folding distance equal to the trench width a , so that a particle at the bottom of the trench sees an electric field which increases exponentially with height. There is also a horizontal component of electric field, which has peak magnitude in the centre.

For large aspect ratio trenches, it is the exponential behaviour which dominates. This is a satisfactory result for two reasons: it shows that there is negligible lateral electric field, consistent with no under-cutting in plasma etching. Also, the field distribution can draw particles with a dipole moment up from the trench bottom, and away from the walls, as argued qualitatively in the previous section. In fact, modest charge build-up at the top corners of large aspect ratio trenches can induce an additional DEP effect, but

at the expense of causing under-cutting [45]. Note also that as the aspect ratio reduces, the lateral variation in electric field strength becomes relatively more significant.

4.5 Numerical Simulation

4.5.1 Equation of Motion

The components of electric field in x and z directions, E_x and E_z are given in (4.11) and (4.12) respectively. Equation (4.1) is used to express the acceleration acting on a particle. In two dimensions:

$$(\mathbf{p} \cdot \nabla) \mathbf{E} = (p_x \partial_x + p_z \partial_z) \mathbf{E} \quad (4.14)$$

$$= \hat{x} [p_x \partial_x E_x + p_z \partial_z E_x] + \hat{z} [p_x \partial_x E_z + p_z \partial_z E_z] \quad (4.15)$$

$$= \frac{\pi^2}{a^2} \phi_0 \left(\hat{x} \left[p_x \sinh\left(\frac{\pi z}{a}\right) \sin\left(\frac{\pi x}{a}\right) - p_z \cosh\left(\frac{\pi z}{a}\right) \cos\left(\frac{\pi x}{a}\right) \right] \right. \\ \left. + \hat{z} \left[-p_x \cosh\left(\frac{\pi z}{a}\right) \cos\left(\frac{\pi x}{a}\right) - p_z \sinh\left(\frac{\pi z}{a}\right) \sin\left(\frac{\pi x}{a}\right) \right] \right) \quad (4.16)$$

Since it is assumed that the electric dipole moment and the electric field are aligned $\hat{\mathbf{p}} = \hat{\mathbf{e}}$, where $\hat{\mathbf{e}} = p\mathbf{E}/|E|$.

$$\frac{\mathbf{E}}{|E|} = - \frac{\hat{x} \sinh\left(\frac{\pi z}{a}\right) \cos\left(\frac{\pi x}{a}\right) + \hat{z} \cosh\left(\frac{\pi z}{a}\right) \sin\left(\frac{\pi x}{a}\right)}{\sqrt{\sinh^2\left(\frac{\pi z}{a}\right) \cos^2\left(\frac{\pi x}{a}\right) + \cosh^2\left(\frac{\pi z}{a}\right) \sin^2\left(\frac{\pi x}{a}\right)}} \quad (4.17)$$

so

$$\hat{e}_x = - \frac{\sinh\left(\frac{\pi z}{a}\right) \cos\left(\frac{\pi x}{a}\right)}{\sqrt{\sinh^2\left(\frac{\pi z}{a}\right) + \sin^2\left(\frac{\pi x}{a}\right)}}, \quad (4.18)$$

$$\hat{e}_z = - \frac{\cosh\left(\frac{\pi z}{a}\right) \sin\left(\frac{\pi x}{a}\right)}{\sqrt{\sinh^2\left(\frac{\pi z}{a}\right) + \sin^2\left(\frac{\pi x}{a}\right)}}. \quad (4.19)$$

Considering that $\hat{\mathbf{p}} = p\hat{\mathbf{e}}$

$$(\mathbf{p} \cdot \nabla) \mathbf{E} = p(\hat{\mathbf{e}} \cdot \nabla) \mathbf{E} \quad (4.20)$$

$$= p \frac{\pi^2}{a^2} \phi_0 \left(\hat{x} \left[e_x \sinh\left(\frac{\pi z}{a}\right) \sin\left(\frac{\pi x}{a}\right) - e_z \cosh\left(\frac{\pi z}{a}\right) \cos\left(\frac{\pi x}{a}\right) \right] \right. \\ \left. - \hat{z} \left[e_x \cosh\left(\frac{\pi z}{a}\right) \sin\left(\frac{\pi x}{a}\right) + e_z \sinh\left(\frac{\pi z}{a}\right) \cos\left(\frac{\pi x}{a}\right) \right] \right). \quad (4.21)$$

Substituting (4.18) and (4.19) in the above and simplifying

$$m\ddot{\mathbf{r}} = p(\hat{\mathbf{e}} \cdot \nabla \mathbf{E}) \quad (4.22)$$

$$\begin{aligned} \ddot{\mathbf{r}} = \frac{p}{m} \frac{\pi^2}{a^2} \phi_0 \left(\hat{\mathbf{x}} \left[\frac{\sin(\frac{\pi x}{a}) \cos(\frac{\pi x}{a})}{\sqrt{\sinh^2(\frac{\pi z}{a}) + \sin^2(\frac{\pi x}{a})}} \right] \right. \\ \left. + \hat{\mathbf{z}} \left[\frac{\sinh(\frac{\pi z}{a}) \cosh(\frac{\pi z}{a})}{\sqrt{\sinh^2(\frac{\pi z}{a}) + \sin^2(\frac{\pi x}{a})}} \right] \right). \end{aligned} \quad (4.23)$$

4.5.2 Non-dimensional Representation

Once normalised to the trench width a , $\xi = x/a$ and $\zeta = z/a$ are the non-dimensional spatial coordinates. Time is normalised to the ion transit time without DEP effect, $t_0 = d/v_0$, yielding non-dimensional time $\tau = t/t_0$. The acceleration of the particle can now be expressed as:

$$\frac{d^2 \xi}{d\tau^2} = \frac{1}{2} \beta \frac{\sin(2\pi\xi)}{\sqrt{\sinh^2(\pi\zeta) + \sin^2(\pi\xi)}}, \quad (4.24)$$

$$\frac{d^2 \zeta}{d\tau^2} = \frac{1}{2} \beta \frac{\sinh(2\pi\zeta)}{\sqrt{\sinh^2(\pi\zeta) + \sin^2(\pi\xi)}}, \quad (4.25)$$

where β is a fundamental parameter which incorporates the dipole moment p , particle mass m , aspect ratio α , launch velocity v_0 , potential at the top of the trench ϕ_0 and trench width a :

$$\beta = \pi^2 \frac{p \alpha^2 \phi_0}{m v_0^2 a}. \quad (4.26)$$

Typically $p = 10^{-30}$ Cm, $\alpha = 4$, $m = 4.68 \times 10^{-26}$ kg (silicon), $a = 10^{-6}$ m and $v_0 = 10^2$ ms⁻¹, yielding

$$\beta \simeq O(1) \text{ if } \phi_0 \simeq O(3). \quad (4.27)$$

4.6 Results

4.6.1 At Aspect Ratio of 4

The consequences of the DEP effect are computed using the above normalised coordinates and illustrated in the following figures.

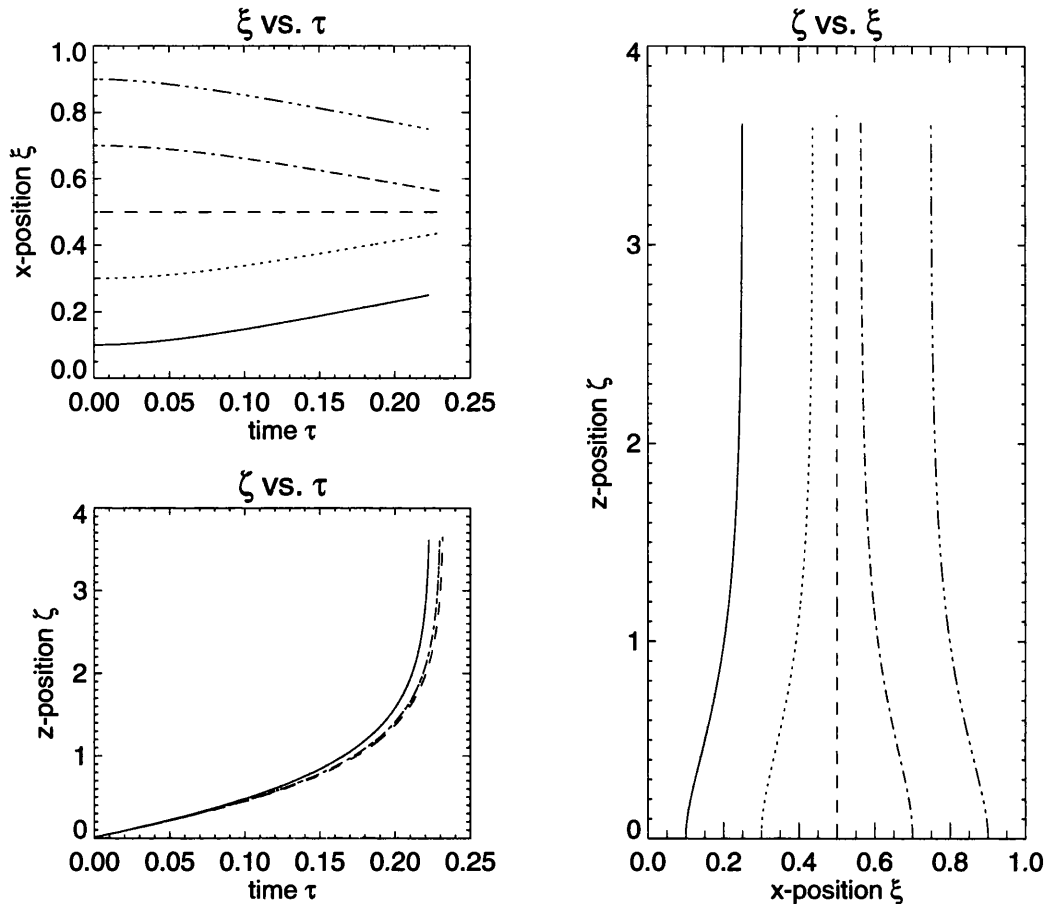


Figure 4.2: Particles ejected perpendicular to the bottom of the trench, $\beta = 1$. Particles are centred in the trench and exit in less time than without the DEP effect.

The first series of plots shows particles leaving from five positions equally spaced across the bottom of a trench with an aspect ratio of 4. The particles have no horizontal velocity component so are initially moving parallel to the trench walls. They have an initial velocity such that they would exit the trench at time $\tau = 1$, so the time shown in the plots indicates the reduced exit time relative to unity. Three plots are shown, for values of $\beta = 1$ (figure 4.2), $\beta = 10$ (figure 4.3) and $\beta = 100$ (figure 4.4).

There are several points to notice about these plots.

- The particles are ejected in a fraction of the time that it would have taken without a dielectrophoretic force. This ranges from 0.7 for a particle in the centre of the trench with $\beta = 1$ to 0.045 when a particle is ejected from the side of the trench with conditions which give $\beta = 100$. Note that the particles are accelerated more when they approach the upper part of the trench.

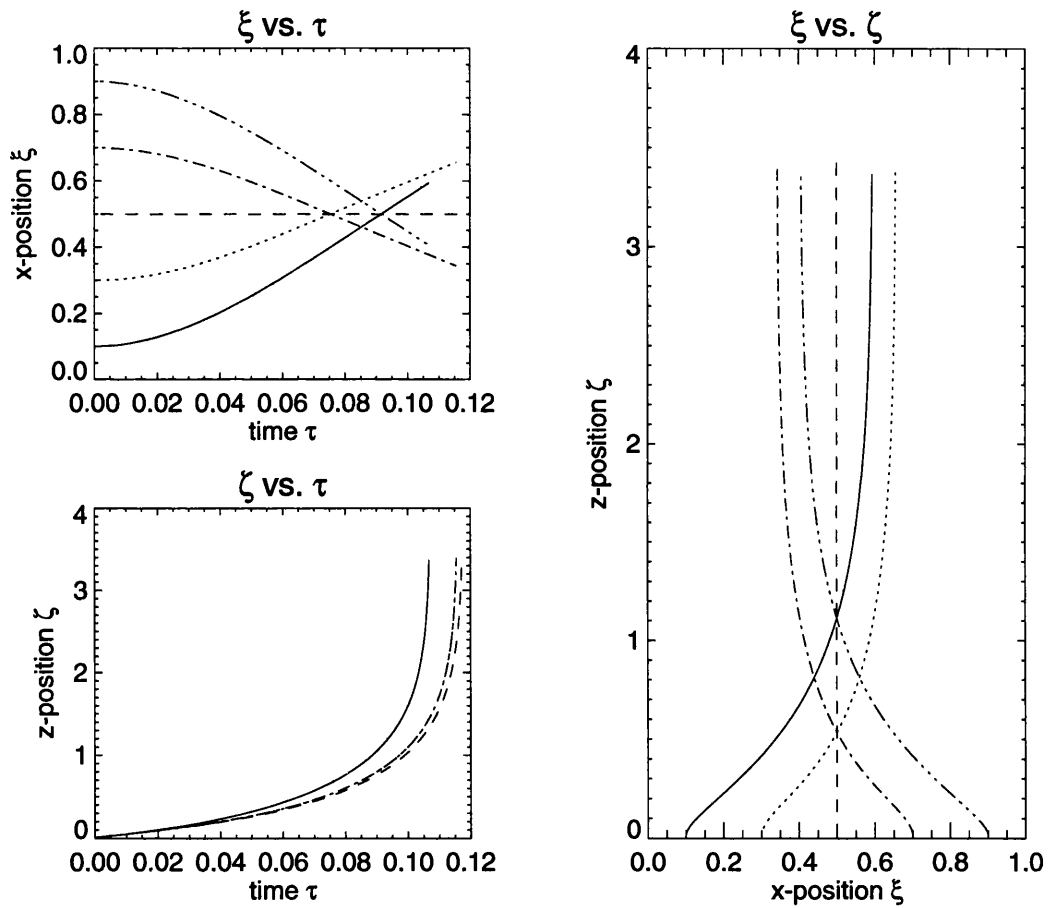


Figure 4.3: Particles ejected perpendicular to the bottom of the trench, $\beta = 10$. A strong centring force causes the particles to overshoot the centre line. Exit time is much less than that without the DEP effect.

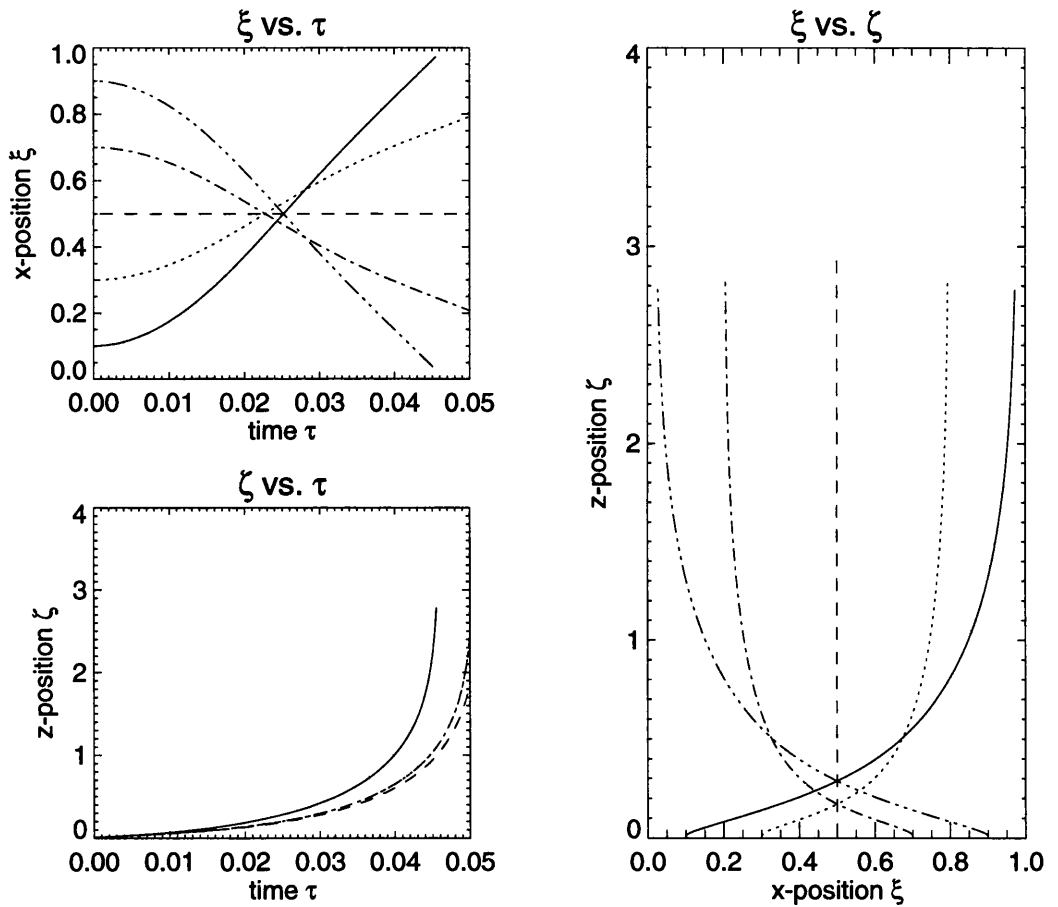


Figure 4.4: Particles ejected perpendicular to the bottom of the trench, $\beta = 100$. A very strong centring force causes the particles to nearly overshoot into the opposite wall. Exit time is a small fraction of that without the DEP effect.

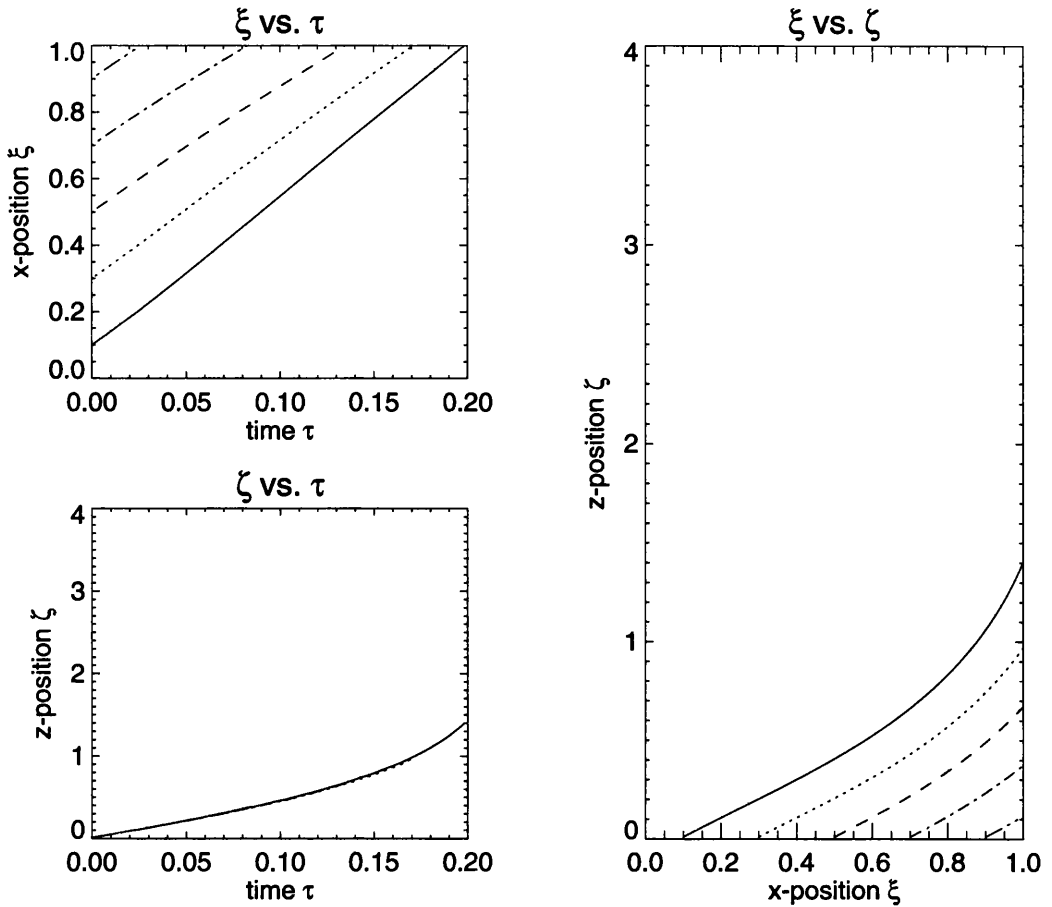


Figure 4.5: Particles ejected at 45° to the bottom of the trench, $\beta = 1$. The centring force is not sufficient to prevent the particles from striking the side wall.

- The particles are deflected towards the centre of the trench. This effect is most dominant in the lower portion of the trench. The centring of particles is greater with increasing value of β . Because the effect is stronger towards the bottom of the trench, a particle may be strongly deflected when it is initially ejected into the trench, then as it moves upwards the centring force is reduced so the particle overshoots the centre line and heads towards the opposite wall. This can be seen in the case $\beta = 100$ (figure 4.4).

The second series of plots are similar to those above. They differ in the initial velocity of the particles, now they are ejected at 45° to the trench walls. Plots for $\beta = 1, 10$ & 100 are given in figures 4.5, 4.6 & 4.7 respectively.

Immediately after the particles are liberated from the substrate, they are in the region subject to the most significant centring force. As they move upwards, the centring force

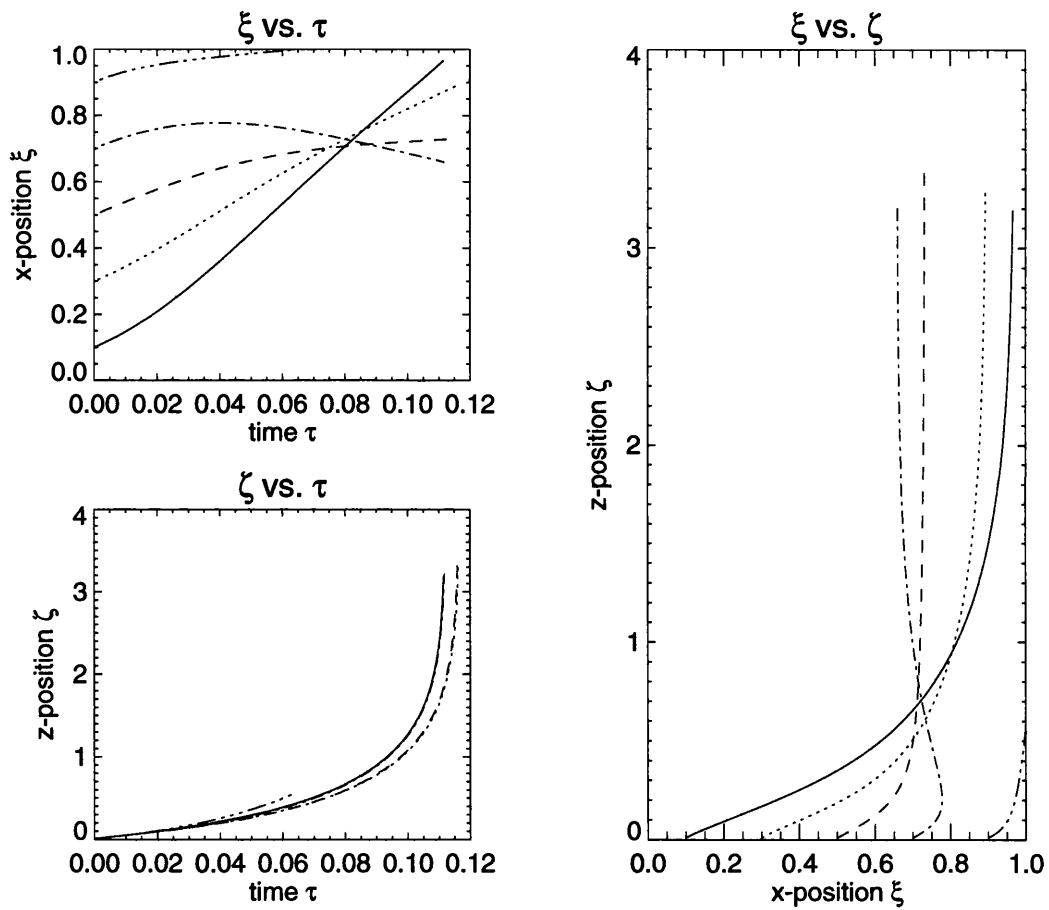


Figure 4.6: Particles ejected at 45° to the bottom of the trench, $\beta = 10$. All but the closest particles are centred enough to prevent them from striking the side wall.

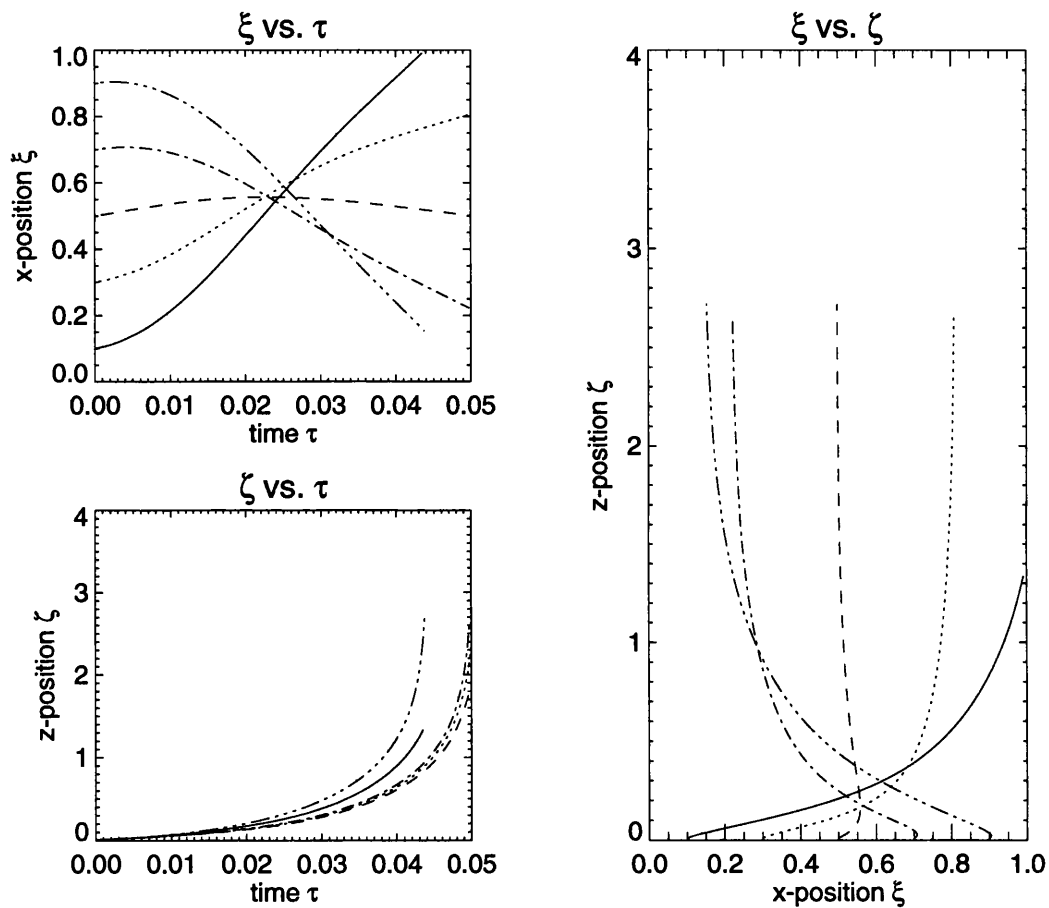


Figure 4.7: Particles ejected at 45° to the bottom of the trench, $\beta = 100$. All the particles leave the trench without striking the side wall except for one. This time the combination of the 45° starting trajectory and the centring force cause a particle to strike the wall furthest from its starting position.

becomes considerably less dominant. This can result in a situation where a particle is far off the centre line, so a force acts on it as it is liberated from the substrate to move it towards the centre. In the time it takes for this to happen the particle has moved into a region with relatively little centring force, so the particle overshoots the centre and heads towards the opposite wall. In many cases the now increasing vertical force ejects the particle before it has time to strike the wall.

4.6.2 Variation in Aspect Ratio

The following plots show only ξ versus τ and ζ versus τ in the interests of compactness. On each page, plots for $\beta = 1, 10$ and 100 are shown from top to bottom. Aspect ratios of 2, 8 and 16 are presented, with particles leaving the trench under a range of conditions.

The first three series of plots show particles leaving perpendicular to the bottom of the trench, aspect ratio 2 in figure 4.8, 8 in figure 4.9 and 16 in figure 4.10. With particles leaving at 45° to the bottom of the trench, the results can be seen for an aspect ratio of 2 in figure 4.11, 8 in figure 4.12 and 16 in figure 4.13. All the plots shown prior to these were for an aspect ratio of 4, so can also be used in comparison.

Two observations are made about these results:

- Increasing the aspect ratio causes a proportionate reduction in the time taken to exit the trench. In summary:

Aspect Ratio	τ		
	$\beta = 1$	$\beta = 10$	$\beta = 100$
2	0.43	0.21	0.90
4	0.23	0.11	0.047
8	0.11	0.055	0.024
16	0.057	0.027	0.012

This is a result of the increase in the vertical field gradient as trench aspect ratio increases.

- Regardless of the aspect ratio, the motion in the ξ direction looks the same simply scaling to the new time to exit. Take as an example a particle that initially heads towards a wall but is centered, so exits without touching a wall in a trench with

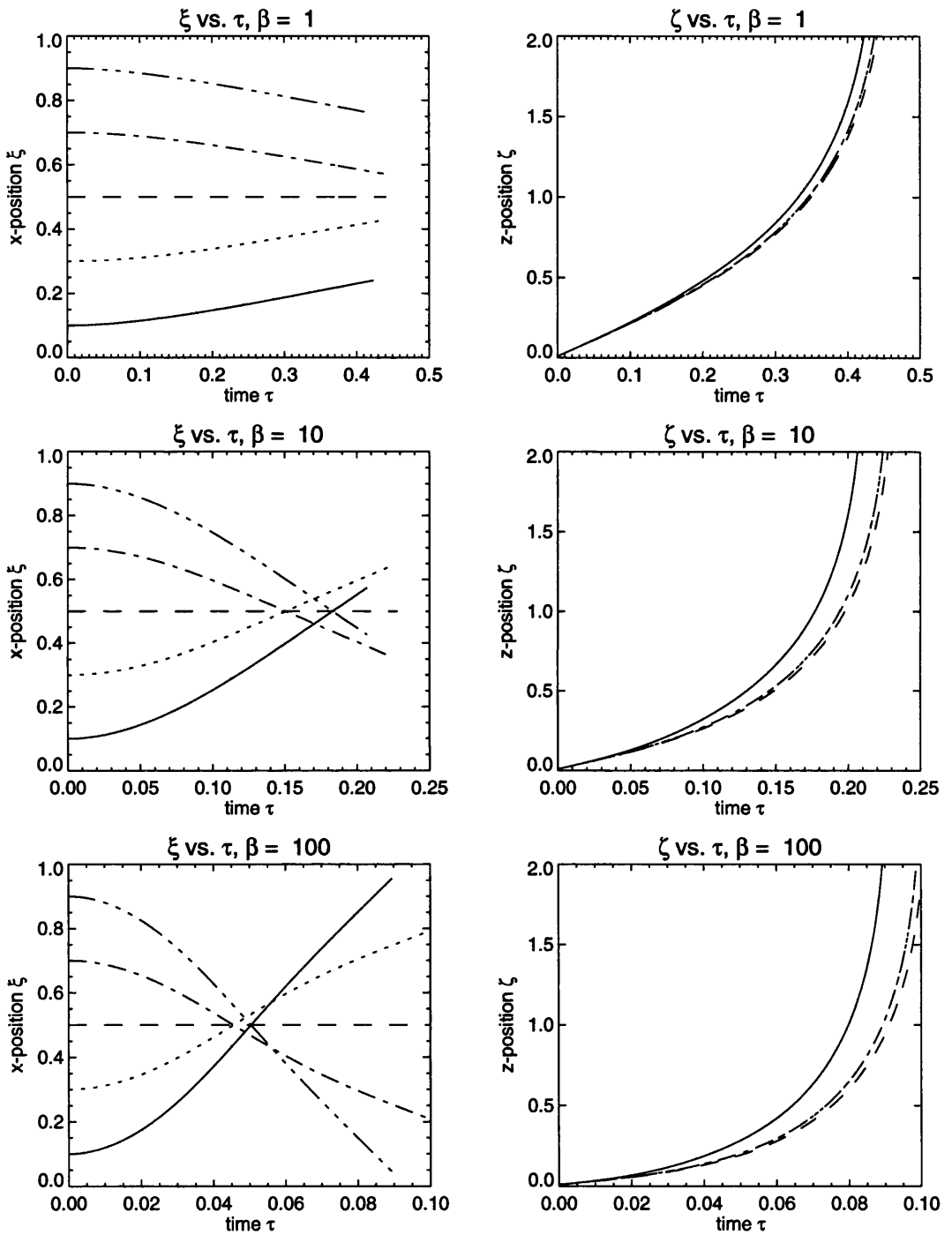


Figure 4.8: Particles ejected perpendicular to the bottom of a trench with aspect ratio = 2. Position of particles in ξ and ζ direction with respect to τ , for three values of β .

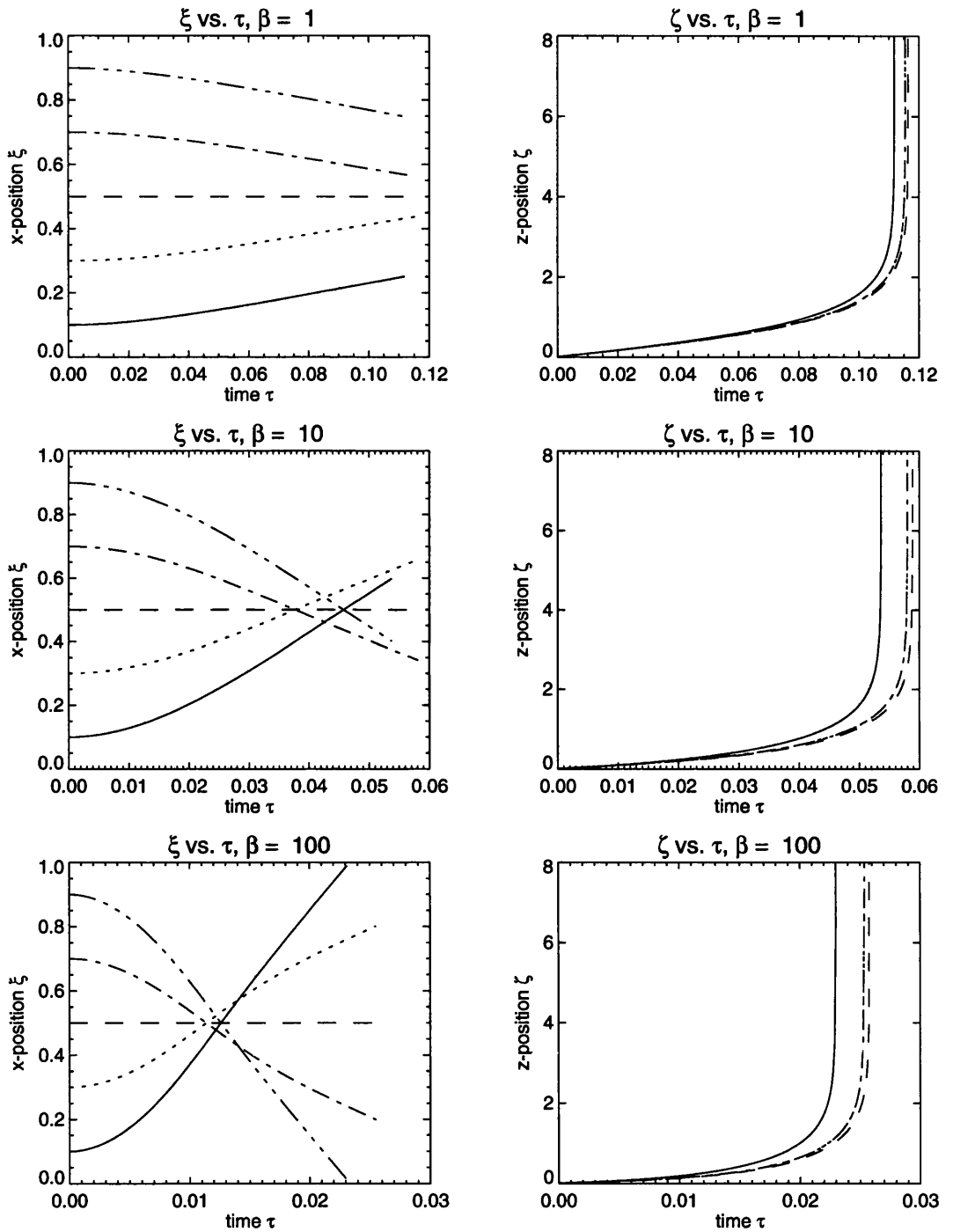


Figure 4.9: Particles ejected perpendicular to the bottom of a trench with aspect ratio = 8. Position of particles in ξ and ζ direction with respect to τ , for three values of β .

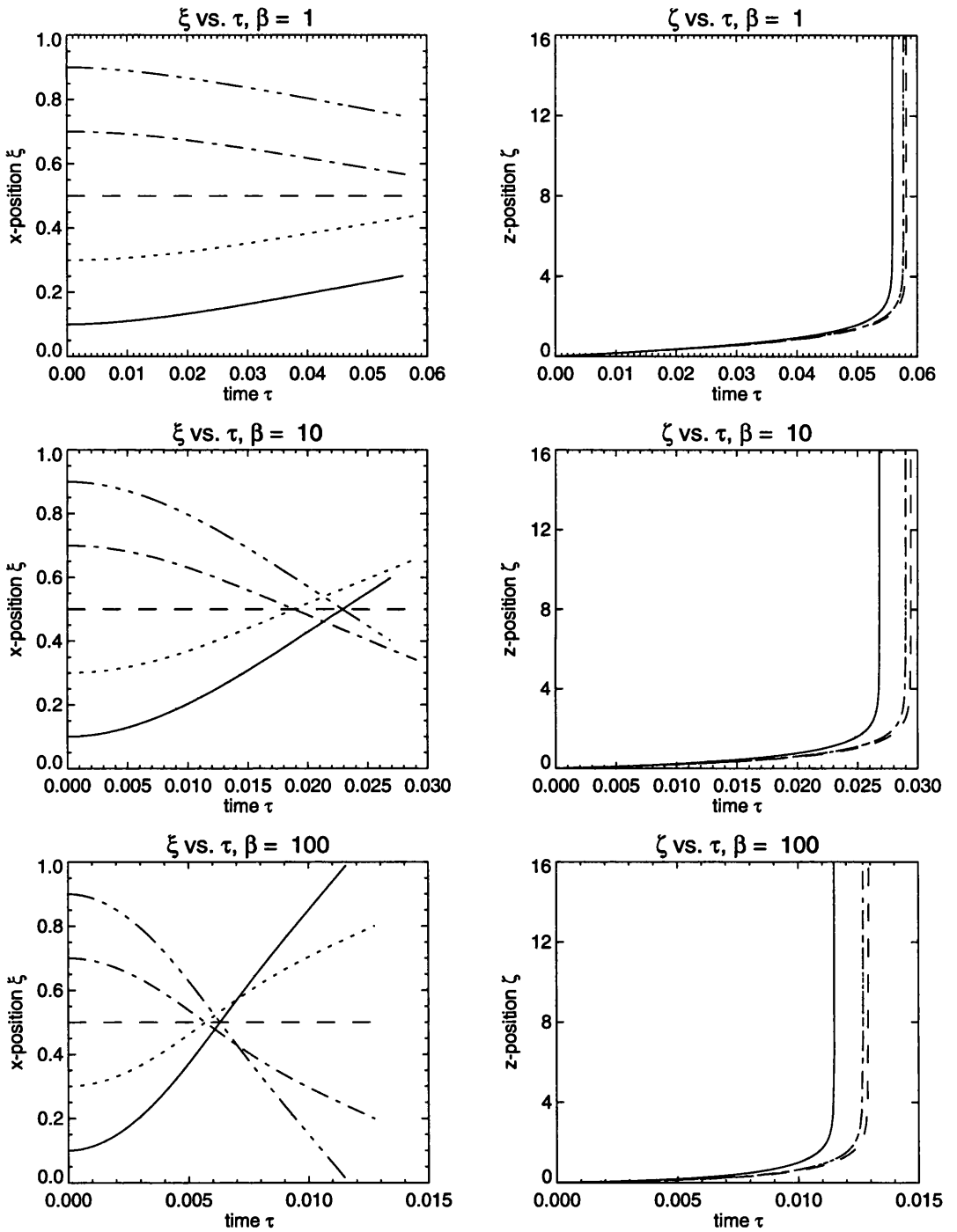


Figure 4.10: Particles ejected perpendicular to the bottom of a trench with aspect ratio = 16. Position of particles in ξ and ζ direction with respect to τ , for three values of β .

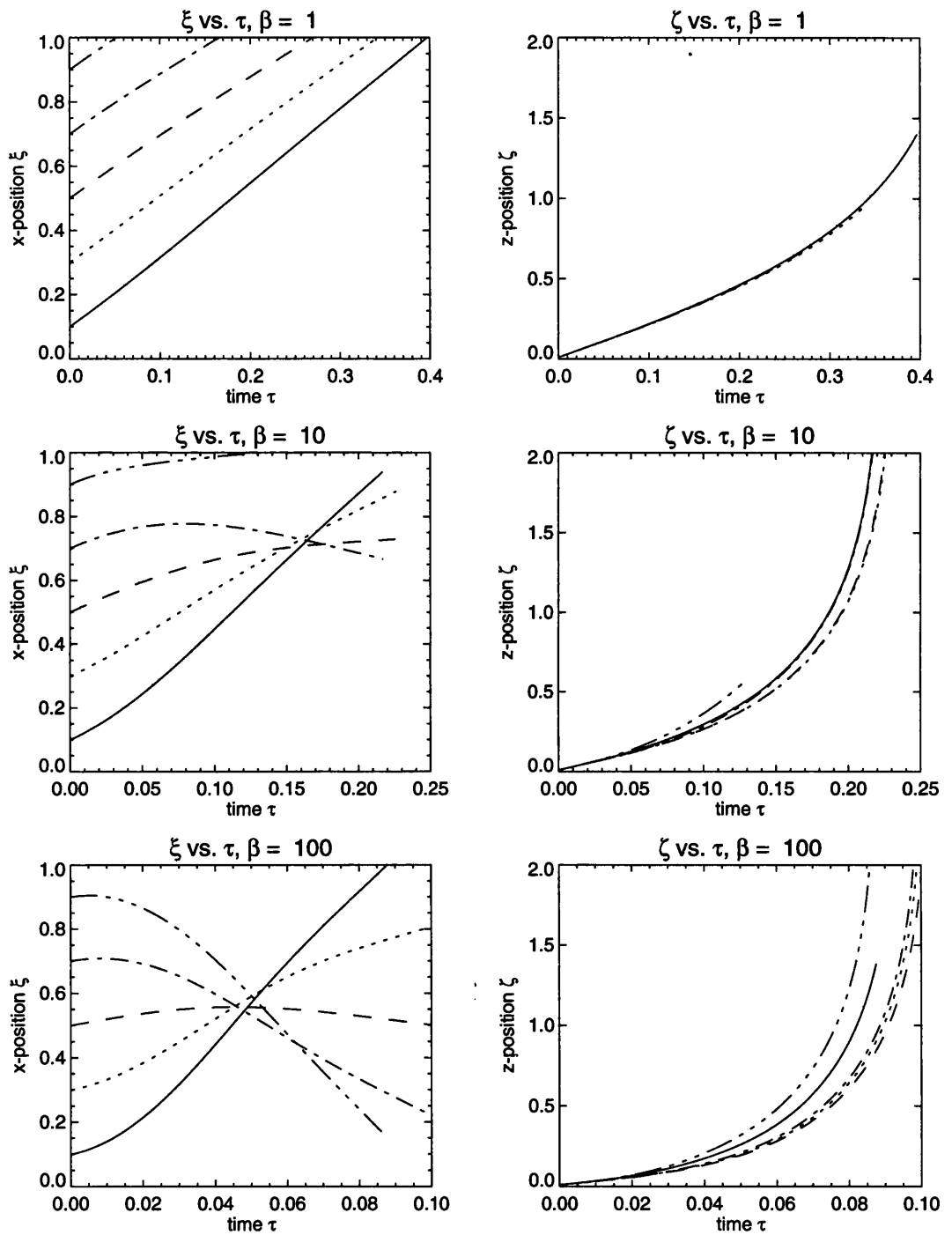


Figure 4.11: Particles ejected at 45° to the bottom of a trench with aspect ratio = 2. Position of particles in ξ and ζ direction with respect to τ , for three values of β .

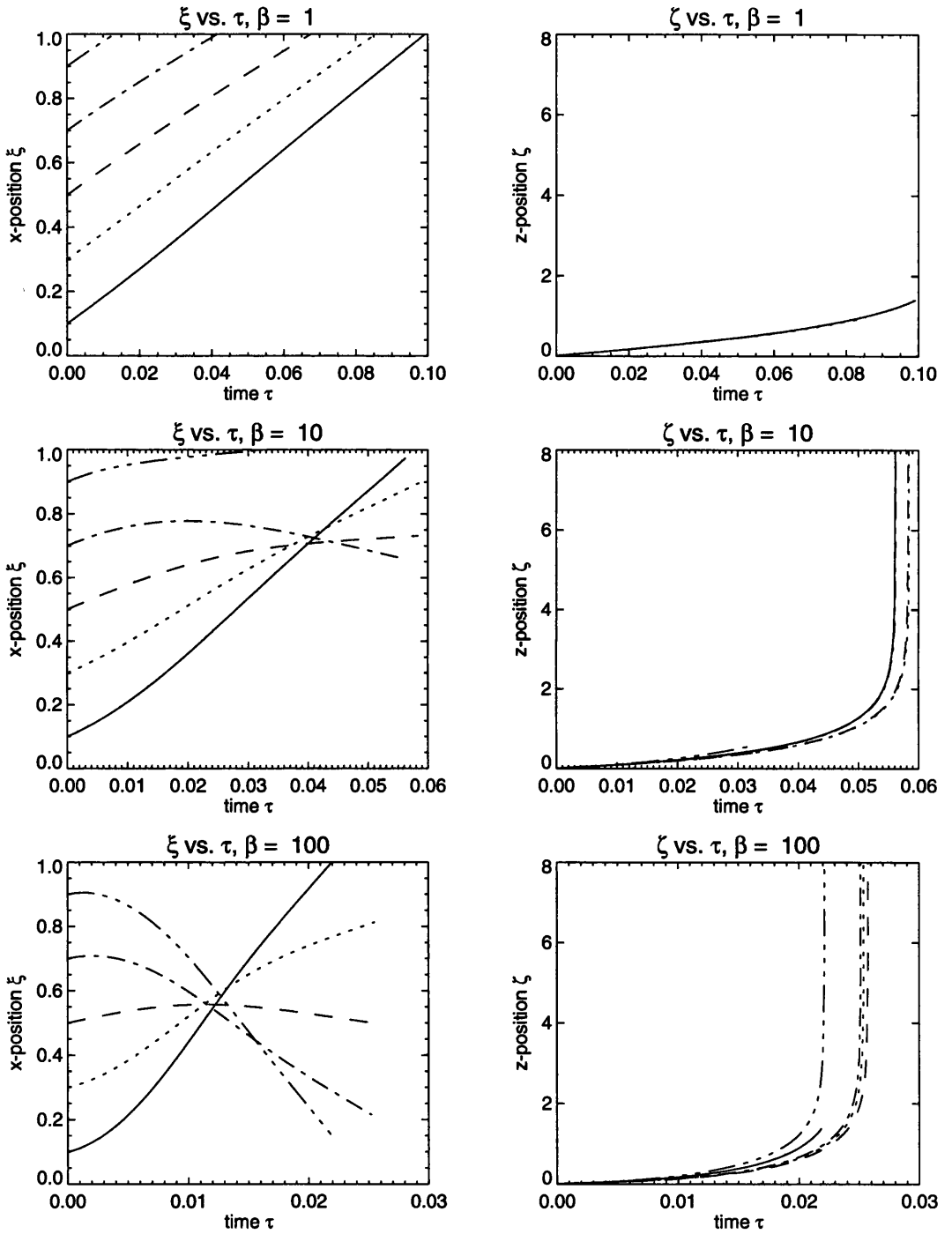


Figure 4.12: Particles ejected at 45° to the bottom of a trench with aspect ratio = 8. Position of particles in ξ and ζ direction with respect to τ , for three values of β .

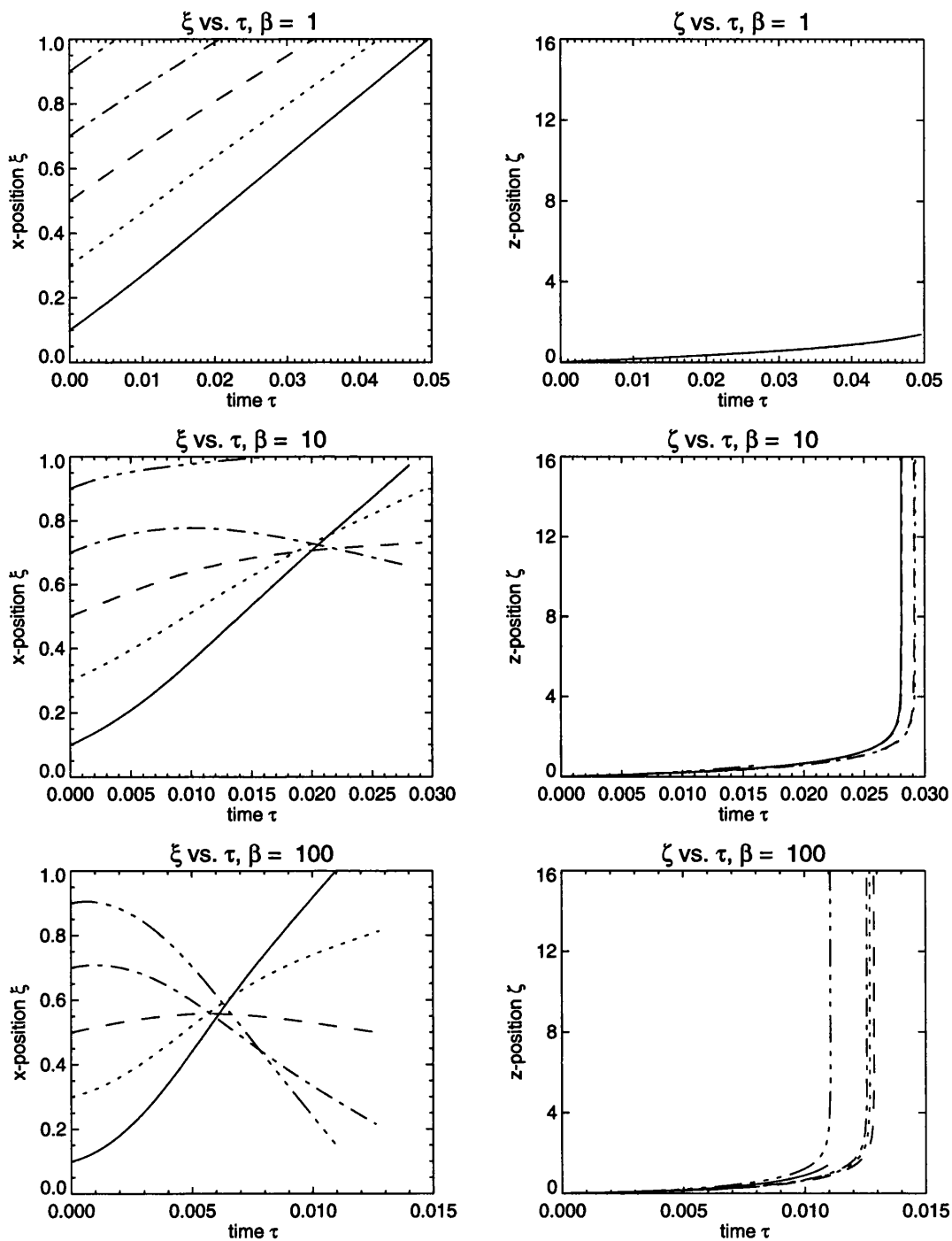


Figure 4.13: Particles ejected at 45° to the bottom of a trench with aspect ratio = 16. Position of particles in ξ and ζ direction with respect to τ , for three values of β .

aspect ratio 2. In the aspect ratio 16 trench, the field gradient is increased so as to centre the particle sooner, still exiting without striking the wall.

4.7 Discussion

The simple idea that neutral molecules can be extracted from deeply etched trenches via the force exerted by the non-uniform sheath field on their electric dipole moment is an attractive one, with genuine application in realistic situations.

A typical etch product when etching SiO_2 in a CF_4 plasma is SiF_2 [22], which has a permanent dipole moment of $4.1 \times 10^{-30} \text{Cm}$ [46]. There are many other particles present immediately above the substrate which may or may not have a permanent dipole moment. The work presented here deals only with permanent dipole moments, but molecules such as SiF_4 which are symmetrical and therefore carry no permanent dipole moment may become polarised in the strong electric field. This would result in an induced dipole moment which would be a function of position.

Moreover, there is the possibility of a further effect if the force on N particles acting under the influence of (4.1) is considered. The force per unit volume on N such particles is $(\mathbf{P} \cdot \nabla)\mathbf{E}$ where $\mathbf{P} = N\mathbf{p}$, and where N is the particle number density. The total fluid consists of a particle fluid, in this case the neutral particles under the DEP force and a carrier fluid, here the remaining gas without the neutral particles under the DEP force. Given that $\mathbf{P} = (\epsilon_p - \epsilon_c)\epsilon_0\mathbf{E}$, where ϵ_p is the relative permittivity of the particle fluid and ϵ_c is the relative permittivity of the carrier fluid, the force per unit volume exerted on the fluid in the presence of the non-uniform electric field in a plasma can be written as [43]

$$\mathbf{F}_{total} = (\epsilon_p - \epsilon_r)\epsilon_0(\mathbf{E} \cdot \nabla)\mathbf{E} = \frac{1}{2}(\epsilon_p - \epsilon_r)\epsilon_0\nabla E^2. \quad (4.28)$$

The relative permittivity of a plasma is a function of frequency: $\epsilon_r = 1 - \omega_p^2/[\omega(\omega - i\nu)]$ [47] where ν is the electron-neutral collision frequency. This raises the possibility of manipulating the frequency of the applied AC field in the plasma reactor to change the bulk force on the neutral component in the plasma mixture, so changing the neutral transport.

4.8 More Complete Potential Calculation

The above calculations depend upon the simplification of the potential to the first term in the series derived from Laplace's equation. This section develops a method to numerically solve the DEP equations, starting from an arbitrary potential definition. This allows the DEP effect to be examined for a region of interest where the potential is defined by a separate routine. Existing potential solving routines can provide input which describes any required feature shape.

As a first step, the potential for the previously used trench can be calculated more accurately by increasing the number of terms taken from (4.9). A routine can iteratively calculate the sum across a suitable grid, to the required accuracy.

Potential Calculation

A program subroutine evaluates equation (4.9) on a square grid for $\xi = 0$ to 1 and $\zeta = 0$ to ar , where ar is the aspect ratio. A fine grid is required to provide the necessary resolution at the bottom of the trench, where the particle will be moving slowly, relative to its final velocity.

Although in this example the same boundary conditions are being used as in the previous section, it is possible to specify any shaped potential across the grid. This allows for any geometrical configuration that might be of interest.

The summing of many terms from equation (4.9) results in a function which approaches a square wave evaluated from 0 to π . In a 32-bit floating point representation numbers up to 10^{38} can be used, a 64-bit double precision representation will allow up to 10^{308} . Either way an upper limit is present and since the hyperbolic functions $\sinh(n\pi\zeta)$ and $\cosh(n\pi\zeta)$ are being evaluated, this limit will be rapidly reached. Because it is not feasible to evaluate this function to infinity, a well defined square wave will only be approximated. This is illustrated in figure 4.14 which shows cross-sections of potential across the trench at different positions in ζ , for three values of n .

The case $n = 1$ is equivalent to the analytic approximation, where only the first term in the series describing the potential was taken. The case $n = 27$ approaches the originally defined boundary condition where the top of the trench was at a single potential. At the top of the trench the effect of taking more terms is clearly evident.

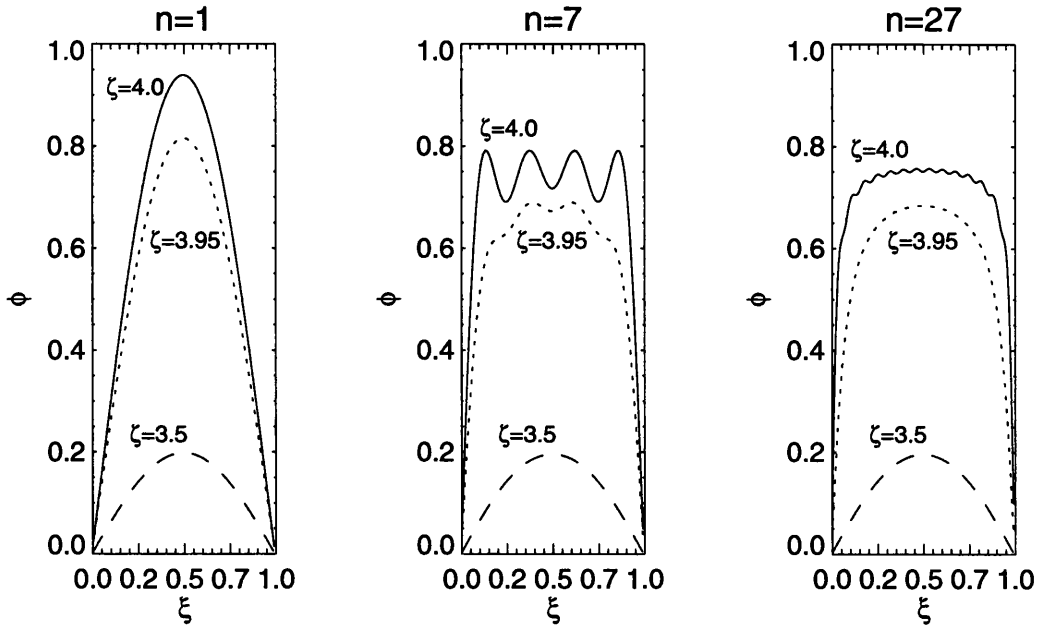


Figure 4.14: Cross-section of potential across the top of the trench and two points in the interior. 1, 7 and 27 terms in the series that describes the potential are used. Note that it is only at the top of the trench that a high number of terms are required to represent the potential accurately.

Moving down the trench, the potential profile rapidly becomes similar for all values of n .

Potential Field

A subroutine takes the potential and finds the gradient at each point in the grid. This is performed by a centre averaging method, finding the gradient at a half grid step before and after the point in question and averaging it. In the ξ direction this is written:

$$\begin{aligned}
 E_{\xi_i} &= \frac{d\phi}{d\xi} \\
 &= \left[\frac{\phi - \phi_{i-1}}{d\xi} + \frac{\phi_{i+1} - \phi}{d\xi} \right] / 2 \\
 &= \frac{\phi_{i+1} - \phi_{i-1}}{2d\xi}.
 \end{aligned} \tag{4.29}$$

The same applies in the ζ direction.

The ξ and ζ components of \mathbf{E} are now available, but all that is required is the modulus

field strength $|E|$ at each point. This is readily obtained:

$$|E| = \sqrt{E_\xi^2 + E_\zeta^2} \quad (4.30)$$

Some care should be taken at the boundaries since at $i = 1$ and $i = i_{max}$ one of the neighbouring values will be absent (from the opposite side in each case). For this simulation the boundaries are not really of any concern because if a particle reaches a boundary then the simulation ends there, with no need to consider the effect of the boundary on the particle. It is satisfactory to copy the value of ξ_i (in the ξ direction) into the missing data point.

The number of terms summed in the series defining the potential has a definite effect on the resulting field. This can be seen for $n = 1$ in figure 4.15 and $n = 27$ in figure 4.16.

DEP force

The DEP force is found from the gradient of $|E|$, calculated by adopting a similar strategy to that of (4.29). As has already been seen above, different choices for n provide a change in the resulting force. Figure 4.17 results when $n = 1$, figure 4.18 when $n = 27$.

4.8.1 Discussion of Graphical Results

The reader is asked to consider these results for a moment, in order to understand the features that arise due to the formulation of this model.

Most importantly, it is observed that the potential and everything that follows from it is the same away from the top corners of the trench for both $n = 1$ and $n \gg 1$. Comparing the contour labels on figures 4.15 and 4.16 shows this most clearly. When a particle has reached the upper region of the trench it will have been acted on by the DEP force for some time, so a very local large force will not greatly affect the outcome. Firstly, because the force is local the particle is not likely to encounter it at all. Secondly, if the force is encountered, the integral force over the whole trajectory will not be dominated by the last portion.

The reason for the departure from the result seen for $n = 1$ as n becomes $\gg 1$ can be readily explained. In the case $n = 27$, the potential across the top of the trench

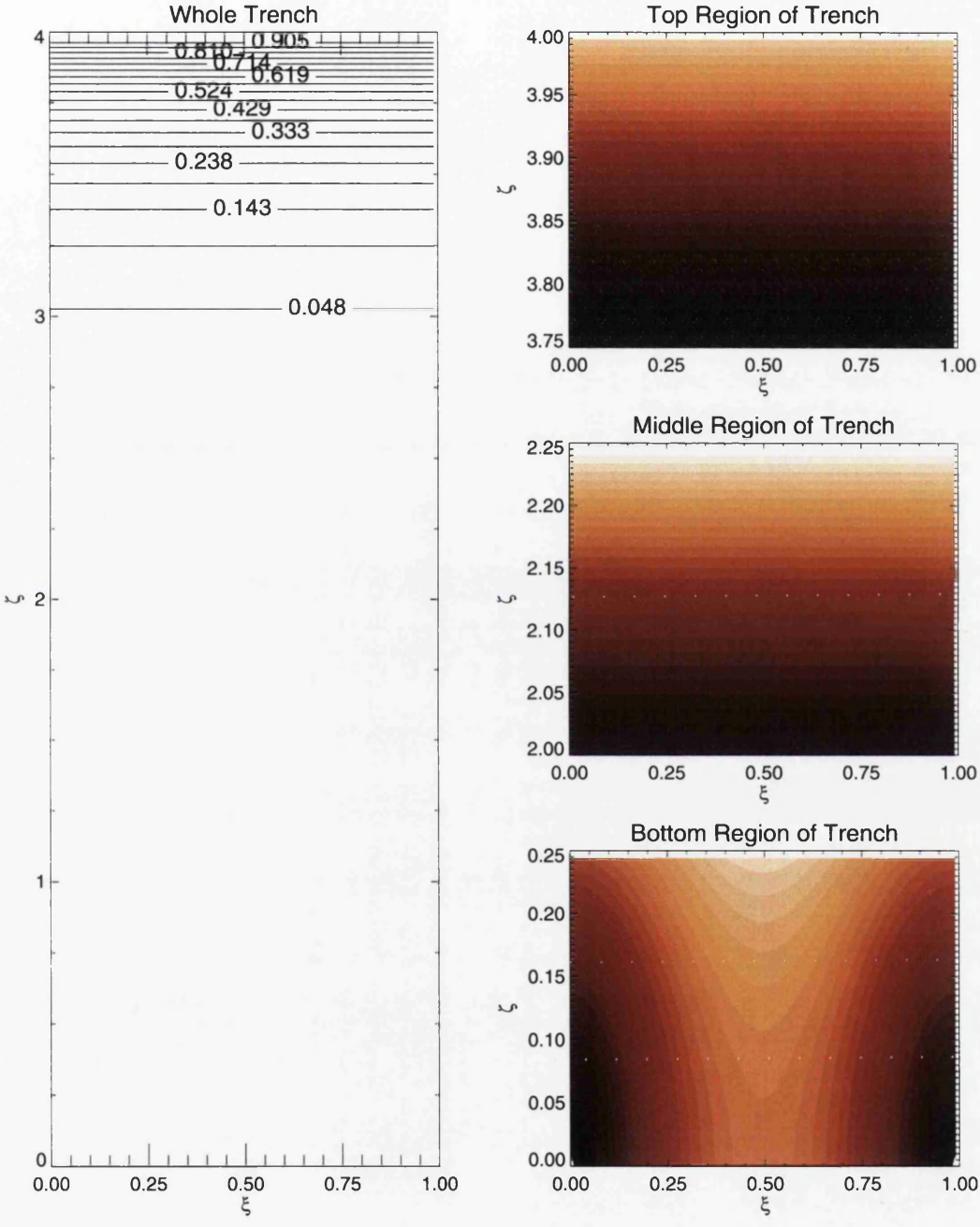


Figure 4.15: Electric field strength in the whole trench and in selected regions when $n = 1$.

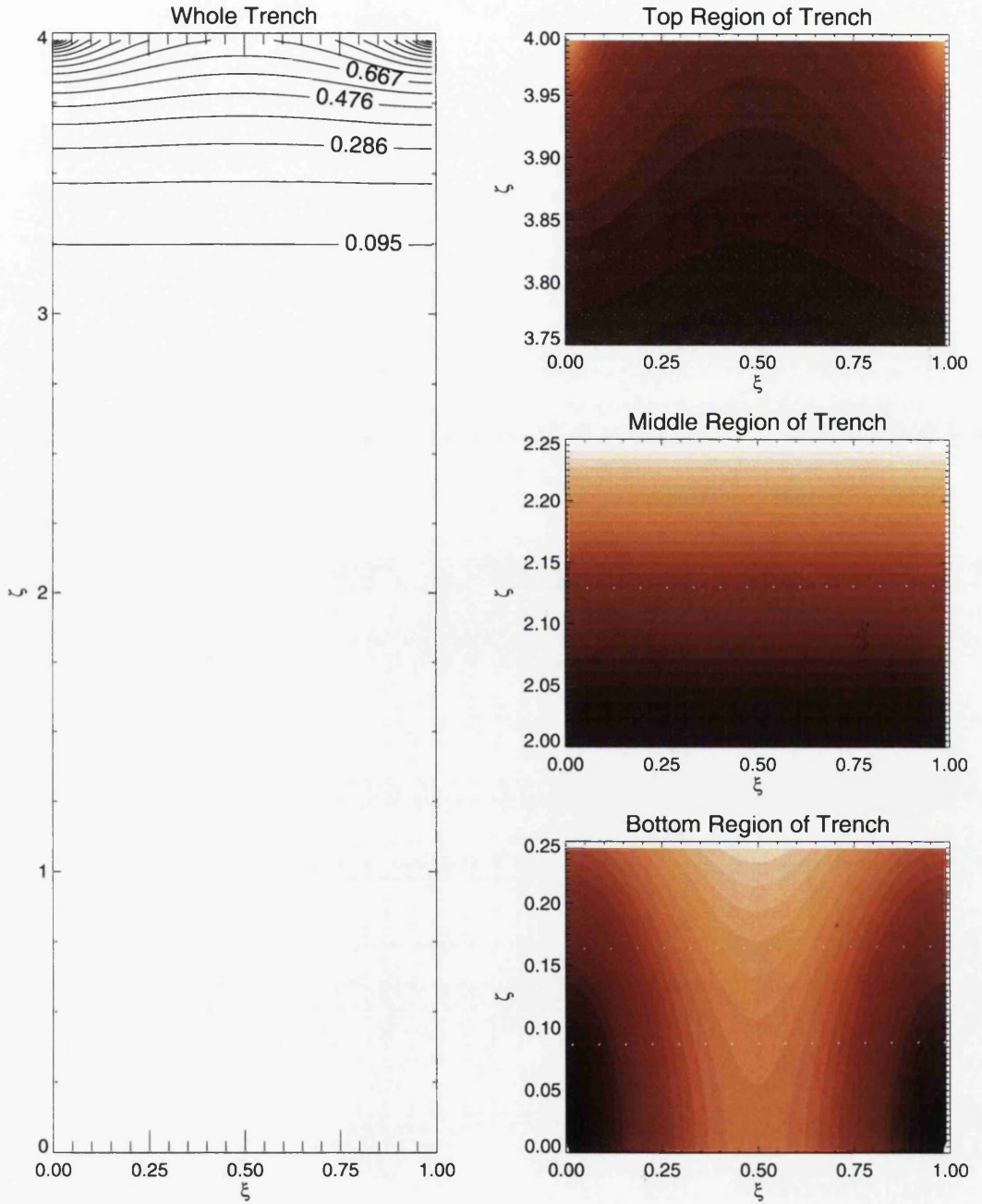


Figure 4.16: Electric field strength in the whole trench and in selected regions when $n = 27$.

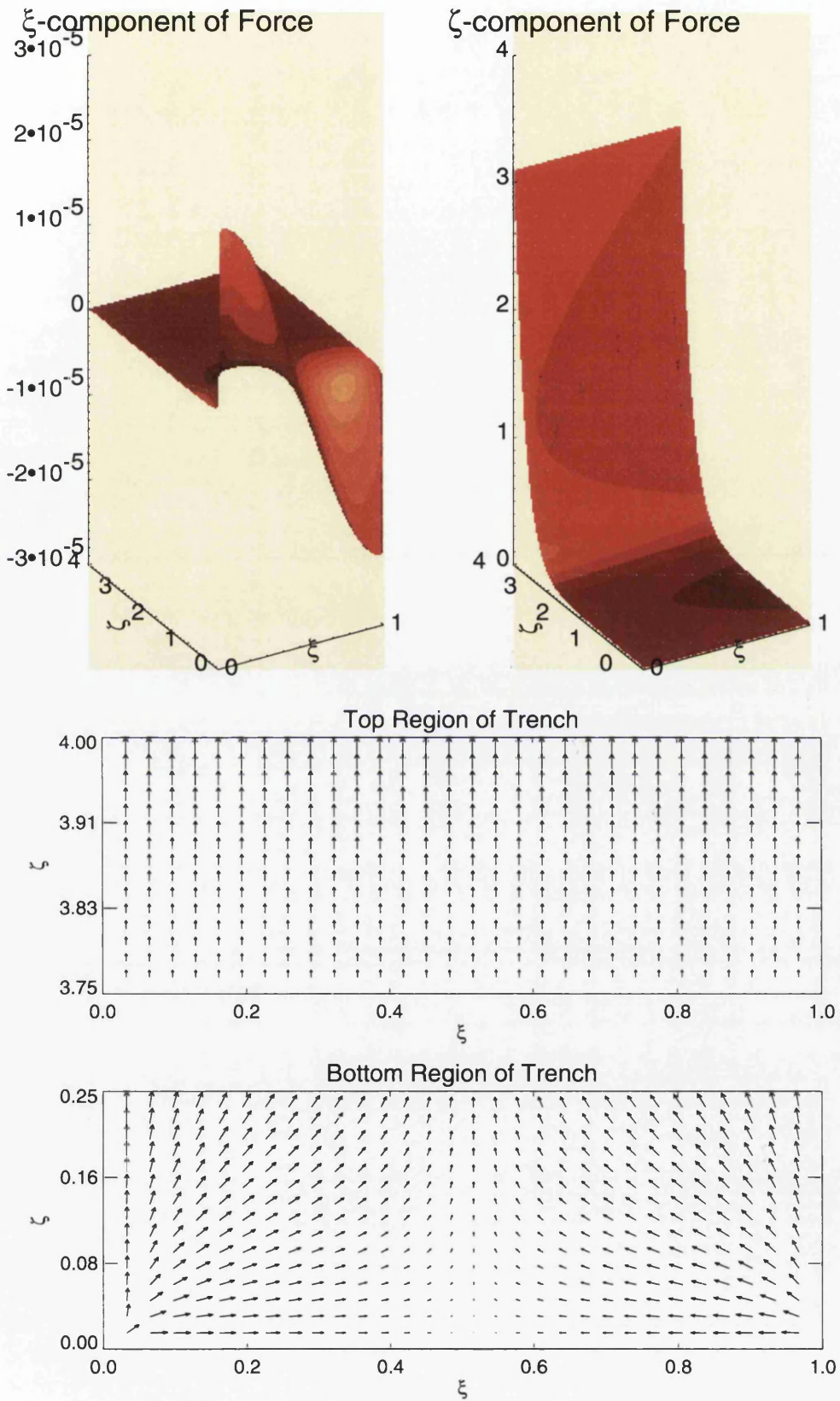


Figure 4.17: DEP Force when $n = 1$. Top plots show ξ and ζ components, bottom plots show total force in two regions of the trench.

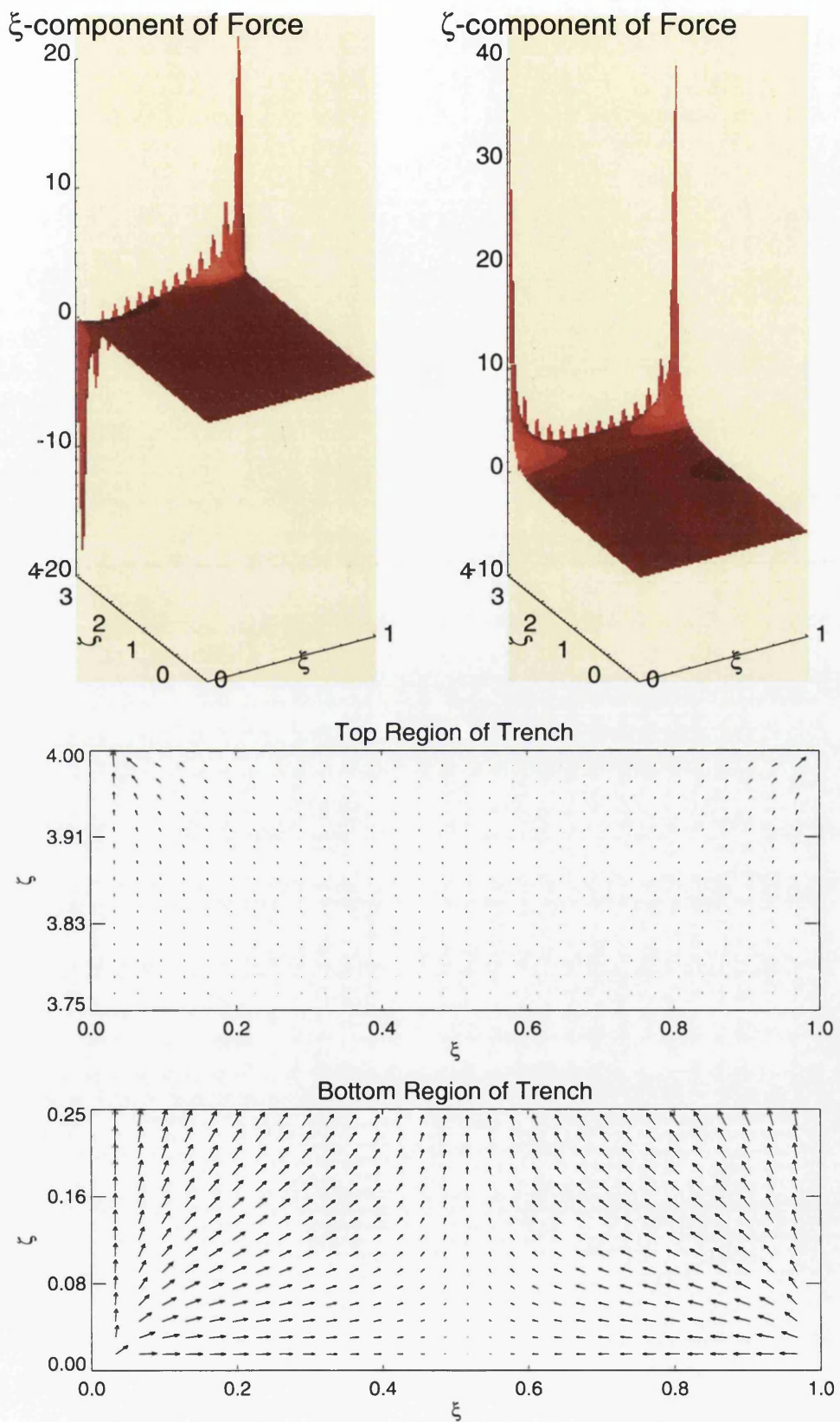


Figure 4.18: DEP Force when $n = 27$. Top plots show ξ and ζ components, bottom plots show total force in two regions of the trench.

(figure 4.14) is beginning to approach a square wave. This leads to a sharp change in potential at the corner between the trench and the opening. A steep gradient in potential means a rapidly changing electric field strength around the corner region. This accounts for the very high value for the DEP force at each top corner seen in figure 4.18. Because the force at the top corners is so large it completely dominates the plot showing the whole trench. Although this is the case, away from the top corners remains similar to the case that $n = 1$.

4.8.2 Simulation Results

All that remains is to carry out a series of simulations to ascertain how a particle responds to the DEP force that has been evaluated and stored in an array. The same series of simulations as with the analytic model has been performed. Because the results are very similar, a reduced number are presented here. Particles ejected parallel to the trench walls with $\beta = 1$ and 100 are shown in figures 4.19 and 4.20 respectively.

Particles ejected at 45° for $\beta = 1$ and 100 are shown in figures 4.21 and 4.22 respectively.

It is shown in figure 4.14 that the difference between the $n = 1$ and $n = 27$ case is only present at the top of the trench. It follows that the particle trajectory away from the trench opening will be the same in each case. Some slight differences can be seen between the analytic and numerical results. This is due to the error which is introduced when dealing with discretised data. Steps could be taken to reduce this error, such as increasing the resolution of the grid which is being used. However, this would be at the cost of increased computation time and is not deemed necessary in this instance.

4.9 Change in Electric Field with Aspect Ratio

The results presented for the numerical model of the DEP force are all for a trench of aspect ratio 4. This is because the results shown for variations in aspect ratio via the analytic model cover this topic adequately in this context. However, it is worth illustrating how the electric field changes with aspect ratio using the numerical model, in order to highlight possible areas for future study.

Two aspect ratios are presented. Figures 4.23 and 4.24 show the whole and regions

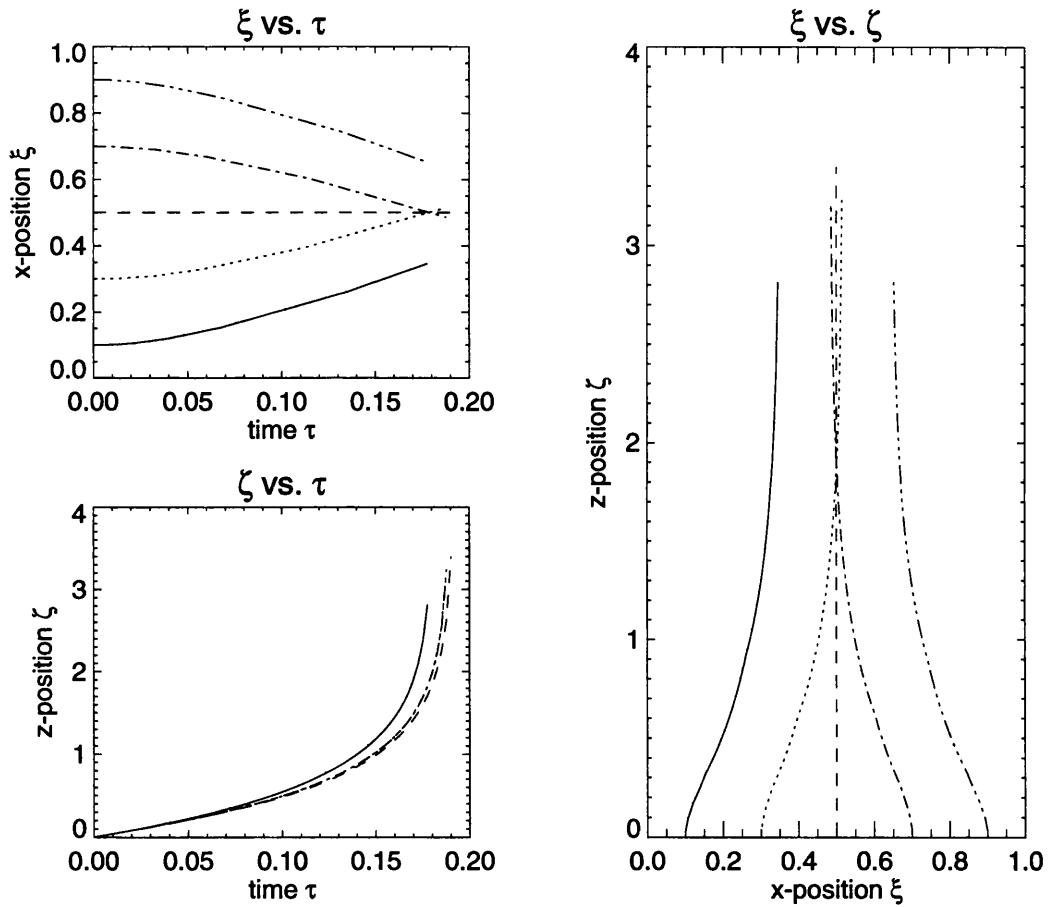


Figure 4.19: Numerical model, particles ejected perpendicular to trench bottom, $\beta = 1$. Position of particles in ξ and ζ directions in respect to τ and each other. Centring force is seen as in analytic case.

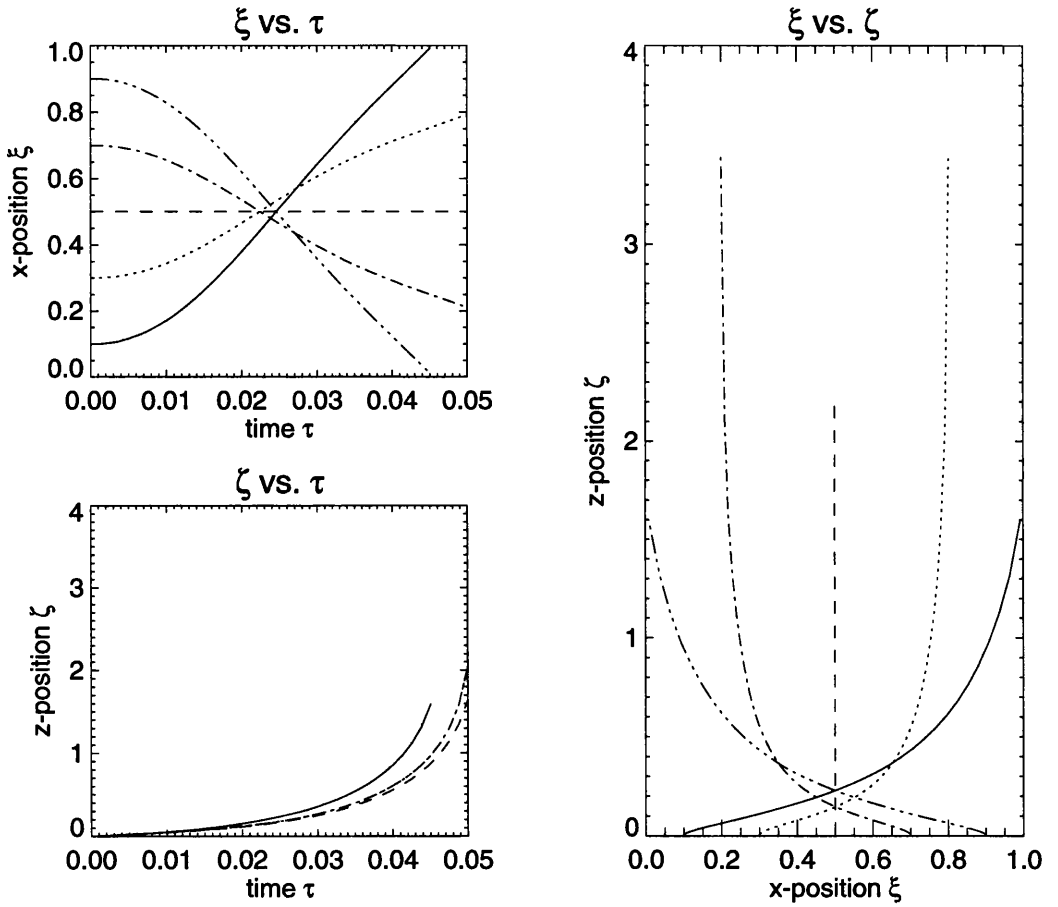


Figure 4.20: Numerical model, particles ejected perpendicular to trench bottom, $\beta = 100$. Position of particles in ξ and ζ directions in respect to τ and each other. Centring force is seen as in analytic case.

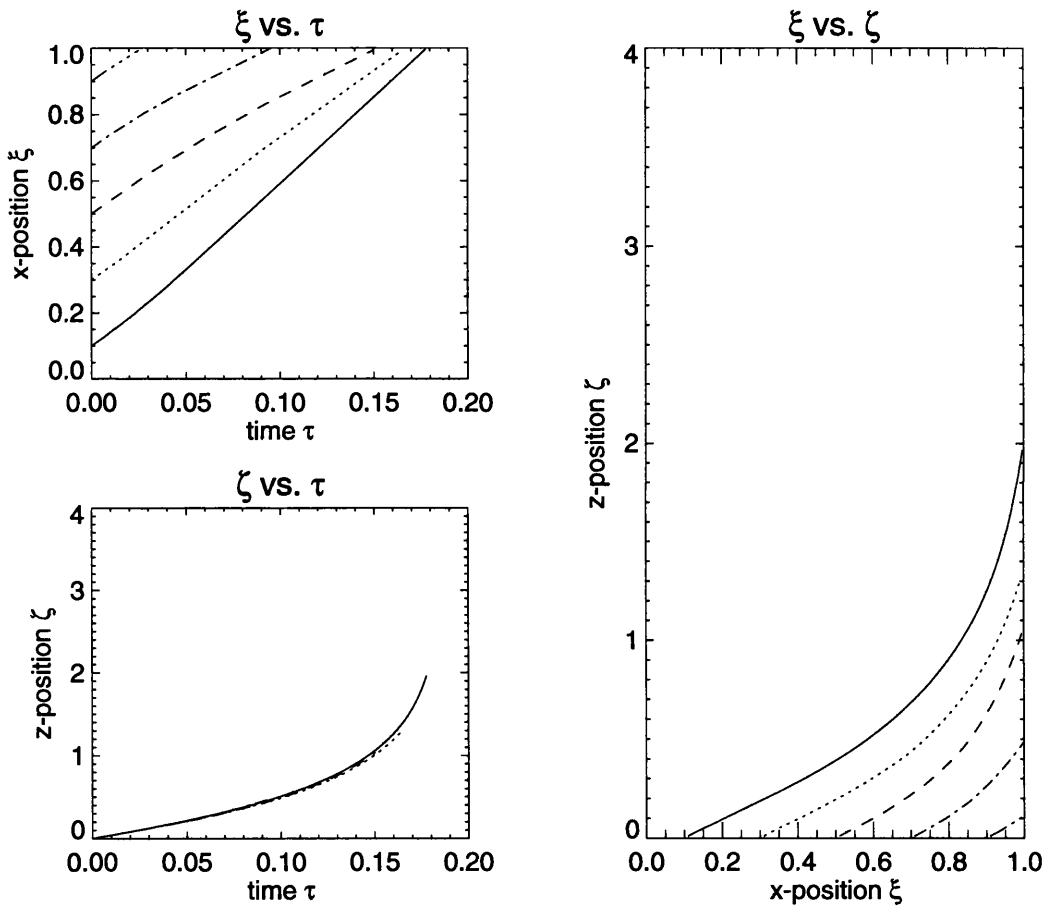


Figure 4.21: Numerical model, particles ejected at 45° to trench bottom, $\beta = 1$. Position of particles in ξ and ζ directions in respect to τ and each other. Centring force is seen as in analytic case.

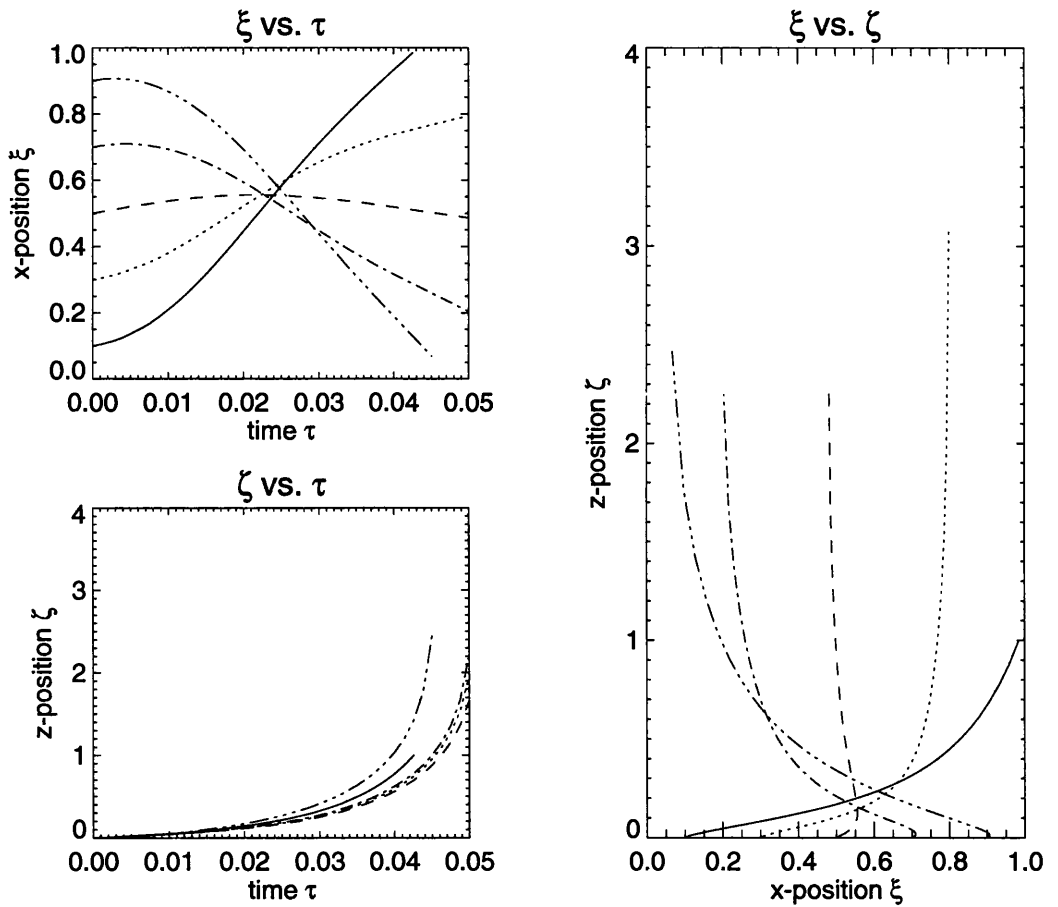


Figure 4.22: Numerical model, particles ejected at 45° to trench bottom, $\beta = 100$. Position of particles in ξ and ζ directions in respect to τ and each other. Centring force is seen as in analytic case.

Issue	Analytic Model	Numerical Model
Computation Time	Very quick	Slow
Accuracy	To first order	To high order
Adaptability	Not adaptable	Adaptable to different boundary conditions

Table 4.1: Differences between the analytic and numerical DEP models.

of a trench with aspect ratio 2. Similar plots are given in figures 4.25 and 4.26 for aspect ratio 8. These results are presented with the correct aspect ratio in order to be as informative as possible.

Attention is drawn to the similarity in the top region of the trench in both cases. The strong electric field around the top corners is also noted. By comparing the values in the middle and bottom of the trench between the two aspect ratios, it can be seen that the field gradient is much greater in the high aspect ratio case.

The contrast with the analytic result is due to the boundary conditions. In the numerical case the top of the trench approaches a step change in potential from the walls, causing a strong electric field. In the analytic case there is a smooth transition in potential from the walls to the centre at the top of the trench. The electric field is correspondingly smooth.

4.10 Comparison of Analytic and Numerical Approaches to DEP model

The differences between the two models that have been examined can be clearly identified. Table 4.1 presents relative merits of an analytic or numerical approach.

For a simulation using the boundary condition presented on page 61 and implemented in the preceding simulations, the analytic method provides the most satisfactory route to a solution. This is because of the nature of the problem to which it is being applied. One factor dominates in why the analytic solution is so appropriate:

The area of interest is the interior of a high aspect ratio trench.

This was made clear in (4.10) while justifying proceeding with an expansion of only the first order at the beginning of this chapter.

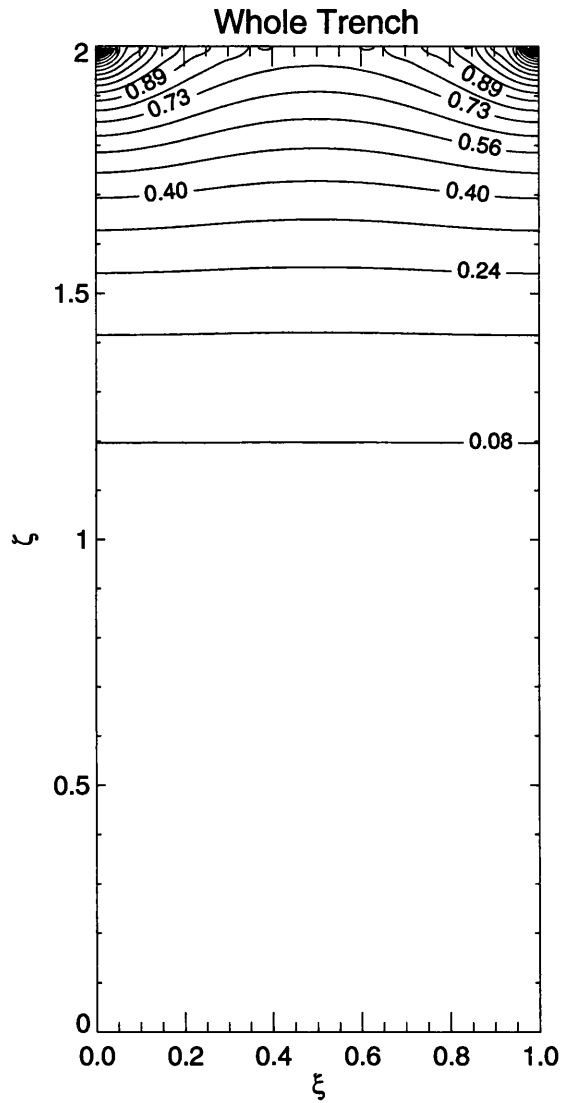


Figure 4.23: Electric field strength in whole trench when aspect ratio = 2. The field is concentrated at the top of the trench, particularly around the sharp corner features.

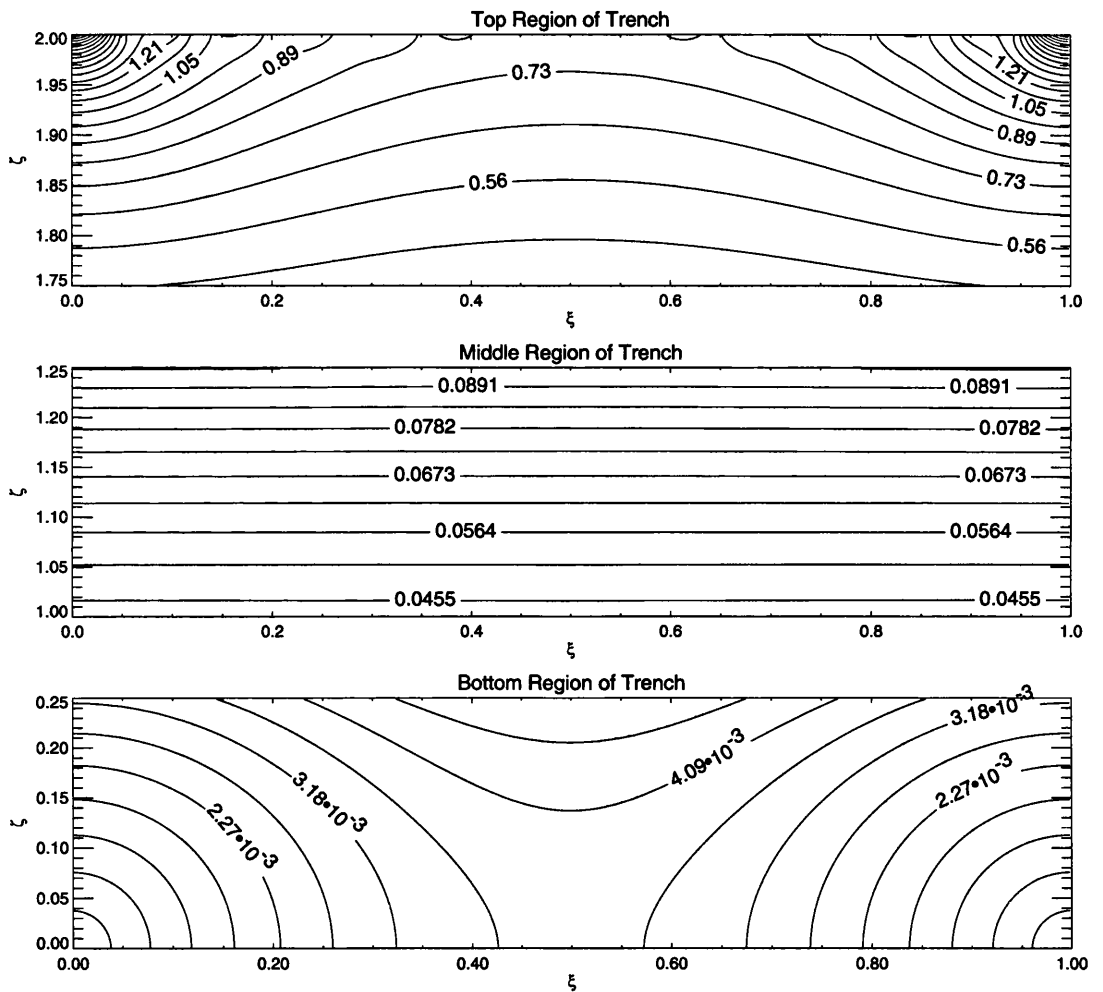


Figure 4.24: Electric field strength in trench when aspect ratio = 2. Selected regions of the trench are shown to expose field variations that cannot be seen in the plot of the whole trench. The reason for the centring force can be seen at the bottom of the trench.

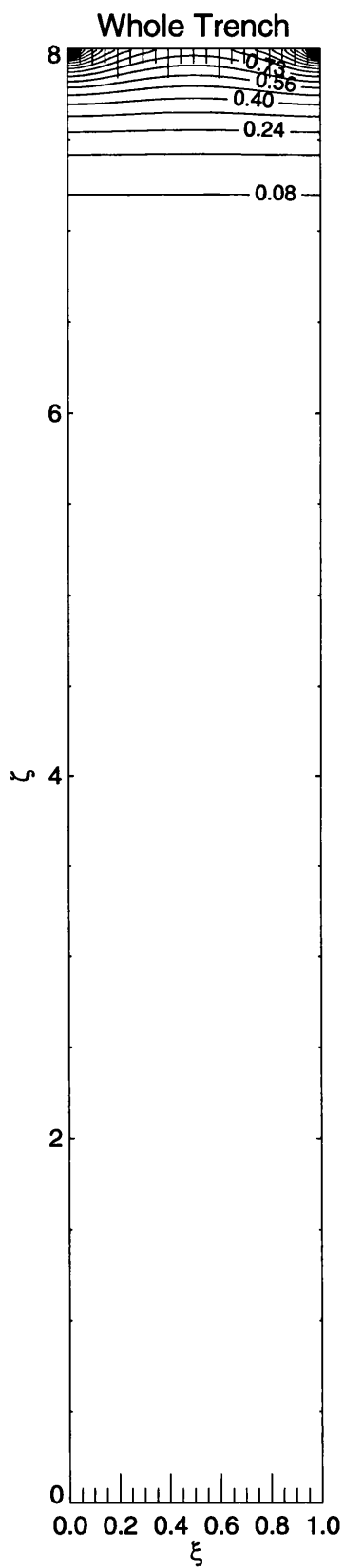


Figure 4.25: Electric field strength in whole trench when aspect ratio = 8. Similar to previous case, but the electric field is concentrated in the upper portion of the trench.

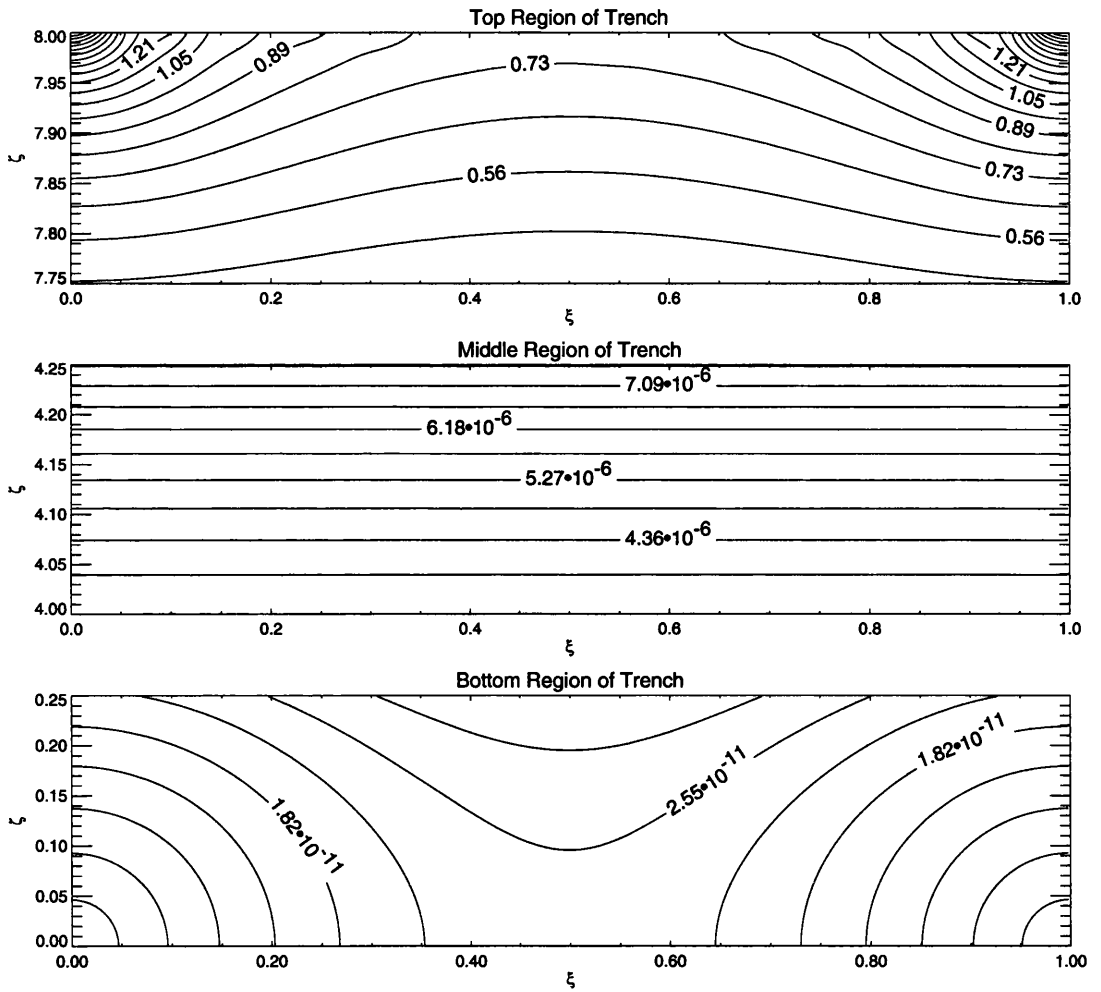


Figure 4.26: Electric field strength in selected regions of trench with aspect ratio = 8. Similar characteristics as aspect ratio = 2 trench, but absolute values are much smaller further down the trench.

The development of a numerical method which can be given any potential as a starting point provides a useful tool for two reasons:

1. Non-trivial boundary conditions may be implemented.
2. Study of small scale features not represented in the analytic formulation can be performed.

The second point would, for example, allow the top corner features to be examined, because at this point particles are strongly attracted back to the substrate. The implications of this have not been addressed here, but a mechanism is now in place to allow this to be considered.

Chapter 5

Conclusions, Future Work and Speculation

5.1 Summary

The path of ions traversing the sheath region of an rf plasma is modelled using the Child-Langmuir analytic approximation to the full sheath equation. The collective characteristics of many ions is obtained by Monte Carlo simulation, revealing structure in the relationship between many parameters. The structure of the relationship between the initial ion energy, the phase at which an ion enters the sheath region and the ion energy on impact with a substrate has been extensively explored. By performing a systematic calculation of ion impact energy versus initial energy and phase, a distinctive spiral shape has been observed. This provides additional insight into the mechanism that underlies the bimodal ion energy distributions that are widely reported in plasma processing systems.

A further step has been taken from this observation, to see if it can be used to provide an analytic method for constructing ion energy distributions. A spiral shape that varies continuously across phase and initial ion energy space has been created, replicating that seen in Monte Carlo simulation. By sampling the result across the appropriate initial conditions, an ion energy distribution can be generated.

An investigation of the shortcomings of the Child-Langmuir sheath representation has been made. In the Child-Langmuir equation, electrons are dismissed from the full non-linear equation order to permit an analytic solution. As a result, the assumption that electrons have a negligible effect is forced upon this representation. A numerical solution to the full sheath equation has been implemented, reintroducing electrons into the area where the sheath region meets the plasma. It has been shown that this causes the ions to follow a significantly different path through the sheath region, spending more time being acted on by the oscillating sheath. When an ion first enters the sheath region, a smaller force is experienced due to the reduction in electric field because of the presence of electrons. These effects propagate through to the ion energy distribution, reducing the low energy tail and affecting the attainable energy range.

Effects due to the high electric fields that are present in etched substrate features have been considered. Particles subject to an electric dipole moment are attracted along lines of increasing electric field strength under a mechanism called dielectrophoresis. An assessment of the significance of this force on neutral transport in the region of the substrate has been made. It is found that particles with a typical dielectric moment are accelerated towards the central region of a trench and accelerated out of the trench

in a fraction of time that it would take without a force due to dielectrophoresis. Two methods have been implemented, one analytic and one numerical. An analytic approach is found to be favourable when looking at the overall effect in a rectangular trench. The numerical method needs to be invoked when looking at features towards the top of the trench or if considering a non-rectangular geometry.

5.2 Future Work

5.2.1 Ion Dynamics

1. Collisional effects have not been looked at in the work presented here. If the mean free path of an ion is less than the characteristic dimension of the sheath, then it has to be considered to be collisional. This means that the energy conservation equation used (page 12) no longer applies, this term has to be modified to incorporate collisional behaviour. Collisions will have a tendency to reduce the impact ion energy through losses that occur during a collision. Whether this destroys the phase relationship or not would be useful to find out. Perhaps noise would be introduced into the relationship, or a more complicated structure could emerge. It is likely that the number of collisions will have a strong influence on these questions.
2. Deriving ion energy distributions from an analytic spiral description is presently disconnected from real parameters. It seems reasonable that if the sheath conditions are characterised appropriately then real parameters can be formulated for the model. It will then be possible to directly produce ion energy distributions for real systems. The key to this lies in defining the function used to control the shape across the spiral. If this was achieved it would provide a very efficient model of IED's.

5.2.2 Dielectrophoresis

1. The attraction of particles to the corner features of trenches has implications for the transport of neutral particles. Looking at a substrate as a whole, each feature on the surface will deform the electric field and attract neutral particles. The increased concentration of particles could lead to formation of dust and alter the behaviour the system in other ways.

2. Using the numerical model of dielectrophoresis, a much larger region of a substrate can be examined. This will allow the inclusion of the sheath region and a variety of different shaped features.
3. The flux of particles in each direction should be considered to see if collisional effects are significant. If collisions are found to occur then this raises the question of whether ejected neutral particles cause ionisation of fast moving ions in the sheath region.
4. The work presented on dielectrophoresis was limited to molecules that exhibit a permanent dipole moment. A symmetrical molecule such as CF_4 has no permanent electric dipole moment, but if placed in a strong electric field, an electric dipole moment may be induced. An induced dipole will not be as significant as a permanent dipole, but considering the magnitude of the effect that has been found, a molecule with a reduced dipole moment is likely to be of interest.
5. As seen in the work on ion dynamics, the sheath potential is time dependent. Time dependence should be incorporated into this model to give a more realistic representation of the system.

5.3 Speculation

5.3.1 General Application of Spiral Observation

Spiral work could be applied to any situation in which a charged particle interacts with an oscillating field.

5.3.2 Non-Sinusoidal Driving Voltages

Some investigations have been made into the effect of driving the electrodes of a reactor with a frequency-modulated signal rather than a sinusoid. In practice this would probably be achieved by separate rf biasing of the substrate [48]. By changing the shape of the oscillating sheath it appears possible to manipulate ion energy distributions, which is in line with results showing the importance of phase in the final ion energy. In effect it may be possible to disguise the influence of phase by jumbling the initial phase encounters of ions.

References

- [1] Marconi-Corp. Marconi on-line museum. <http://www.marconicalling.com>, 2001.
- [2] ScienCentral Inc. and American Institute Of Physics. Transistorized. <http://www.pbs.org/transistor/>, 1999.
- [3] C. C. Fang, F. Jones, R. R. Kola, G. K. Celler, and V. Prasad. Stress and microstructure of sputter-deposited thin films: Molecular dynamics simulations and experiment. *J. Vac. Sci. Technol. B*, 11(6):pp2947–2952, 1993.
- [4] J. W. Coburn and E. Kay. Positive-ion bombardment of substrates in rf diode glow discharge sputtering. *J. Appl. Phys.*, 43(12):pp4965–4971, 1972.
- [5] S. G. Ingram and N. St. J. Braithwaite. Ion and electron energy analysis at a surface in an rf discharge. *J. Phys. D: Appl. Phys.*, 21(10):pp1496–1503, 1988.
- [6] S. G. Ingram and N. St. J. Braithwaite. Rf modulation of positive-ion energies in low-pressure discharges. *J. Appl. Phys.*, 68(11):pp5519–5527, 1990.
- [7] J.-B. Kim, K. Kawamura, Y.-W. Choi, M. D. Bowden, and K. Muraoka. Studies of a sheath structure in an rf discharge using experimental, analytical, and simulation approaches. *IEEE Trans. on Plasma Sci.*, 27(5):pp1510–1515, 1999.
- [8] E. A. Edelberg, A. Perry, N. Benjamin, and E. S. Aydil. Energy distribution of ions bomarding biased electrodes in high density plasma reactors. *J. Vac, Sci. Technol. A*, 17(2):pp506–516, 1999.
- [9] M. A. Sobolewski, J. K. Olthoff, and Y. Wang. Ion energy distributions and sheath voltages in a radio-frequency-biased inductively coupled, high-density plasma reactor. *J. Appl. Phys.*, 85(8):pp3966–3975, 1999.
- [10] P. Benoit-Cattin and L.-C. Bernard. Anomalies of the energy of positive ions

- extracted from high-frequency ion sources. a theoretical study. *J. Appl. Phys.*, 39(12):pp5723–5726, 1968.
- [11] Y. Okamoto and H. Tamagawa. Energy dispersion of positive ions effused from an rf plasma. *J. Phy. Soc. Jap.*, 29(1):pp187–191, 1970.
- [12] M. J. Kushner. Distribution of ion energies incident on electrodes in capacitively coupled rf discharges. *J. Appl. Phys.*, 58(11):pp4024–4031, 1985.
- [13] G. A. Hebner and M. J. Kushner. Phase and energy distribution of ions incident on electrodes in radio-frequency discharges. *J. Appl. Phys.*, 62(6):pp2256–2260, 1987.
- [14] B. E. Thompson and H. H. Swain. Monte Carlo simulation of ion transport through rf glow-discharge sheaths. *J. Appl. Phys.*, 63(7):pp2241–2251, 1988.
- [15] A. Bogaerts. Comprehensive modelling network for dc glow discharges in argon. *Plasma Sources Sci. Technol.*, 8:pp210–229, 1999.
- [16] E. Kawamura, V. Vahedi, M. A. Lieberman, and C. K. Birdsall. Ion enery distributions in rf sheaths; review, analysis and simulation. *Plasma sources Sci. Technol.*, 8:ppR45–R64, 1999.
- [17] B. N. Chapman. *Glow Discharge Processes, Sputtering And Plasma Etching*. John Wiley & Sons, Inc., New York, 1980.
- [18] H. Conrads and M. Schmidt. Plasma generation and plasma sources. *Plasma Sources Sci. Technol.*, 9:pp441–454, 2000.
- [19] N. Sakudo. Microwave ion sources for material processing. *Rev. Sci. Instr.*, 69(2):pp825–830, 1998.
- [20] G. Hancock. Diagnostics of active species in plasmas. *Surf. Coat. Technol.*, 74-5(Part 1):pp10–14, 1995.
- [21] J.-P. Booth. Optical and electrical diagnostics of fluorocarbon plasma etching processes. *Plasma Sources Sci. Technol.*, 8:pp249–257, 1999.
- [22] G. Cunge, P. Chabert, and J.-P. Booth. Laser-induced fluorescence detection of SiF₂ as a primary product of Si and SiO₂ reactive ion etching with CF₄ gas. *Plasma Sources Sci. Technol.*, 6:pp349–360, 1997.

- [23] G. A. Hebner. Relative atomic chlorine density in inductively coupled chlorine plasmas. *J. Appl. Phys.*, 81(2):pp578–581, 1997.
- [24] B. K. McMillin and M. R. Zachariah. Two-dimensional images of CF_2 density in CF_4/Ar plasmas by laser-induced fluorescence in a GEC rf reference cell. *IEEE Tran. Plas. Sci.*, 24(1):pp113–114, 1996.
- [25] N. A. Kubota and D. J. Economou. Molecular dynamics simulations of low-energy (25–200 eV) argon ion interactions with silicon surfaces: Sputter yields and product formation pathways. *J. App. Phys.*, 83(8):pp4055–4063, 1998.
- [26] G. M. W. Kroesen, H.-J. Lee, H. Moriguchi, H. Motomura, T. Shirafuji, and K. Tachibana. Investigations of the surface chemistry of silicon substrates etched in a rf-biased inductively coupled fluorocarbon plasma using Fourier-transform infrared ellipsometry. *J. Vac. Sci. Technol. A*, 16(1):pp225–232, 1998.
- [27] A. Laganá, S. Crocchianti, G. Ochoa, A. Riganelli, and E. García. Accurate calculations of cross sections and rate coefficients of some atom-diatom reactions relevant to plasma chemistry. *Plasma Sources Sci. Technol.*, 6:pp270–279, 1997.
- [28] V. Martišoviš and M. Zahoran. Transport of chemically active species in plasma reactors for etching. *Plasma Sources Sci. Technol.*, 6:pp280–297, 1997.
- [29] F. F. Chen. *Introduction To Plasma Physics*. Plenum Press, New York, 1974.
- [30] D. Bohm. *The Characteristics Of Electrical Discharges In Magnetic Fields*. MacGraw-Hill, New York, 1949.
- [31] K.-U. Riemann. The Bohm criterion and sheath formation. *J. Phys. D: Appl. Phys.*, 24:pp493–518, 1991.
- [32] N. Metropolis. The beginning of the Monte Carlo method. *Los Alamos Science*, 15:pp125–130, 1987.
- [33] T. Warnock. Random-number generators. *Los Alamos Science*, 15:pp137–141, 1987.
- [34] W. H. Press, B. P. Flannery, S. A. Teukolsky, and W. T. Vetterling. *Numerical Recipes: The Art Of Scientific Computing*. CUP, Cambridge, 1989.
- [35] Y. P. Song, D. Field, and D. F. Klemperer. Electrical potentials in rf discharges. *J. Phys. D: Appl. Phys.*, 23(6):pp673–681, 1990.

- [36] D. Field, D. F. Klemperer, P. W. May, and Y. P. Song. Ion energy distributions. *J. Appl. Phys.*, 70(1):pp82–92, 1991.
- [37] M. Sugawara. *Plasma Etching: Fundamentals And Applications*. OUP, Oxford, 1998.
- [38] H. A. Pohl. *Dielectrophoresis, The Behaviour Of Neutral Matter In Nonuniform Electric Fields*. CUP, Cambridge, 1978.
- [39] N. G. Green and H. Morgan. Dielectrophoretic investigations of sub-micrometre latex spheres. *J. Phys. D: Appl. Phys.*, 30(18):pp2626–2633, 1997.
- [40] T. Müller, A. Gerardino, T. Schnelle, S. G. Shirley, F. Bordoni, G. De Gasperis, R. Leoni, and G. Fuhr. Trapping of micrometre and sub-micrometre particles by high-frequency electric fields and hydrodynamic forces. *J. Phys. D: Appl. Phys.*, 29(2):pp340–349, 1996.
- [41] R. W. Rosensweig. *Ferrohydrodynamics*. CUP, Cambridge, 1985.
- [42] T. B. Jones. *Electromechanics Of Particles*. CUP, Cambridge, 1995.
- [43] P. Lorrain and D. R. Corson. *Electromagnetic Fields And Waves*. Freeman, San Francisco, 2nd edition, 1970.
- [44] D. Adalsteinsson and J. A. Sethian. A level set approach to a unified model for etching, deposition, and lithography. *J. Comp. Phys.*, 138(1):pp193–223, 1997.
- [45] G. S. Hwang and K. P. Giapis. Aspect-ratio-dependent charging in high-density plasmas. *J. Appl. Phys.*, 82(2):pp566–571, 1997.
- [46] D. R. Lide, editor. *Handbook Of Chemistry And Physics*. CRC Press, Florida, 74th edition, 1994.
- [47] M. A. Lieberman and A. J. Lichtenberg. *Principles Of Plasma Discharges And Materials Processing*. John Wiley & Sons, Inc., New York, 1994.
- [48] D. Barton, D. J. Heason, R. D. Short, and J. W. Bradley. The measurement and control of the ion energy distribution function at a surface in an rf plasma. *Meas. Sci. Technol.*, 11:pp1726–1731, 2000.

